Hamahashi *et al.*
Progress in Earth and Planetary Science (2024) 11:8
https://doi.org/10.1186/s40645-024-00607-0

Progress in Earth and Planetary Science

RESEARCH ARTICLE

Open Access

Shallow structure and late quaternary slip rate of the Osaka Bay fault, western Japan

Mari Hamahashi[1,8*], Hironori Otsuka[1], Yoshiaki Suzuki[2], Jun Arimoto[2], Tetsuo Matsuno[1], Nobukazu Seama[1,3], Yuzuru Yamamoto[1,3], Hiroko Sugioka[1,3], Stephen A. Bowden[1,4], Satoshi Shimizu[1,6], Hikaru Iwamaru[1,5], Mamoru Sano[1,5], Keita Suzuki[1,5], Katsuya Kaneko[1,3], Kazuo Nakahigashi[7] and Yoshiyuki Tatsumi[1]

Abstract

The Osaka Bay is situated at a seismically active region north of the Median Tectonic Line and east of Awaji Island in western Japan, known as part of the Kinki Triangle and the Niigata–Kobe Tectonic Zone. Dense distribution of active faults and high geodetic strain rates characterize the region, posing a major seismic hazard potential to the coastal and metropolitan areas of the Kansai region. To investigate the shallow structure and recent deformation history of active faults in the Osaka Bay, we acquired 15 high-resolution seismic profiles using a Mini-GI airgun and a Boomer as active sources, together with multi-beam bathymetry data across the Osaka Bay Fault. Our seismic sections image a ~0.1 to 3.7 km-wide asymmetric anticline forelimb above the Osaka Bay Fault at shallow depths, coupled with a ~2.6 km-wide syncline to the west, and a broad, ~11 km-wide syncline in the footwall to the east. The synclinal axial surface at shallow depths measured in this study ranges 75°–89°. We observe the vertical displacement of the Osaka Bay Fault increasing northwards along strike. The sediment thickness on the hanging wall, however, is variable, modified by non-tectonic processes such as by tidal currents, affecting the geometry of growth strata. The most recent deformation by the Osaka Bay Fault reaches to near the seafloor by active folding, with large vertical offsets of 8–14 m over the last ~11 ka, and 5–11 m over the last ~5 ka. By combining with previously reported borehole age data, the average uplift rate on the Osaka Bay Fault is estimated to be ~1.0 to 1.7 m/ka during the Latest Pleistocene to Holocene. The inferred slip of the Osaka Bay Fault during the Holocene is likely to account for >5% of the regional geodetic strain accumulation within the Kinki Triangle. Further studies to evaluate the Holocene slip rates of regional faults are necessary to assess the seismic hazards and the internal strain budgets within the Kinki Triangle and the Niigata–Kobe Tectonic Zone.

Keywords Seismic reflection survey, Multi-beam bathymetry, Osaka Bay fault, Slip rate, Late quaternary sediments, Growth strata, Kinki triangle, Niigata–Kobe tectonic zone, Boreholes, Sedimentary basins

*Correspondence:
Mari Hamahashi
mhamahashi@yamaguchi-u.ac.jp
Full list of author information is available at the end of the article

Graphical abstract

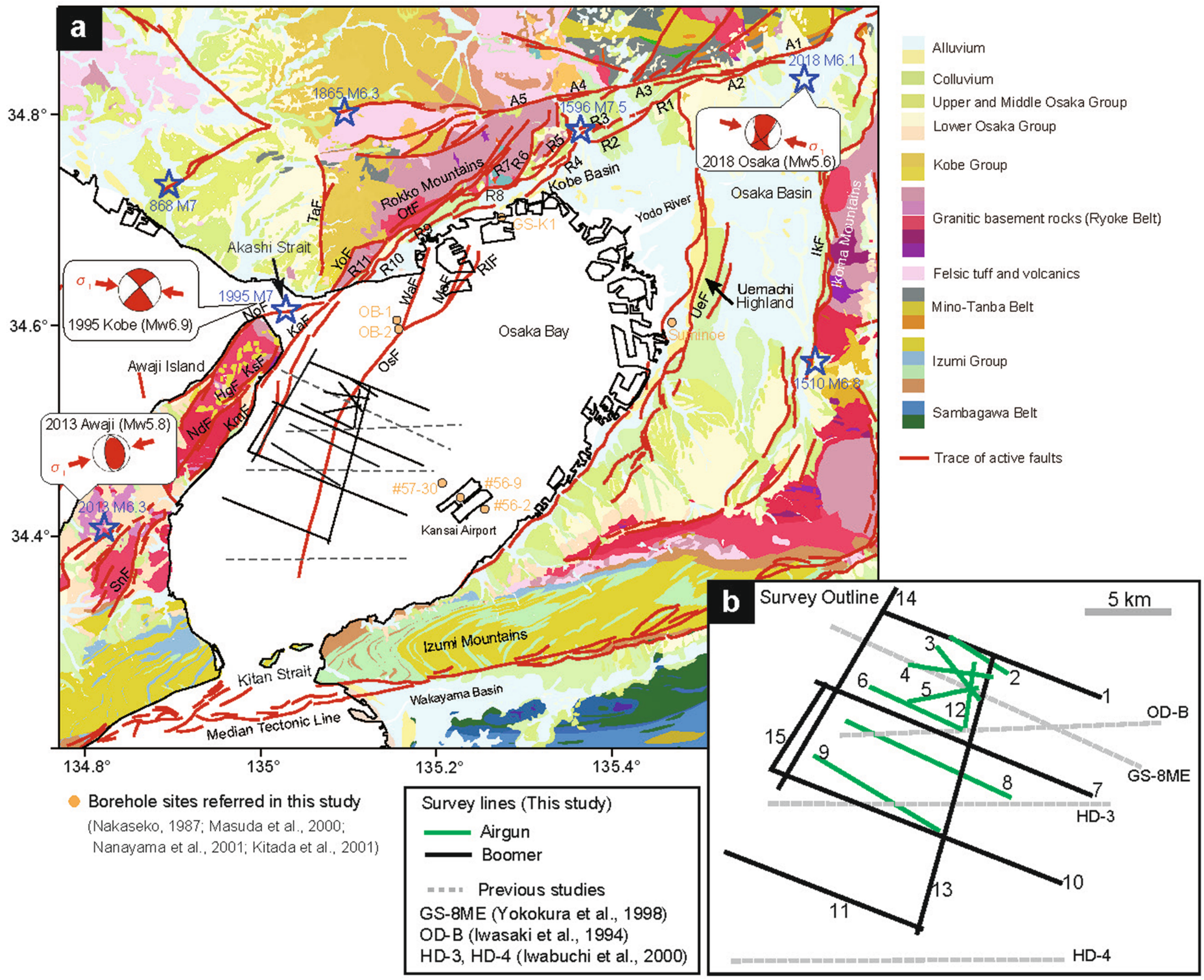

(See figure on next page.)

Fig. 1 Tectonic setting of the Kinki Triangle, western Japan. (**a**) Distribution of active faults (red lines) and the Kinki Triangle (yellow) after National Institute of Advanced Industrial Science and Technology (2012). Shaded relief and bathymetry (10-m and 500-m horizontal grid-spacing, respectively) are based on digital elevation map by the Geospatial Information Authority of Japan. White triangles: Quaternary volcanoes (Committee for Catalog of Quaternary Volcanoes in Japan 1999). Box shows location of study area closed-up in Fig. 2a. Dotted line shows location of cross-section in Fig. 1c. (**b**) Interseismic secular velocity at onland GNSS and offshore GPS-A stations modified from Nishimura et al. (2018). Vectors are velocities relative to the stable Amurian plate with 95% confidence limit ellipsoids (Nishimura et al. 2018). The shaded yellow region and pink line are the Niigata–Kobe Tectonic Zone (Sagiya et al. 2000) and the Median Tectonic Line, respectively. Depth contour (km) of the upper boundary of the Philippine Sea and Pacific Plates are from Nakajima and Hasegawa (2007). (**c**) Schematic cartoon of the E–W cross-section and inferred geometry of faults at ~ 34°N based on previous studies modified after Sato et al. (1998, 2009). Shaded gray: sedimentary basin in this region. OsF: Osaka Bay Fault. KaF: Kariya Fault. NoF: Nojima Fault. UeF: Uemachi Fault. IkF: Ikoma Fault. NbF: Nara Basin East Edge Fault. TgF: Taguchi Fault. IsF: Isshi Fault. YiF: Yokkaichi Fault. The upper/lower crust boundary is inferred at the downdip limit of the seismogenic zone (cross-hatched area) (e.g., Tanaka 2004). A possible detachment is speculated. Box shows region of study area closed-up in Fig. 2a

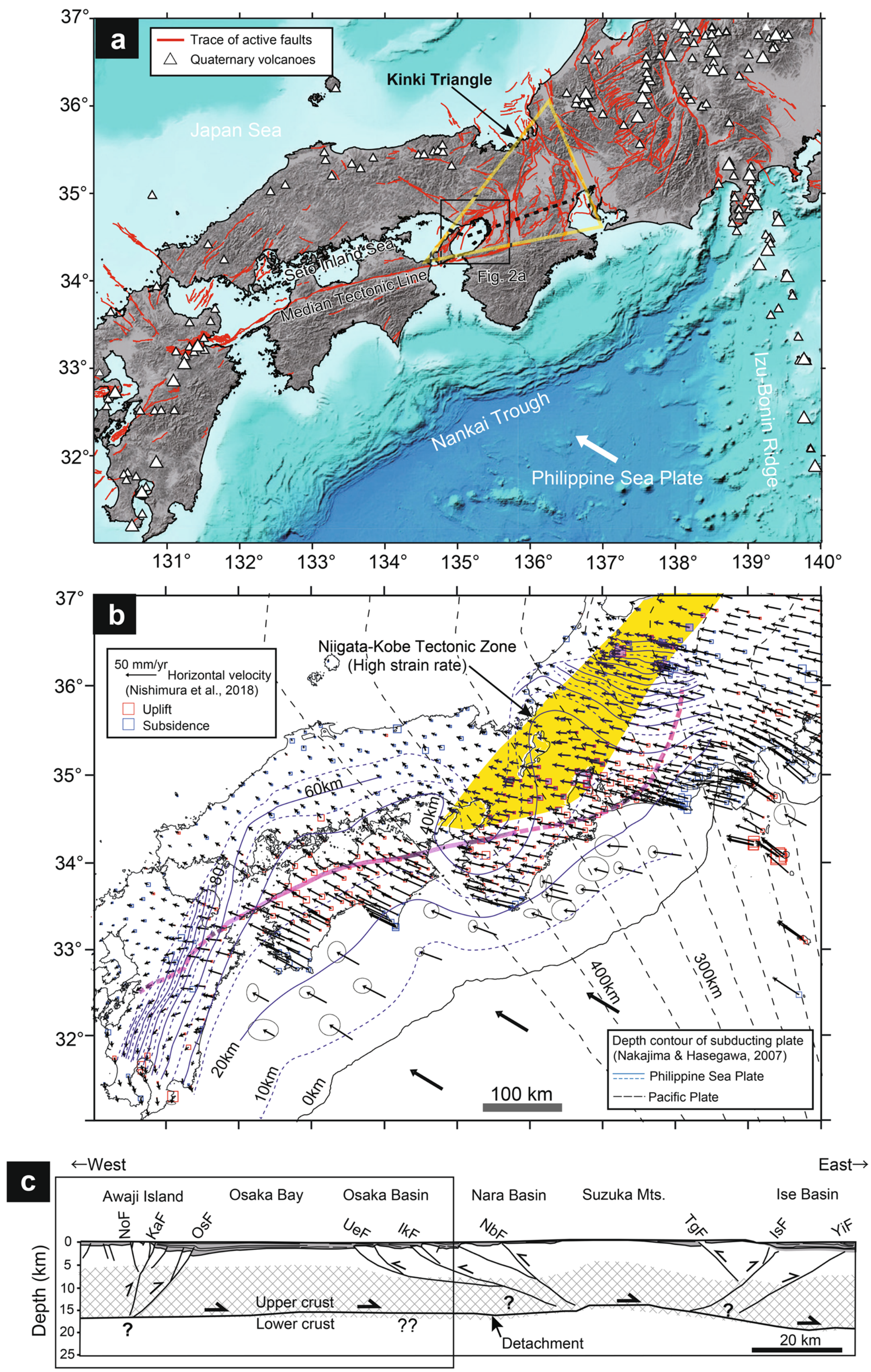

Fig. 1 (See legend on previous page.)

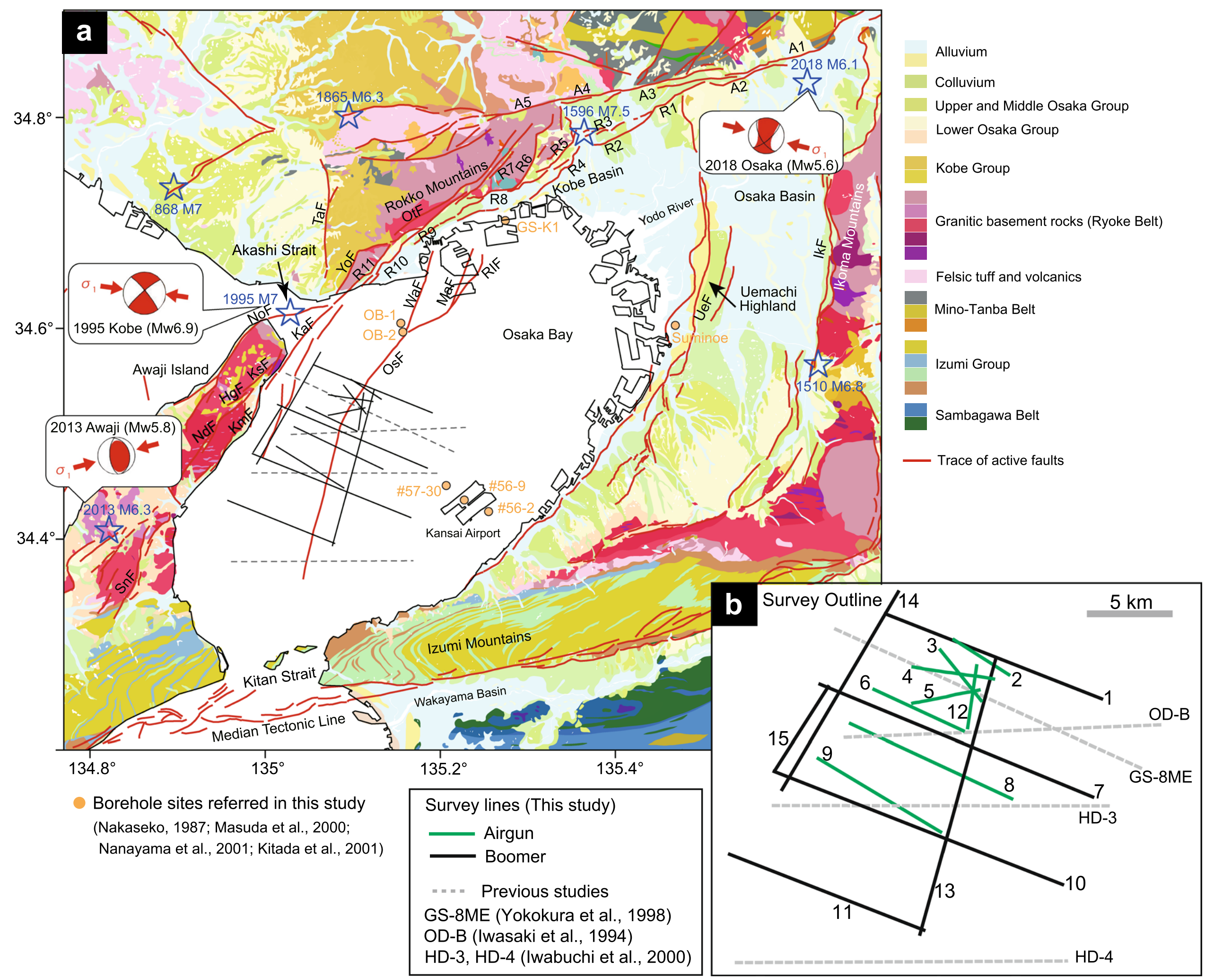

Fig. 2 Geologic map of study area. (**a**) Distribution of active faults (red lines) around the Osaka Bay (e.g., Kato et al. 2008). Black lines: seismic reflection survey lines in this study closed-up in (b). Dotted lines: deep seismic profiles by previous studies. Orange dots: location of boreholes referred in this study (Nakaseko 1987; Masuda et al. 2000; Masuda & Miyahara 2000; Nanayama et al. 2001; Kitada et al. 2001). OsF: Osaka Bay Fault. The Awaji Island Fault zone consist of the KaF: Kariya Fault, NoF: Nojima Fault, KsF: Kusumoto Fault, HgF: Higashiura Fault, KmF: Kamakuchi Fault, NdF: Nodao Fault, and SnF: Senzan Fault. WaF: Wadamisaki Fault. MaF: Maya Fault. RIF: Rokko Island Fault. YoF: Yokooyama Fault. TaF: Takatsukayama Fault. OtF: Otsuki Fault. R1-R10: Rokko Fault zone (R1: Nobata Fault. R2: Itami Fault. R3: Koyaike graben. R4: Nishinomiya flexure. R5: Koyo Fault. R6: Ashiya Fault. R7: Gosukebashi Fault. R8: Okamoto Fault. R9: Suwayama Fault. R10: Motomachi and Itayado flexures. R11: Suma Fault.). A1-A5: Arima-Takatsuki Fault zone (A1: Makami Faults. A2: Ai Fault. A3: Bojima Fault. A4: Kiyoshi-kojin Fault. A5: Rokko Fault). UeF: Uemachi Fault. IkF: Ikoma Fault. Blue stars show representative earthquakes. Focal mechanisms are based on Imanishi et al. (2020). Geologic map is modified from Geological Survey of Japan, AIST (2022). (**b**) Close-up of seismic reflection survey lines in this study. Green and black lines were acquired using an Airgun and a Boomer as active source, respectively

1 Introduction

Further than 100 km inboard from the subduction interface in central-western Japan, the crustal seismogenic zone is 5–20 km depth, based on the cut-off depths of seismicity and on heat flow gradients (Tanaka 2004; Nakajima and Hasegawa 2007). Active faulting is manifested under the contemporary compressional regime formed by the oblique subduction of the Philippine Sea Plate under the Japan arc at a current velocity of 40–65 mm/yr (Seno et al. 1993; Miyazaki and Heki 2001; Zang et al. 2002). The “Kinki Triangle” (Huzita 1962) is a seismically active region north of the Median Tectonic Line and east of Awaji Island, characterized by a dense distribution of active faults and high geodetic strain rates, also known as part of the “Niigata–Kobe Tectonic Zone” (Sagiya et al. 2000; Nishimura et al. 2018), posing a major seismic hazard potential to the coastal and metropolitan areas of the Kansai region (Fig. 1a, b). Moderate to large, destructive earthquakes frequently occur in this region, represented by the devastating 1995 M_w6.9 Kobe (Southern Hyogo Prefecture) earthquake (death toll: 6434) (e.g., Kikuchi and Kanamori 1996; Irikura et al. 1996), the 1596 Keicho-Fushimi Earthquake (death toll: > 600) (e.g., Ikeda et al. 2019), the 2018 M_w5.6 Northern Osaka prefecture earthquake (death toll: 6) (e.g., Hirata and Kimura 2018), and the 2013 M_w5.8 Awaji Island earthquake (e.g., Imanishi et al. 2020) (Fig. 2a).

Within the Kinki Triangle, based on patterns of geodetic strain accumulation (interseismic secular velocity) from Ise Basin to the Osaka Bay, an ESE–WNW to ENE–WSW shortening of ~ 10 to 20 mm/yr at latitude of 34°N can be inferred (Fig. 1b; Sagiya et al. 2000; Sagiya 2004; Loveless and Meade 2010; Nishimura et al. 2018, 2020). During interseismic periods, the seismogenic zone is partially locked, and strain is released during coseismic periods by transferring slip onto reverse and strike-slip faults in this region. Previous seismic reflection surveys have revealed a NE–SW trending fold-and-thrust belt consisting of ~ 30 to 40° west- and east-dipping reverse faults beneath the Ise Basin, Suzuka Mountain, Nara Basin, and the Osaka Basin (Ishiyama 2003; Sato et al. 2009; Kitada and Mimura 2016; Nishiwaki et al. 2021) (Fig. 1c). Whereas, to the west, ~ 70 to 80° east-dipping, high-angle reverse- and strike-slip faults characterize the structures around the Awaji Island and the Osaka Bay, including the Nojima Fault that ruptured in the 1995 earthquake, and the offshore Osaka Bay Fault (Iwasaki et al. 1994; Iwabuchi et al. 1995, 2000; Yokokura et al. 1998; Sato et al. 1998) (Fig. 1c).

The largest sedimentary basin in the region comprises the Osaka Basin and Osaka Bay. It is bounded by the E–W trending Median Tectonic Line to the south, the E–W trending Rokko-Awaji Island and Arima-Takatsuki Fault zones to the north, the NE–SW trending Nojima and Kariya Faults to the west, and the NE–SW trending Ikoma and Uemachi Faults to the east (Fig. 2a; Kusumoto et al. 2013; Itoh et al. 2013ab; Itoh and Takemura 2019c). The Late Pliocene and Quaternary basin fill here is up to ~ 3000 m thick (e.g., Yokokura et al. 1998). The subsidence and formation of this sedimentary basin is largely thought to have been contributed to by the movement/reactivation of faults within and surrounding the basin, which have been active since the Late Pliocene (Yokokura et al. 1998; Kusumoto et al. 2001, 2013; Itoh and Takemura 2019a, b, c). Here, active faults are buried by sediments and are often blind, complicating the assessment of their distribution and slip histories. Although blind, the surface expression of these faults is often observed in the form of folding (Ishiyama 2003; Sato et al. 2009; Kitada and Mimura 2016). The 2018 M_w5.6 Northern Osaka prefecture earthquake occurred on a previously unknown blind fault, demonstrating the damaging effects of blind fault earthquakes, and the potential for presence of many more hidden faults and/or off-fault seismicity (Hallo et al. 2019; Kato and Ueda 2019) (Fig. 2a).

Because these faults are continuously buried in rapidly subsiding basins, the progressive fault displacement and syn-tectonic growth strata are defined by well-constrained stratigraphic sequences. Acquisition of high-resolution seismic reflection data enable the documentation of deformed strata and imaging of fault and fold geometries, which in combination with borehole data, provides opportunities to characterize fault slip histories in detail (e.g., Ishiyama et al. 2007; Hamahashi et al. 2022). The sediments that fill the Osaka Basin and the Osaka Bay consist of fluvial, lacustrine, and marine sequences that can be correlated with global eustatic sea level changes, and their sediment ages are well-constrained by abundant tephra derived from the volcanic arc, in addition to marine microfossils, pollen assemblages and magnetostratigraphy (e.g., Hyodo et al. 1985; Masuda 1992; Biswas et al. 1999; Masuda and Miyahara 2000; Masuda et al. 2000; Nanayama et al. 2001; Itoh and Takemura 2019a).

The motivation for our research is to investigate the shallow structure and recent slip history of active faults in the Osaka Bay. The Osaka Bay Fault is a blind fault that extends for at least ~ 40 km across the bay, exhibiting one of the largest seismic and tsunami risks to the surrounding Kansai megacities (Nakamura 1999; Kawata et al. 2005; The Headquarters for Earthquake Research Promotion 2014) (Fig. 2a). In this paper, we present results from high-resolution seismic profile data that we acquired along 15 survey lines in the central-eastern portion of the Osaka Bay, using a Mini GI air gun (15/15 in^3) and a Boomer (100/200 J) as active sources, together with multi-beam bathymetry data collected onboard the T/S Fukaemaru and R/V Onokoro (Fig. 2b). By combining with published borehole data around the bay with knowledge of deep structures imaged by previous seismic surveys, our newly acquired data documents the Late Pleistocene to Holocene deformation history at the central segment of the Osaka Bay Fault. Our results also have significant implications for changes in depositional environment, as well as for the formation of the sedimentary basin and interactions with late Quaternary climate and tectonic events in this region, situated at the southern edge of the Kinki Triangle.

2 Background and geologic setting

2.1 The 1995 Kobe (southern Hyogo prefecture) earthquake

The M_w6.9 1995 Kobe (Southern Hyogo prefecture) Earthquake (death toll: 6434) was the most destructive earthquake in Japan since the 1923 Kanto Earthquake and the 1944/1946 Nankai-Tonankai Earthquakes, second to the 2011 Tohoku-oki Earthquake (Kikuchi and Kanamori 1996; Baba and Cummins 2005; Kobayashi and Koketsu 2005; Uchida and Bürgmann 2021). The mainshock occurred at a depth of ~ 16 km beneath the Akashi Strait north of Awaji Island in the Osaka Bay, with a right lateral strike-slip focal mechanism and a WNW-ESE trending maximum compressional axis (Japan Meteorological Agency/JMA 1995; Kikuchi and Kanamori 1996; Katao et al. 1997) (Fig. 2a). The earthquake rupture propagated bilaterally towards the land in Kobe and Awaji Island along a ~ 60-km-long northeasterly trending zone consisting of multiple fault traces of the Rokko-Awaji Island Fault zone; from the Nojima and Kariya Faults to the Suma, Otsuki, Suwayama, and Gosukebashi Faults, and to the Arima-Takatsuki Fault zone (Hirata et al. 1996; Ide et al. 1996) (Fig. 2a). Dense aftershock distributions occurred along and/or near these faults, and offshore northern Awaji Island in Osaka Bay (Hirata et al. 1996; Katao et al. 1997). The propagation of the rupture produced long-period pulses in the observed fault-normal ground motions, and a "damage belt" where more than 30% of wooden-frame houses collapsed (seismic intensity VII defined by JMA) occurred along the topographic boundaries between the cities and hills in the Kobe-Hanshin area (Furumura and Koketsu 1998). The location of the damage belt deviated from the earthquake distributions and was closer to the coast, and was mainly explained by strong ground motions caused by rupture directivity from basin edge effects (Furumura and Koketsu 1998; Hallier et al. 2008; Koketsu and Miyake 2008). Field surveys have found surface ruptures occurring on a ~ 9 to 15-km-long segment of the preexisting right-lateral Nojima Fault on the Awaji Island with a maximum horizontal displacement of ~ 1.9 to 2.1 m and vertical offsets of up to ~ 1.0 to 1.2 m, whereas surface ruptures were not reported in the Kobe area (Awata et al. 1995; Ikeda et al. 1995; Nakata and Yomogida 1995; Nakata et al. 1996; Sato et al. 1998).

In response to the disastrous 1995 earthquake, the Japanese government, national and private institutes and universities conducted seismic reflection surveys to assess the structures of active faults and seismic hazards in this region (Iwabuchi et al. 1995, 2000; Yokota et al. 1997; Yokokura et al. 1998; Sato et al. 1998; Nanayama et al. 2000; Grothe et al. 2014; Itoh and Takemura 2019b). Seismic reflection surveys around the Osaka Bay have characterized the distribution of high-angle (~ 80°), NE–SW trending strike-slip/reverse faults responsible for the 1995 earthquake; the east-dipping Nojima Fault along the west coast of Awaji Island, and the west-dipping Higashiura and Kariya Faults along the east coast (Yokota et al. 1997; Sato et al. 1998) (Fig. 2a). These fault systems have likely contributed to the narrow uplift of the Awaji Island that extends to the Rokko Mountains (e.g., Huzita 1990; Kato et al. 2008). Offshore of the Awaji Island, multiple blind reverse faults have been identified within the Osaka Bay, including the ~ 70° west-dipping, NE–SW trending Osaka Bay Fault and a subsidiary fault ~ 15 km and ~ 3 to 5 km east of the island, respectively (Iwabuchi et al. 1995, 2000; Yokota et al. 1997; Yokokura et al. 1998; Sato et al. 1998; Nanayama et al. 2000) (Fig. 2a). These fault systems have likely made a significant contribution to the long-term subsidence of the basin in the footwall side (e.g., Itoh et al. 2000, 2001). Despite the proximity to the faults around the Awaji Island that ruptured during the 1995 earthquake, the Osaka Bay Fault is not reported to have ruptured during the earthquake, as inferred from mainshock and aftershock distributions, although aftershock microseismicity was observed offshore northern Awaji Island, possible along the subsidiary faults between the Kariya Fault and the Osaka Bay Fault (Hirata et al. 1996; Katao et al. 1997).

2.2 The Osaka bay fault

The Osaka Bay Fault is responsible for the deformation of the ~ 3-km-thick Late Pliocene to Quaternary sediments of the Plio-Pleistocene (< 3 Ma) Osaka Group and the Late Pleistocene-Holocene strata (colluvium, alluvium) that extend to the Osaka Basin, and the underlying Cretaceous granitic basement rocks of the Ryoke Group (e.g., Yokota et al. 1997). The deformation caused by the fault is observed in the form of thrust folding, characterized by an asymmetric anticline (~ 1 to 2 km-wide flexure) of which its forelimb becomes steeper with depth, and a broad syncline (~ 10 km wide) in the footwall side, depositing packages of growth strata (Iwabuchi et al. 1995, 2000; Yokota et al. 1997; Yokokura et al. 1998; Sato et al. 1998; Usami 2002; Grothe et al. 2014). The fault tip is not directly imaged by previous studies, although it is inferred to lie > 1 km below the seafloor based on trishear modelling (Grothe et al. 2014). The vertical displacement by the Osaka Bay Fault reaches ~ 1 km at the base of the sediments during the last ~ 3 Ma, and reaches to a total of ~ 2.5 to 3 km relative to the uplifted Awaji Island when combining with the displacements by other faults along the east coast and the Kariya and Higashiura Fault systems (e.g., Sato et al. 1998). The lateral displacement by the Osaka Bay Fault is unknown, and previous studies have not been able to clarify the strike-slip offsets from their seismic images (e.g., Yokokura et al. 1998). Although dip slip is largely supported from the geodetic principal strain axis (ESE–WNW to ENE–WSW) that is nearly perpendicular to the strike (NE–SW) of the main fault traces of the Osaka Bay Fault (Sagiya 2004; Nishimura et al. 2018, 2020) (Fig. 1b), right-lateral strike-slip faulting is also expected from the steep dips (> 70°) of these faults, and the regional earthquake focal mechanisms that show strike-slip and reverse slip senses (Hirata et al. 1996; Katao et al. 1997; Nakamukae et al. 2003; Matsushita and Imanishi 2015). The P-axes of regional focal mechanisms generally show ESE–WNW to ENE–WSW compressions, but with some complexities (e.g., NE–SW, SE–NW and N–S compressions and normal faulting), possibly due to the variable geometry of faults and/or local stress changes (Katao et al. 1997; Nakamukae et al. 2003; Matsushita and Imanishi 2015). In the northern region of the Osaka Bay, right-lateral strike slip is likely to be more dominant where the Osaka Bay Fault bends and strikes WSW–ENE parallel to the Rokko-Awaji Island Fault zones (e.g., Nakamukae et al. 2003) (Fig. 2a).

The Osaka Bay Fault can be divided into the northern, central, and southern segments based on the along-strike variations in fault geometry, that may partly be due to the structural relationship with the surrounding Rokko-Awaji Island Fault zone, the Median Tectonic Line, and the Uemachi Fault zone (Fig. 2a). Understanding how these major faults structurally link with each other is important for assessing the regional seismic hazard and the complex rupture processes that may involve movement of multiple fault strands during a single or sequential earthquake (e.g., Honda and Yomogida 2003). At the northern segment, the Osaka Bay Fault is known to splay into three strands (namely the Wadamisaki, Maya, and Rokko Island Faults), as the fault approaches the adjacent Rokko-Awaji Island Fault zone to the north (Yokokura et al. 1998; Nanayama et al. 2000). At the central segment, displacement by the Osaka Bay Fault is mainly occurring at the main fault, in addition to distribution of subsidiary faults in the eastern and western portions of the bay (Yokokura et al. 1998; Sato et al. 1998; Iwabuchi et al. 2000). In contrast, at the southern segment, the geometry of the Osaka Bay Fault changes, and is likely partitioning into several strands, as also inferred from gravity anomalies and isopach models that show complex basement morphologies and varying sediment thickness (Komazawa et al. 1996; Yokokura et al. 1998; Iwabuchi et al. 2000; Afnimar et al. 2002; Itoh et al. 2013a). However, due to the lack of seismic imaging in the southern portion of the Osaka Bay, the fault geometry at this segment is unknown. This segment has importance in the structural relationships with the Median Tectonic Line to the south, and the Uemachi Fault zone beneath the Osaka Basin to the east that is gradually bending westward towards the southern Osaka Bay (Fig. 2a; Research and Development Bureau/MEXT & DPRI 2013).

While previous seismic reflection surveys in the Osaka Bay have mostly targeted great depths of ~ 2 km below the seafloor, inferring the overall deformation structure from the basement to the sedimentary section (Iwasaki et al. 1994; Yokokura et al. 1998; Sato et al. 1998; Iwabuchi et al. 2000), the shallow structures of the faults have not been studied in detail. Previous surveys that targeted shallow depths (Hayakawa et al. 1964; Huzita and Maeda 1969; Inouchi 1990; Iwabuchi et al. 1995; Nanayama et al. 2000) have inferred the existence of multiple blind faults in the bay (e.g., Iwabuchi et al. 1995; Usami 2002), suggesting possible fault ruptures associated with the 1995 earthquake (Iwabuchi et al. 1995), but detailed studies have been limited to the northern segment of the fault close to the coast (Nanayama et al. 2000). The recent deformation history of the Osaka Bay Fault is not well constrained, together with the lack of historical earthquakes (The Headquarters for Earthquake Research Promotion 2014). Detailed constraints on the shallow structure and subsurface deformation are crucial for assessing the Holocene fault slip rates and seismic risks that may involve tsunami generation at the seafloor (e.g., Nakamura 1999; Kawata et al. 2005) and strong ground motions in the sedimentary basin, and is the primary focus of this study.

2.3 Depositional environment and late quaternary sedimentary sequence around the Osaka Bay

The Osaka Bay is situated at the eastern edge of the Seto Inland Sea in western Japan (Figs. 1, 2). The Seto Inland Sea has generally shallow water depths of ~ 30 to 50 m, and is connected with the Pacific Ocean via the Kitan and Naruto Straits to the southeast and the Hoyo Strait to the west, and connects with the Japan Sea via the Kanmon Strait, consisting of multiple enclosed bays (Osaka, Harima-nada, Hiuchi-nada, Hiroshima, Iyo-nada, and Suo-nada Bays) laterally linked by narrow straits (Akashi, Bisan-seto, Kurushima and Tsurushima Straits) (e.g., Yasuhara 2008; Saito et al. 2016). While the paleo-Seto Inland Sea is thought to have originated from repeated, episodic rifting events in the Asian continent since the Eocene–Oligocene (e.g., Nakajima 2018), partially overprinted by Setouchi volcanism in the Mid-Miocene (~ 15 Ma) (Kimura et al. 2005; Tatsumi 2006), the current Seto Inland Sea is overlain by

Plio-Pleistocene (< 3 to 6 Ma) sedimentary basins (e.g., Mizuno 2018) that have likely interacted with the contemporary compressional regime associated with the subduction of the Philippine Sea Plate and reactivation of the Median Tectonic Line since the Late Miocene (Kamata and Kodama 1994; Kimura et al. 2005, 2014).

Past fluctuations in relative sea-levels and consequent opening of the straits and formation of bays have resulted in a dynamic depositional environment in and around the Osaka Bay (e.g., Irizuki et al. 2001; Yasuhara et al. 2004; Yasuhara 2008; Masuda and Itomoto 2015). The sedimentary sequence underlying the Osaka Bay and Osaka Basin consists of alternating marine and non-marine strata of the Plio-Pleistocene Osaka Group, overlain by Late Pleistocene colluvium and Holocene alluvium (e.g., Huzita and Maeda 1984; Itihara eds. 1993; Itoh and Takemura 2019a). While the Osaka Group and colluvium sediments are partially exposed at the surface in the surrounding mountains and elevated fluvial terraces in the Osaka Basin, the Holocene alluvium is distributed more broadly, forming the coastal alluvial fan and floodplains (e.g., Itoh and Takemura 2019a) (Fig. 2a). The stratigraphy of the sedimentary sequence in this region has been characterized on the basis of tephrochronology, magnetostratigraphy, pollen assemblage, and marine clay beds (individually numbered "Ma 1"–"Ma13") correlated to eustatic sea level high-stands and marine oxygen isotope records (e.g., Itihara 1960, 1993; Yoshikawa et al. 1987; Itoh et al. 2000, Itoh and Takemura 2019a), in addition to regional unconformities (e.g., Huzita 1990), established from outcrops and deep drilling results in the Osaka Basin and coastal areas in Kobe (e.g., Ikebe et al. 1970; Mitamura et al. 1998, 2000).

The Late Pleistocene colluvium in this region consist of terrigenous fluvial sands and gravels during the Last Glacial Period, containing marine clay beds "Ma 12" and "Ma 11", correlated to Marine Isotope Stages (MIS) 3 and 5, respectively, whereas the major composition of the Holocene alluvium is the "Ma13" clay, silt, and sand, correlated to MIS 1, consisting of inner bay deposits and tidal delta sediments (e.g., Masuda 1992; Nanayama et al. 2001). Based on detailed facies analysis and dense ^{14}C dating from sediment cores offshore Kobe and Kansai Airport, and along the coastal edge of the Osaka Basin (e.g., Nakaseko 1987; Masuda 1992; Irizuki et al. 2001; Yasuhara et al. 2004; Kitada et al. 2001), the sediments beneath the Osaka Bay are interpreted to have transitioned from fluvial, estuary to inner bay deposits during a rapid rising stage of sea level (transgression) starting at ~ 11 ka when sea level was -51 m below modern sea level (Masuda and Miyahara 2000; Nanayama et al. 2001; Masuda and Itomoto 2015). This period was followed by tidal delta deposition consisting of sand and mud, originating from the Akashi Strait that was formed at ~ 9.7 ka, when sea level was − 30 m below modern sea level (Masuda and Miyahara 2000). The sedimentary sequence was then overlain by bay-floor deposits during marine flood and sea level high-stands that occurred at ~ 5.3 to 5 ka, during which sea level was + 1 to 2 m above modern sea level (Masuda et al. 2000). The most recent sediments consist of coarse bedload deposits transported by strong tidal currents from the Akashi Strait, and the uppermost marine clay which are primarily floodplain suspension loads transported by the Yodo and Mukogawa River systems from the Osaka Basin, inferred to have deposited following periods of marine regression that started at ~ 1 to 1.7 ka (Masuda and Miyahara 2000; Nanayama et al. 2001).

The distribution of contemporary seafloor sediments in the Osaka Bay is not homogeneous, where marine clay is restricted to the eastern portion of the bay, whereas coarser sediments are more dominant in the central to western part of the bay (Huzita and Maeda 1969; Inouchi 1982; Inouchi 1990; Fujiwara et al. 1989; Yashima 1992; Masuda and Miyahara 2000; Nanayama et al. 2001). Sediment distribution is affected by wave and tidal currents operating in the bay, producing various erosional and depositional processes near the straits and in the shelf (e.g., Yashima 1992; Ikehara and Kinoshita 1994). In a longer timescale, the sediments are also affected by coastal tectonic deformation, forming the sedimentary basin (e.g., Sato et al. 2017). In this study, we investigate the shallow structure and distribution of seafloor sediments in the Osaka Bay, and document the geometries of sequence stratigraphic surfaces and deformation, providing constraints on the dynamic interactions of tectonics, sea level fluctuations, and tidal currents that led to the formation of the late Quaternary sedimentary basin in this region.

3 Methods

We conducted our surveys in the central-western portion of the Osaka Bay along E–W trending lines that are nearly perpendicular to the fault traces of the Osaka Bay Fault (e.g., Iwabuchi et al. 1995; Yokokura et al. 1998; Usami 2002; National Institute of Advanced Industrial Science and Technology 2012), and along N–S trending lines that intersect with the E–W trending lines to characterize the three-dimensional structure (Fig. 2).

We acquired high-resolution seismic profile data along eight survey lines using a Sercel Mini-GI airgun with volume reducers (15 in^3 generator and 15 in^3 injector) as active source, equipped at Kobe University onboard the T/S Fukaemaru (449 t). The shot spacing was 10 s with a record length of 8 s, every 23 m while the vessel ran at an average speed of 4.5 knot. The towed streamer cable had 6 channels with 6.25 m hydrophone group intervals and a total length of 150 m. The received seismic reflection signals were recorded at a 1 ms sampling rate by the DAQLink 4 seismograph (Seismic Source). The locations of receivers and shots were determined by GPS. The acquired data was processed with static correction, band-pass filter, amplitude recovery, 12.5 m binning, normal moveout correction using constant velocity (1500 m/s), and Stolt migration. The data are also visualized with an automatic gain control. The frequency range for band-pass filter was set to 50–450 Hz.

We also acquired high-resolution seismic profile data along seven survey lines onboard the R/V Onokoro (9.7 t), using a Boomer (Applied Acoustics, AA251) as active source, with an energy output of 100 J or 200 J per shot, equipped at the Geological Survey of Japan (Suzuki et al. 2021). The shot spacing was 1 s with a record length of 800 ms, every 1.56 m while the vessel ran at an average speed of 3–3.5 knot. The towed streamer cable had 16 channels with 3.125 m hydrophone group intervals, combined to a total length of 50 m. The received seismic reflection signals were recorded at a 0.125 ms sampling rate by the GeoEel multi-channel digital streamer system (Geometrics), and the locations of receivers and shots were determined by GPS. The acquired data was processed with the sequence of format conversion and trace edit, geometry application to trace header, band-pass filter, gain recovery, deconvolution, velocity analysis, normal moveout corrections, CMP stacking, and data visualization after a second band-pass filter. The frequency range for band-pass filter was set to 300–2000 Hz.

At the vicinity of our seismic reflection profile data, high-resolution multi-beam bathymetry data covering ~ 170 km^2 around the survey area was acquired onboard the T/S Fukaemaru, using a Kongsberg EM 712 (1.0° × 1.0°) Multi-beam Echo Sounder, operating at sonar frequencies in the 40–100 kHz range, and swath coverage of 140° with 400 beams by dual swath (Figs. 3, 4). To account for submetric error on the beam positioning, the system was interfaced with Differential Global Positioning System and motion Reference Unit (Kongsberg) for attitude determination and motion compensation. The in situ surface water sound speed was acquired for calibrating proper beam steering, by sound velocity probes equipped at on-keel station located near the multi-beam transducers, and by CTD profiling of the water column. Bathymetry and backscatter data were processed with the Seafloor Information System (SIS) and CARIS HIPS & SHIPS software. Noise reduction due to artificial instrumental spikes and poor-quality beam exclusion were carried out by swath editing and de-spiking tools.

We interpret lithostratigraphy and sequence boundaries and assign the ages in our seismic profiles by correlating with published borehole data acquired in the vicinity of our survey lines offshore Kobe city and Kansai Airport, and along the coastal plain of the Osaka Basin (Nakaseko 1987; Masuda 1992; Masuda et al. 2000; Masuda and Miyahara 2000; Nanayama et al. 2000, 2001; Kitada et al. 2001; Masuda and Itomoto 2015). We use observed stratigraphic geometries and age constraints from boreholes to estimate fault displacements and slip rate.

4 Results

4.1 Bathymetry and backscatter data

Figures 3, 4, 5 shows the acquired multi-beam bathymetry data (10-m horizontal grid spacing) acquired in this study, plotted with the M7000 digital bathymetry data published by the Japan Hydrographic Association. The seafloor of the Osaka Bay has generally shallow water depths (10–20 m) at the eastern region, abruptly transitioning into deeper water depths (30–65 m) at the central-western part of the bay, across a concave-shaped inner shelf and slope (Fig. 3a). The deepest portion of the bay (> 70 m water depth) is restricted to the northwest and northcentral regions offshore northern Awaji Island, which gradually shallows towards the south (Fig. 3b). Seafloor morphology is most complex near the Akashi Strait to the north and the Kitan Strait to the south, and is characterized by multiple pockets of bathymetric lows and highs, interpreted to be caused by depositional and erosional processes linked to tidal currents (e.g., Inouchi 1990; Yashima 1992; Ikehara and Kinoshita 1994) (Fig. 3b). The Akashi Strait has a water depth of up to ~ 100 m, indicating dominant erosion; previous studies have documented bedrock granites exposed at the seafloor beneath the strait (Huzita and Maeda 1984). Coincidently, the epicenter of the 1995 Kobe Earthquake is also at this vicinity, where the Nojima and Kariya Faults (Rokko-Awaji Island Fault zone) run across northern Awaji Island towards Kobe city (e.g., Kato et al. 2008) (Fig. 2a).

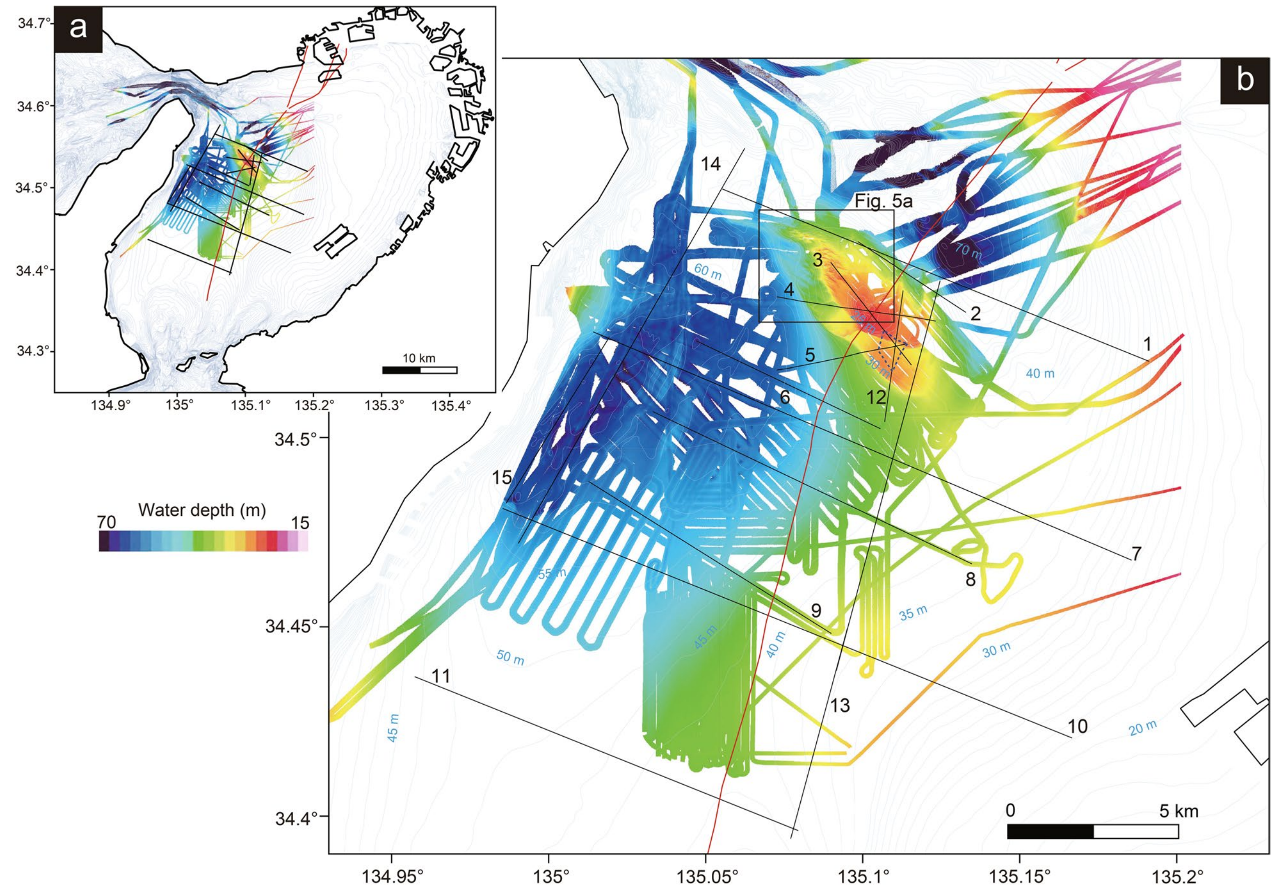

Fig. 3 Multi-beam bathymetry data (10-m horizontal grid spacing) acquired in this study, plotted with the M7000 digital bathymetry data (light blue contours) by the Japan Hydrographic Association. (**a**) Location of survey area. (**b**). Close-up of survey area. Grey lines: seismic reflection survey lines (#1–15). Red line: Trace of the Osaka Bay Fault. Box shows region of distinct sand wave structures closed-up in Fig. 5a. Blue dotted square: area of negative polarity reflector observed along Lines 3, 5, and 12 (Sect. 4.2.1)

At about 6 km offshore northern Awaji Island, our bathymetry data clearly image a NW–SE trending bathymetry high region (27–30 m water depth), extending 6.4 km (long axis) × 2.6 km (short axis) wide with relative heights of 5–10 m (Fig. 3b). This bathymetric high, locally called the "Okinose" sand bank (Inouchi 1990; Yashima 1992; Kojima 2020), is associated with ESE–WNW trending lineation fabrics interpreted to be sand wave bedforms comprising a subaqueous dune complex (Figs. 3b, 5a). The sand waves are oriented approximately 12–45 degrees to the long axis of the Okinose sand bank, and are characterized by asymmetric shapes with steeper southern flanks (Fig. 5b). The largest sand waves are up to ~ 5 m in height with 100–150 m wavelengths and 1–5 km along-crest length, and are concentrated on the northwestern region, whereas the smaller waves are < 1 m high with a wavelength less than 20 m and > 1 km along-crest length (Fig. 5b). The morphology of the western and southern part of the dune complex are bounded by steep edges and sharp steps in bathymetry, characterized by an NW–SE trending ~ 5 m-high escarpment in the western side, and WNW-ESE trending ~ 5 m-high escarpment in the southern side (Fig. 3b). These escarpments intersect at 34.53° N, 135.10° E south of the summit of the bathymetric high, with an angular contact between the western and southern flanks (Fig. 3b). The Okinose sand bank is interpreted to be a sand dune complex formed by strong tidal currents from the Akashi Strait (Inouchi 1990; Yashima 1992; Kojima 2020). To the east and west of the dune complex, the water depth deepens to ~ 60 to 78 m (Fig. 3b). The regional depressions to the east of the Okinose sand bank is an area locally named "Yokose", and are likely forming seafloor cauldrons and

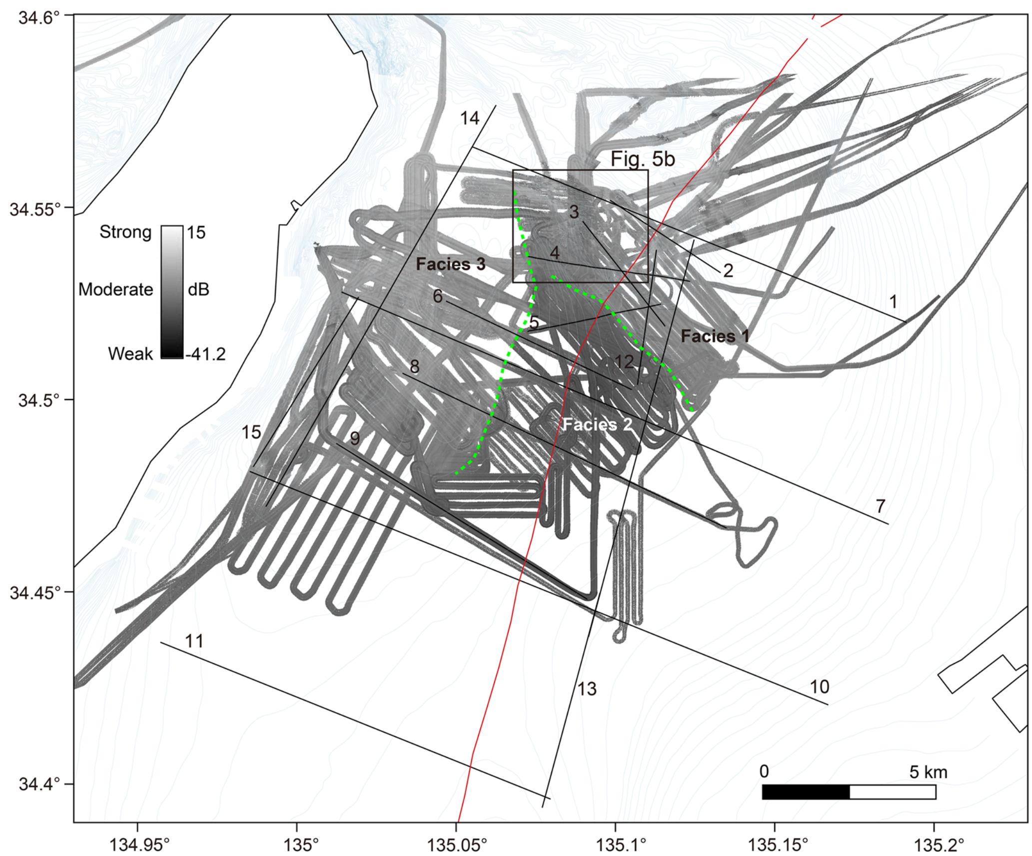

Fig. 4 Backscatter intensities acquired in this study linearly mapped to a greyscale mosaic with a resolution of 1 m and dynamic mosaic range of -41.2–15 dB. Light blue contours: M7000 digital bathymetry data. Three characteristic backscatter imagery facies are identified (boundary traced by green-dotted lines). Facies 1: heterogeneous, moderate reflective (light grey) facies. Facies 2: homogeneous, weak-to-moderate reflective (dark grey) facies. Facies 3: homogeneous, moderate-to-strong reflective (light grey) facies. Black lines: seismic reflection survey lines (#1–15). Red line: Trace of the Osaka Bay Fault. Box shows region of distinct sand wave structures closed-up in Fig. 5b

scour hollows eroded by tidal currents (Inouchi 1990; Yashima 1992; Ikehara and Kinoshita 1994).

Figure 4 shows the backscatter intensities acquired in this study linearly mapped to a greyscale mosaic with a lateral resolution of 1 m and dynamic mosaic range of − 41.2 to 15 dB. The compensated backscatter imagery, normalized at reference levels on flat seafloor, provide relative intensities for qualitative analyses. We define three characteristic backscatter imagery facies at the seafloor within our survey area: (1) a heterogeneous, moderate reflective (grey; − 20 to 10 dB) facies ("backscatter facies 1"), (2) a homogeneous, weak-to-moderate reflective (dark grey; − 40 to − 20 dB) facies ("backscatter facies 2"), and (3) a homogeneous, moderate-to-strong reflective (light grey; − 20 to 10 dB) facies ("backscatter facies 3") (Fig. 4).

The region of backscatter facies 1 is associated with the Okinose sand bank. Notably, the moderate backscatter

(See figure on next page.)

Fig. 5 Close-up of bathymetry and backscatter imageries across the Okinose sand bank. (**a**) Bathymetry data image the morphology of the sand bank, with characteristic ENE–WSW trending lineation fabrics interpreted to be sand wave bedforms. (**b**) Elevation of bedforms across i–ii (left), and iii–iv (right) shown in (a). The sand waves generally have steeper southern flanks. Note smaller-scale waves in southern portion of the dune. (**c**) Backscatter intensities detect the morphology of individual sand waves (blue arrows: example of larger-scale sand waves, yellow arrows: example of smaller-scale sand waves). The backscatter imagery provides fine details of the small-scale sand waves that extends to the southern flanks of the dune complex. Note occasionally patchy distributions. Black box: example of heterogeneous, high backscatter intensities not related to sand waves

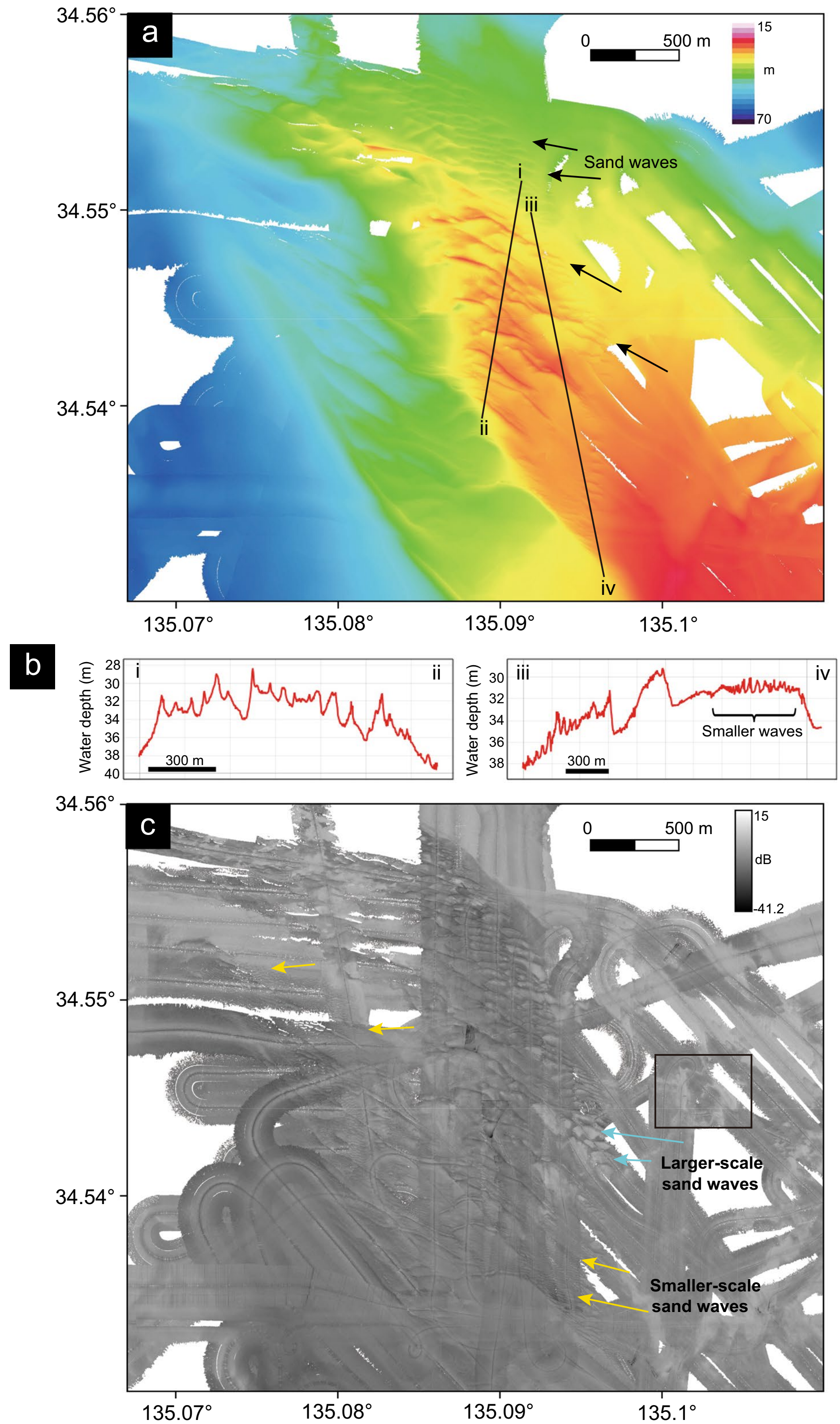

Fig. 5 (See legend on previous page.)

reflectivity extends east and southeast of the sand bank (Fig. 4). The sand wave bedforms and morphology of the dune complex are also clearly detected in the backscatter imagery (Fig. 5c). The backscatter over the sand waves is generally weak (dark grey to grey), whereas low backscatter level (dark grey) is observed on the sand wave crests, and strong levels (light grey) in the flanks and troughs, with occasionally patchy distributions (Fig. 5c). Patches of heterogenous, high backscatter intensities (light grey) not associated with sand waves are also present (Fig. 5c). Across the local depressions northeast of the Okinose sand bank, patches of low backscatter intensities (dark grey) are observed, indicating a complex distribution of seafloor sediments and erosion (Figs. 4, 5c).

The crest of the southern escarpment of the Okinose sand bank is visible from the lineations of low backscatter levels (dark grey) (Fig. 4). At the southern flank of the Okinose bank, the water depths gradually deepen from ~ 35 to ~ 40 m, and a sharp transition from backscatter facies 1 to facies 2 is observed at the foot of the dune (Fig. 4). The seafloor south of the Okinose bank corresponds to the region of backscatter facies 2, which is distributed broadly and has an overall smooth bathymetry (< 55 m water depth) (Fig. 4).

Westward from the region of facies 1 and 2, a sharp transition from backscatter facies 2 to facies 3 is observed from east to west at our northern and central survey areas (Fig. 4). Backscatter facies 3 is associated with the gradual increase of water depths (> 60 m) as the seafloor forms a local embayment (Fig. 3b). At the southern area, in contrast, the boundary between backscatter facies 2 and 3 is gradually curved westward along the southern rim of the embayment as the water depths shallow (Fig. 4). Here, backscatter facies 2 is continuously distributed from east to west.

Generally, the intensities of acoustic signals backscattered from the seafloor indicate seafloor characteristics such as interface roughness, acoustic impedance, and surficial heterogeneity, related to seafloor composition and small-scale topographies (e.g., Lamarche et al. 2011; Yu et al. 2015). The increase in backscatter intensities with grain size have been noted in previous studies (e.g., Goff et al. 2000; Collier and Brown 2005; Ferrini and Flood 2006), and is likely perceptible in this study. We attribute the high backscatter intensity facies 1 and 3 to represent coarser sediments such as sands and gravels, and lower backscatter intensity facies 2 to represent finer sediments such as silt and clay.

4.2 Seismic reflection data

The Osaka Bay Fault is inferred to run NE–SW across the western-central part of the Osaka Bay (Fig. 2a). In this section, we interpret the structures below the seafloor imaged by seismic reflection data obtained from a Mini-GI airgun (imaged to ~ 1000 ms, ~ 700 m below the seafloor) and a Boomer (imaged to ~ 150 ms, ~ 50 to 80 m below the seafloor) as active sources (Sect. 3). Due to challenges in seafloor multiples in the data and scattering of signals across higher-angle strata at greater depths, we use the upper < 300 to 500 ms (~ 200 to 400 m below the seafloor) to resolve for confidence in structural interpretations, and assume a constant velocity of 1500 m/s for depth conversion. Based on the bandpath width of 300–2000 Hz for Boomer and 50–450 Hz for airgun (Sect. 3), we estimate the accuracy of depth measurement for Boomer to range ~ 0.4 to 2.5 m, and ~ 3 to 17 m for airgun. In this section, we divide our survey areas into the northern, central, and southern regions, and constrain the geometry of observed structures and stratal dips (Figs. 6, 7, 8, 9, 10, 11, 12, 13, 14, 15, 16, 17, 18, 19, 20, 20, 21). We trace distinct seismic reflectors and assign seismic units based on stratal terminations (angular disconformities) and characteristics of seismic reflections (Figs. 6, 7, 8, 9, 10, 11, 12, 13, 14, 15, 16, 17, 18, 19). The area of greatest folding, itself a proxy for fault shear at a particular stratigraphic level in growth strata above the Osaka Bay Fault is mostly contained between the anticlinal fold axis and the synclinal fold axis (Figs. 7, 8, 9, 10, 13, 14, 15, 16, 17). The widths of fold limbs in this study are measured from the range of width between the anticlinal fold axis and synclinal fold axis in the imaged depths.Fence diagrams are constructed to observe the spatial distributions of seismic units and their geometries across our study area (Fig. 21). To interpret the surface expressions of structures and distribution of seafloor sediments, we combine our observations with bathymetry and backscatter data (Sect. 4.1) (Figs. 3, 4). For the deeper sections, we identify seismic horizons at the base of representative seismic reflectors that are traceable among all the sections (Horizons C1–C5; Figs. 6, 7, 8, 9, 10, 11, 12, 13, 14, 15, 16, 17, 18, 19). In Sect. 5.1.2, the ages of these deeper horizons are estimated by comparing with the age-correlated reflectors of marine clay marker beds by Grothe et al. (2014) along previously acquired deep seismic lines (Yokokura et al. 1998), OD-B (Iwasaki et al. 1994; Yokokura et al. 1998; Iwabuchi et al. 2000).

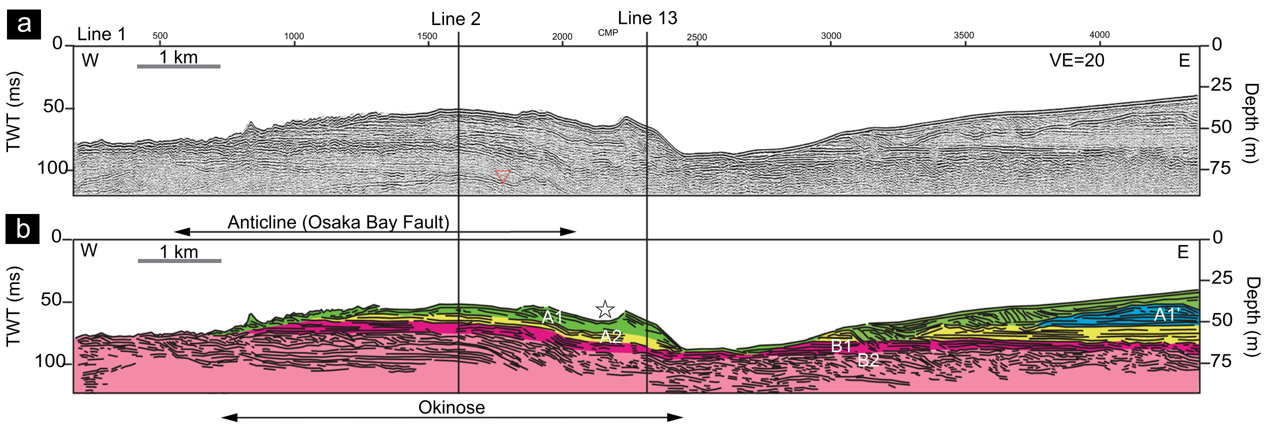

Fig. 6 Seismic profile Line 1 (Boomer). TWT: two-way travel time. Vertical line represents location of cross lines. (**a**) Uninterpreted image (post-stack, vertical exaggeration = 20). Red triangle: representative seafloor multiple. (**b**) Trace of seismic reflectors in (a) and interpreted image. Star shows location of sediment thickness measurement in Fig. 24. Unit A1 exhibits chaotic internal structure with a wavy and irregular base, indicating an erosional contact (CMP #3000–3800). Continuous tilting of strata by the hanging wall anticline of the Osaka Bay Fault is observed to reach to shallow depths

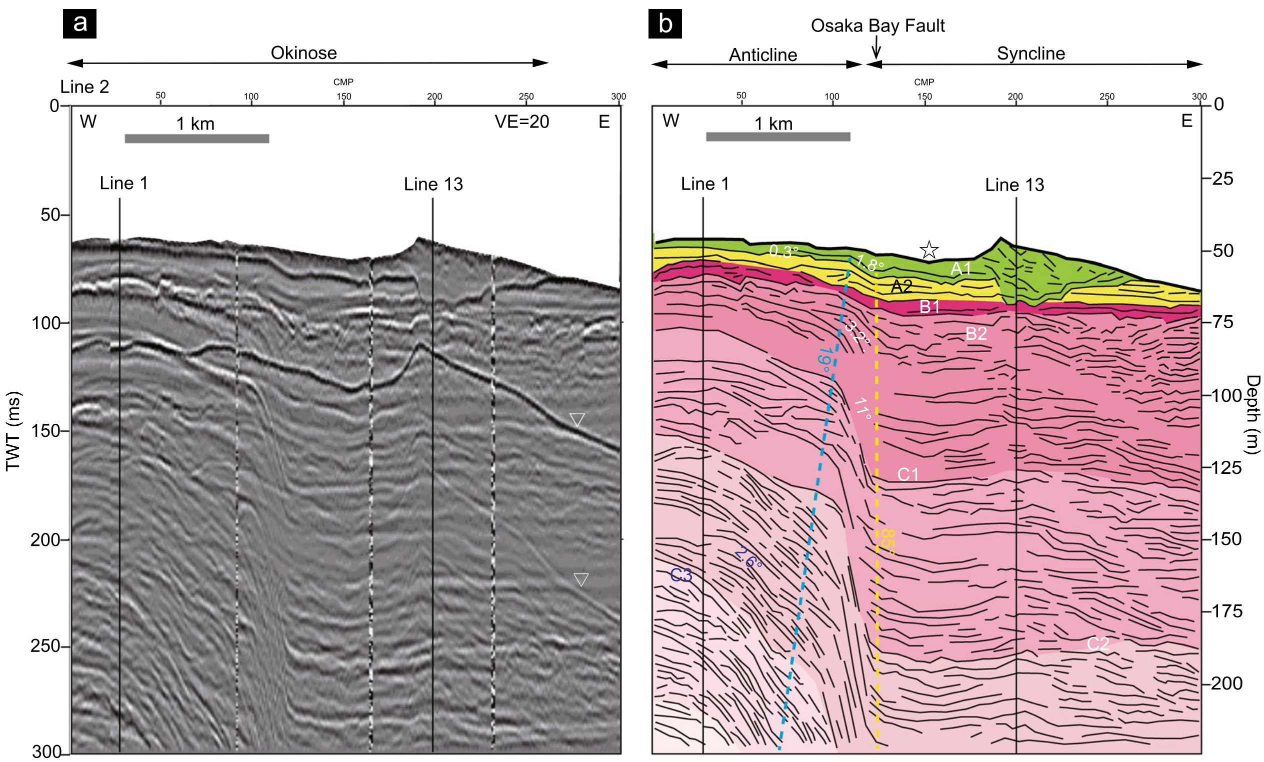

Fig. 7 Seismic profile Line 2 (Airgun). TWT: two-way travel time. Vertical line represents location of cross lines. (**a**) Uninterpreted image (post-stack, vertical exaggeration = 20). White triangle: representative seafloor multiple. (**b**) Trace of seismic reflectors in (a) and interpreted image. The seismic units at deeper sections (light to dark pink) are assigned at the base of representative seismic reflectors traceable with other sections. Blue dotted line: anticlinal axial surface. Yellow dotted line: synclinal axial surface. Dip measurements of representative layers are shown. Star shows location of sediment thickness measurement in Fig. 24. The base of Unit A1 is wavy and irregular, indicating an erosional contact (CMP #120–260). Continuous tilting of strata by the hanging wall anticline of the Osaka Bay Fault is observed to reach to shallow depths

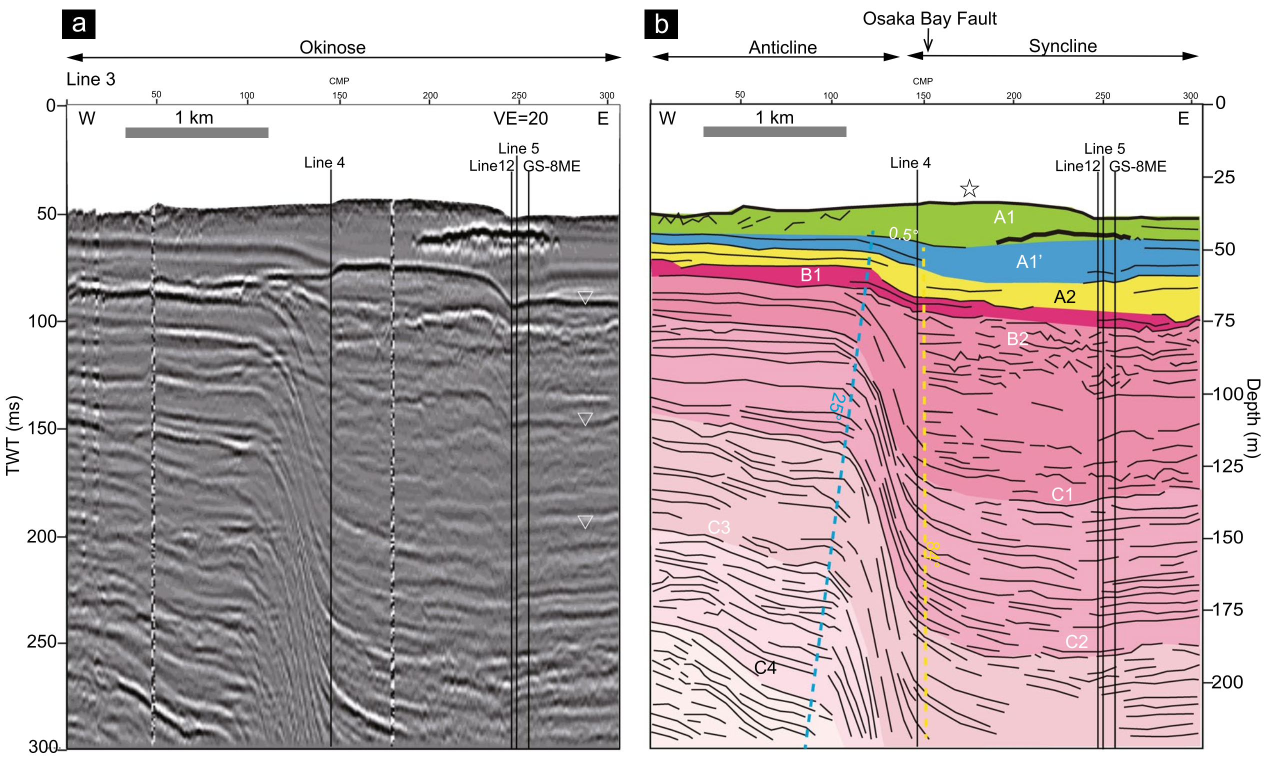

Fig. 8 Seismic profile Line 3 (Airgun). TWT: two-way travel time. Vertical line represents location of cross lines. (**a**) Uninterpreted image (post-stack, vertical exaggeration = 20). White triangle: representative seafloor multiple. Note the presence of high-amplitude negative polarity reflector at shallow depths (CMP #180–270). (**b**) Trace of seismic reflectors in (a) and interpreted image. The seismic units at deeper sections (light to dark pink) are assigned at the base of representative seismic reflectors traceable with other sections. Blue dotted line: anticlinal axial surface. Yellow dotted line: synclinal axial surface. Dip measurements of representative layers are shown. Star shows location of sediment thickness measurement in Fig. 24. Continuous tilting of strata by the hanging wall anticline of the Osaka Bay Fault is observed to reach to shallow depths

4.2.1 Northern survey area

At our northern survey area, our E–W, NE–SW, and NW–SE sections that cross oblique to high-angle to the structure of the Osaka Bay Fault show a monoclinal panel consisting of a coupled anticline and syncline (Figs. 3b, 6, 7, 8, 9, 10). We observe a distinct fold axis of the hanging wall anticline buried beneath recent sediments above the Osaka Bay Fault. The anticlinal axial surface, or growth axial surface, dips 12–25° to the west, separating shallowly-dipping reflectors to the west from a 0.4–13° east-dipping panel which comprises the ~ 0.3–2.0-km-wide forelimb to the east (Figs. 6, 7, 8, 9, 10). The anticline has a 0.2–0.9° west-dipping backlimb, which dips gentler than the forelimb (Figs. 6, 7, 8, 9, 10). The synclinal fold axial surface, in contrast, dips ~ 84–85° to the east along Lines 2 and 3, and dips ~ 75° to the west along Lines 4 and 5, and separates the forelimb to the west from shallowly-dipping reflectors to the east (Figs. 7, 8, 9, 10). The seismic reflectors are continuously folded across these fold axes, thinning the strata across the fold, with the forelimb and backlimb of the anticline progressively steepening with depth, and the overall monocline widening at shallower depths. It is noted that Lines 1–3 cross at high-angle to the structure of the Osaka Bay Fault, reflecting the geometry of the fault-normal fold and its greater synclinal fold axial surface (84–85°), compared to Lines 4 and 5, which cross oblique to the strike of the fault (Fig. 2a).

At our northern sections, the uppermost sequence consists of a 7–14-m-thick seismically transparent package with occasional chaotic fabric, associated with the local topographic high (Okinose sand bank) imaged from bathymetry data (Sect. 4.1), which we assign as Unit A1 (Figs. 6, 7, 8, 9, 10). The base of Unit A1 is erosive along the northern edge of the Okinose bank (Lines 1 and 2) (Figs. 6, 7), whereas continuous deposition is observed at the center of the dune (Lines 3–5) (Figs. 8, 9, 10).

Along Lines 3–5, the section (up to ~ 11 m thick) beneath Unit A1 consists of parallel reflectors contrasting with the less-reflective Unit A1, which we assign as Unit A1' (Figs. 8, 9, 10). Between this transition, a localized section of high-amplitude negative polarity reflector is observed, indicating the presence of a low velocity

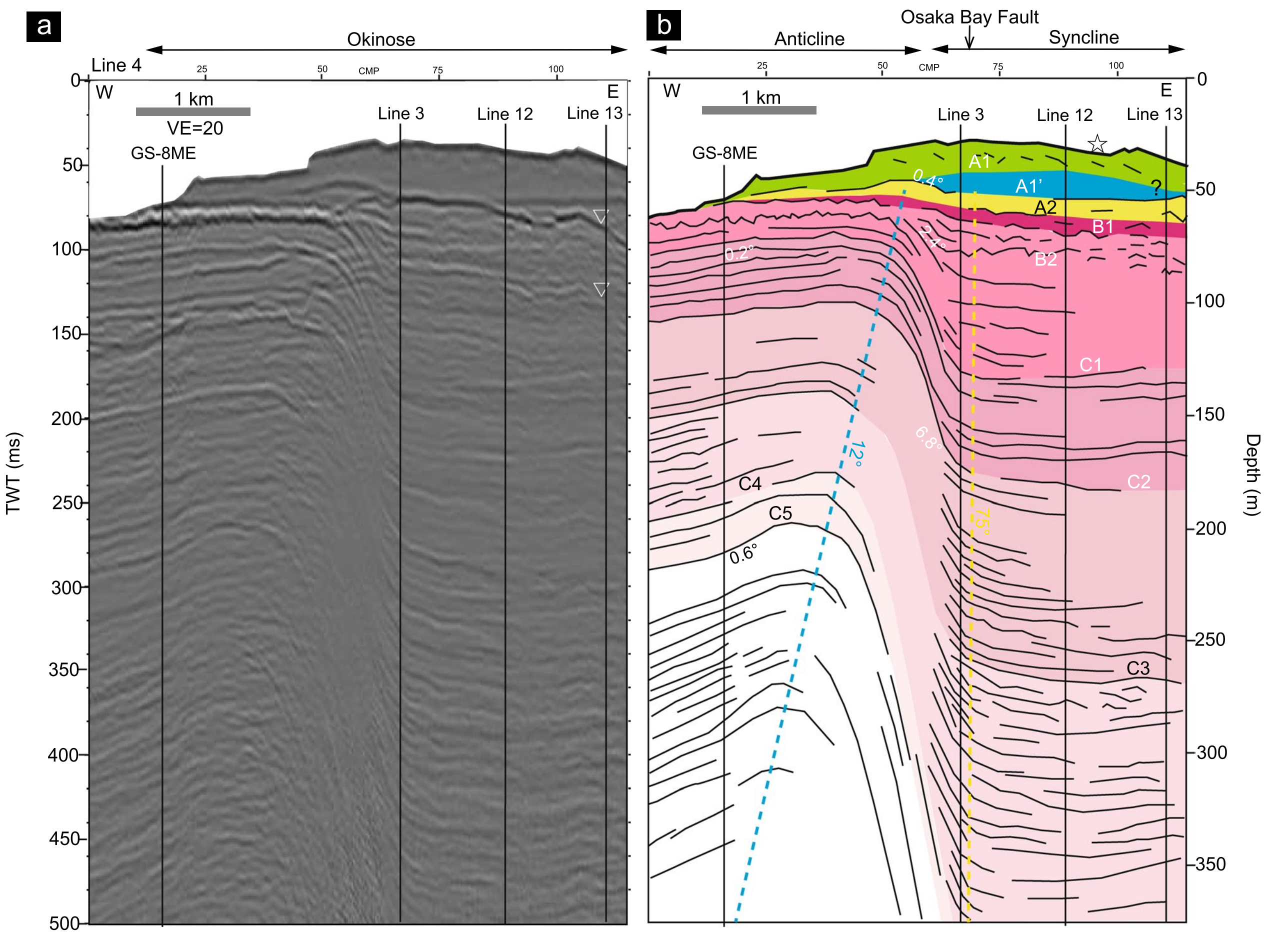

Fig. 9 Seismic profile Line 4 (Airgun). TWT: two-way travel time. Vertical line represents location of cross lines. (**a**) Uninterpreted image (post-stack, vertical exaggeration = 20). White triangle: representative seafloor multiple. (**b**) Trace of seismic reflectors in (a) and interpreted image. The seismic units at deeper sections (light to dark pink) are assigned at the base of representative seismic reflectors traceable with other sections. Blue dotted line: anticlinal axial surface. Yellow dotted line: synclinal axial surface. Dip measurements of representative layers are shown. Star shows location of sediment thickness measurement in Fig. 24. Units A1, A1' and A2 onlap onto Unit B1, underlain by continuous tilting of strata by the hanging wall anticline of the Osaka Bay Fault

material relative to the surrounding strata (Lines 3, 5, 12; Figs. 8, 10, 11).

Unit A1' is underlain by a 13–16-m-thick sequence of thin, well-defined parallel seismic reflections, which we assign as Unit A2 (Figs. 6, 7, 8, 9, 10). Beneath this section, < 5 m-thick sequences of continuous, high-amplitude reflections are present, which we assign as Unit B1. At the base of Unit B1, sequences of discontinuous and wavy reflectors are observed, contrasting with the sequence above, which we classify as Unit B2 (Figs. 6, 7, 8, 9, 10). At the deeper section of Unit B2, well-defined continuous reflectors are present. Towards the western side of our sections, Units A1, A2 and B1 gradually thin, and Unit B2 is exposed at the seafloor, as the water depth increases west of the Okinose bank (Figs. 9, 10).

Along Lines 1 and 2, the base of Unit A1 is wavy and irregular, indicating an erosional contact (Figs. 6, 7). Here, Unit A2 is eroded at the base of Unit A1, and Unit A1' is absent or only partially distributed. Erosion is most significant across the bathymetric depression east of the Okinose bank, and the uppermost sequence (10–11 m) at the eastern side of Line 1 exhibits chaotic internal structure, overlying the < 20-m-thick sub-horizontal Units A1' and A2 (Line 1; Fig. 6).

Our N-S sections (Lines 12, 13) show that Unit A1 terminates south of the Okinose bank, and a 13–14-m-thick sequence of thin, well-defined parallel seismic reflections, which we assign as Unit A1', is exposed at the seafloor (Figs. 11, 12). The sub-horizontal base of Unit A1' underlain by Unit A2 is well-imaged as clear seismic reflectors from north to south. Here, Units A2, B1, and B2 are continuously distributed below Units A1 and A1' (Figs. 11, 12). From the fence diagram crossing our N-S and E–W sections, these units are spatially correlated (Fig. 21;

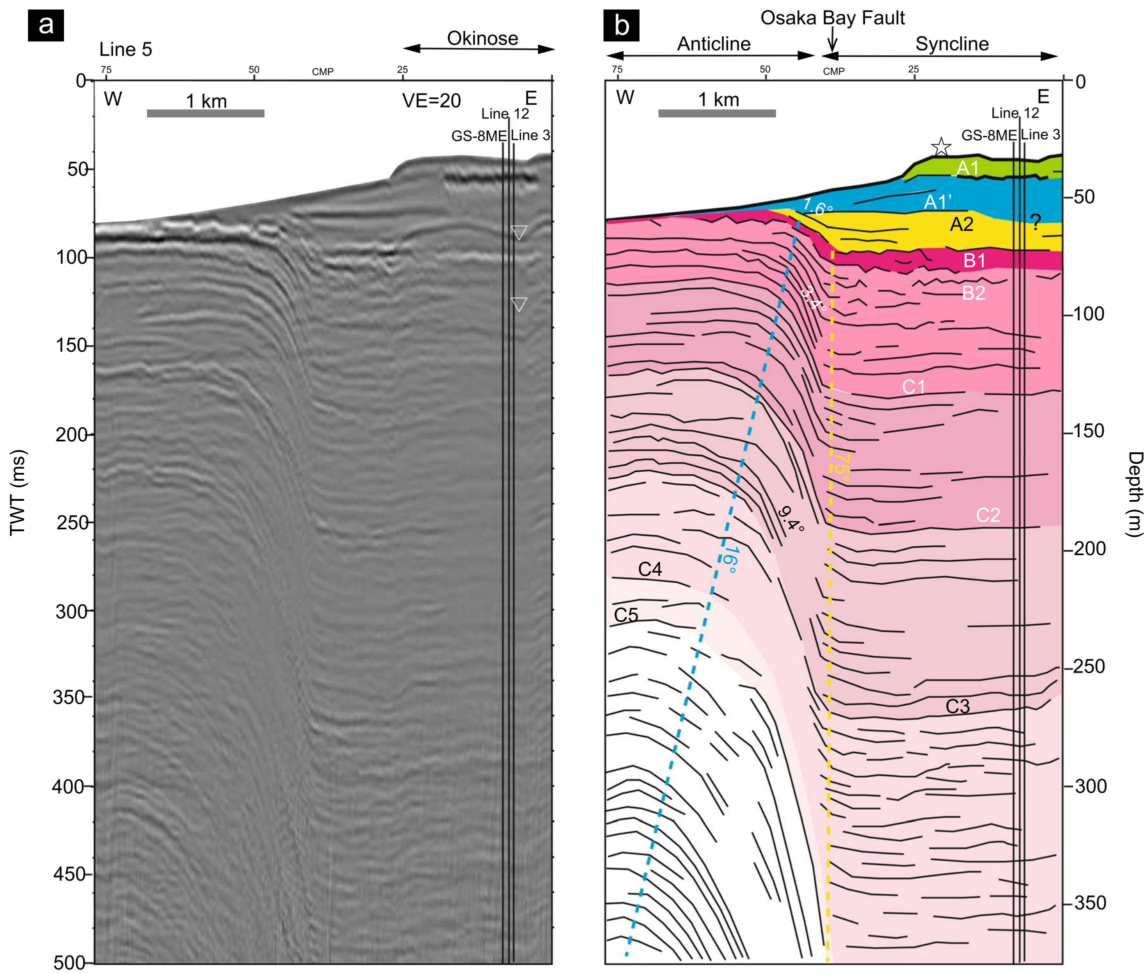

Fig. 10 Seismic profile Line 5 (Airgun). TWT: two-way travel time. Vertical line represents location of cross lines. (**a**) Uninterpreted image (post-stack, vertical exaggeration = 20). White triangle: representative seafloor multiple. Note the presence of high-amplitude negative polarity reflector at shallow depths (CMP #1–20). (**b**) Trace of seismic reflectors in (a) and interpreted image. The seismic units at deeper sections (light to dark pink) are assigned at the base of representative seismic reflectors traceable with other sections. Blue dotted line: anticlinal axial surface. Yellow dotted line: synclinal axial surface. Dip measurements of representative layers are shown. Star shows location of sediment thickness measurement in Fig. 24. Units A1' and A2 onlap onto Unit B1, underlain by continuous tilting of strata by the hanging wall anticline of the Osaka Bay Fault

Additional file 1: Fig. S1). The top of Unit A1' beneath the Okinose bank (the boundary between A1 and A1'), however, is discontinuous and likely erosive (Figs. 6, 7, 8, 9, 10).

Our NW–SE sections (Lines 1, 2, 3) cross at high-angle to the structure of the Osaka Bay Fault, and nearly parallel to the long axis of the Okinose bank and to the strike of the shelf northeast of our sections (Figs. 3b, 6, 7, 8). Here, continuous tilting of strata of Units A1, A1', A2, B1, and B2 are observed from near the seafloor, revealing the shallow deformation by uplift on the hanging wall anticline forelimb above the Osaka Bay Fault. We measure 0.5–3.2° east-dipping strata and shallowly-dipping strata separated by a synclinal axial surface within these units, associated with distinct thinning of sediments in the hanging wall and thickening in the footwall (Figs. 6, 7, 8). Here, the uplifted stratigraphy in the hanging wall is preserved from erosion, and the continuous deformation by the anticline to the shallow subsurface is clearly observed.

Our E–W and NE–SW sections (Lines 4, 5), by contrast, cross at an oblique angle to the structure of the Osaka Bay Fault, and also oblique to the shelf and to the long axis of the Okinose bank (Figs.3b, 9, 10). From these sections, we observe progressive onlap and overlap of Units A1, A1', and A2 onto Unit B1. Here, Units A1 and A1' dip sub-horizontally to the west, sub-parallel to the dip of the current seafloor (Figs. 9, 10). In contrast, tilting of strata are observed in Units A2, B1, and B2, which we interpret to represent the shallow deformation by the hanging wall anticline forelimb above

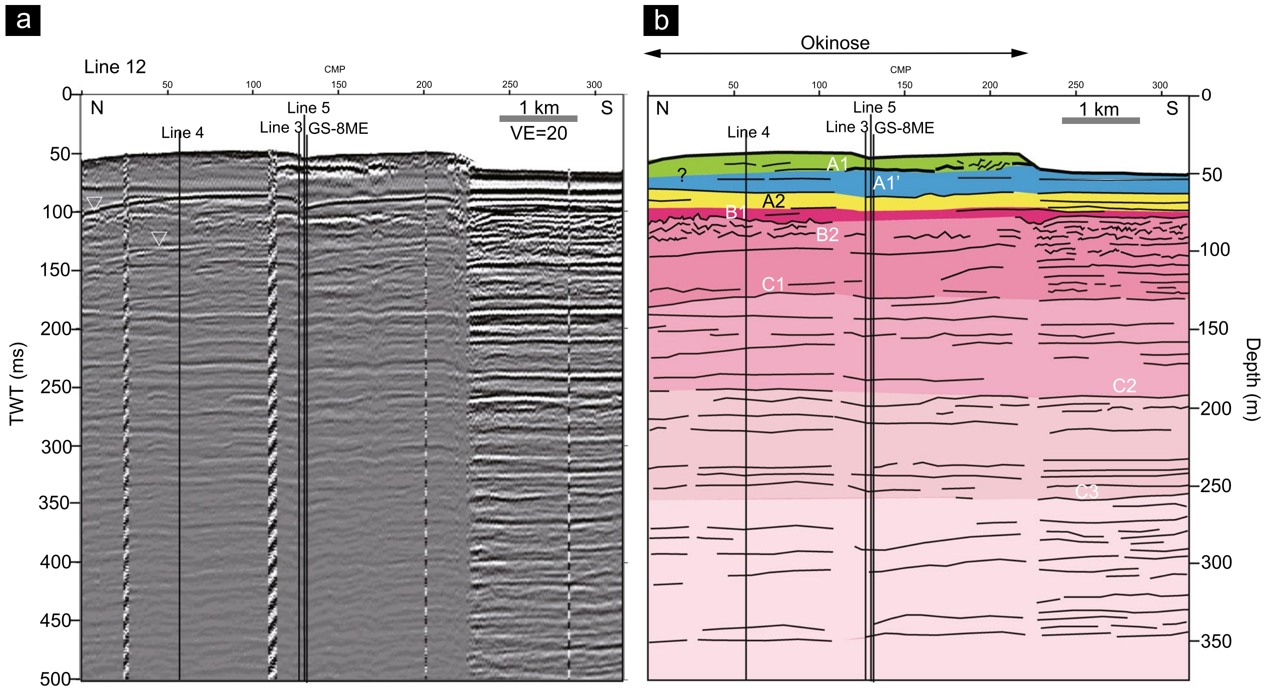

Fig. 11 Seismic profile Line 12 (Airgun). TWT: two-way travel time. Vertical line represents location of cross lines. (**a**) Uninterpreted image (post-stack, vertical exaggeration = 20). White triangle: representative seafloor multiple. Note the presence of high-amplitude negative polarity reflector at shallow depths (CMP #120–180). (**b**) Trace of seismic reflectors in (a) and interpreted image. The seismic units at deeper sections (light to dark pink) are assigned at the base of representative seismic reflectors traceable with other sections

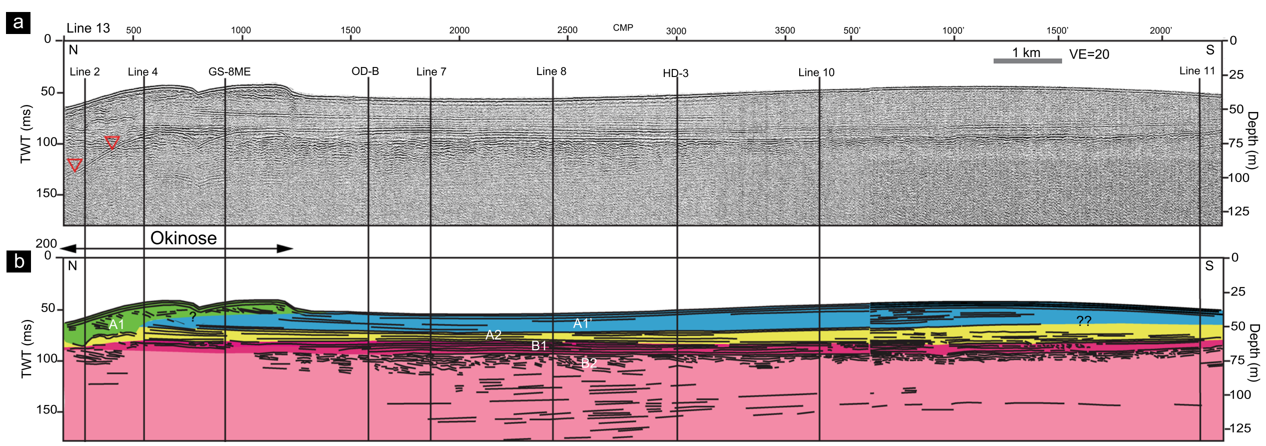

Fig. 12 Seismic profile Line 13 (Boomer). TWT: two-way travel time. Vertical line represents location of cross lines. (**a**) Uninterpreted image (post-stack, vertical exaggeration = 20). Red triangle: representative seafloor multiple. (**b**) Trace of seismic reflectors in (a) and interpreted image

(See figure on next page.)

Fig. 13 Seismic profile Line 6 (Airgun). TWT: two-way travel time. Vertical line represents location of cross lines. (**a**) Uninterpreted image (post-stack, vertical exaggeration = 20). White triangle: representative seafloor multiple. (**b**) Trace of seismic reflectors in (a) and interpreted image. The seismic units at deeper sections (light to dark pink) are assigned at the base of representative seismic reflectors traceable with other sections. Blue dotted line: anticlinal axial surface. Yellow dotted line: synclinal axial surface. Dip measurements of representative layers are shown. Star shows location of sediment thickness measurement in Fig. 24. Note the onlap of Units A1' and A2 onto Unit B1, underlain by continuous tilting of strata by the hanging wall anticline of the Osaka Bay Fault. Unit A1' is also likely truncated by Unit A2 (CMP #100–160)

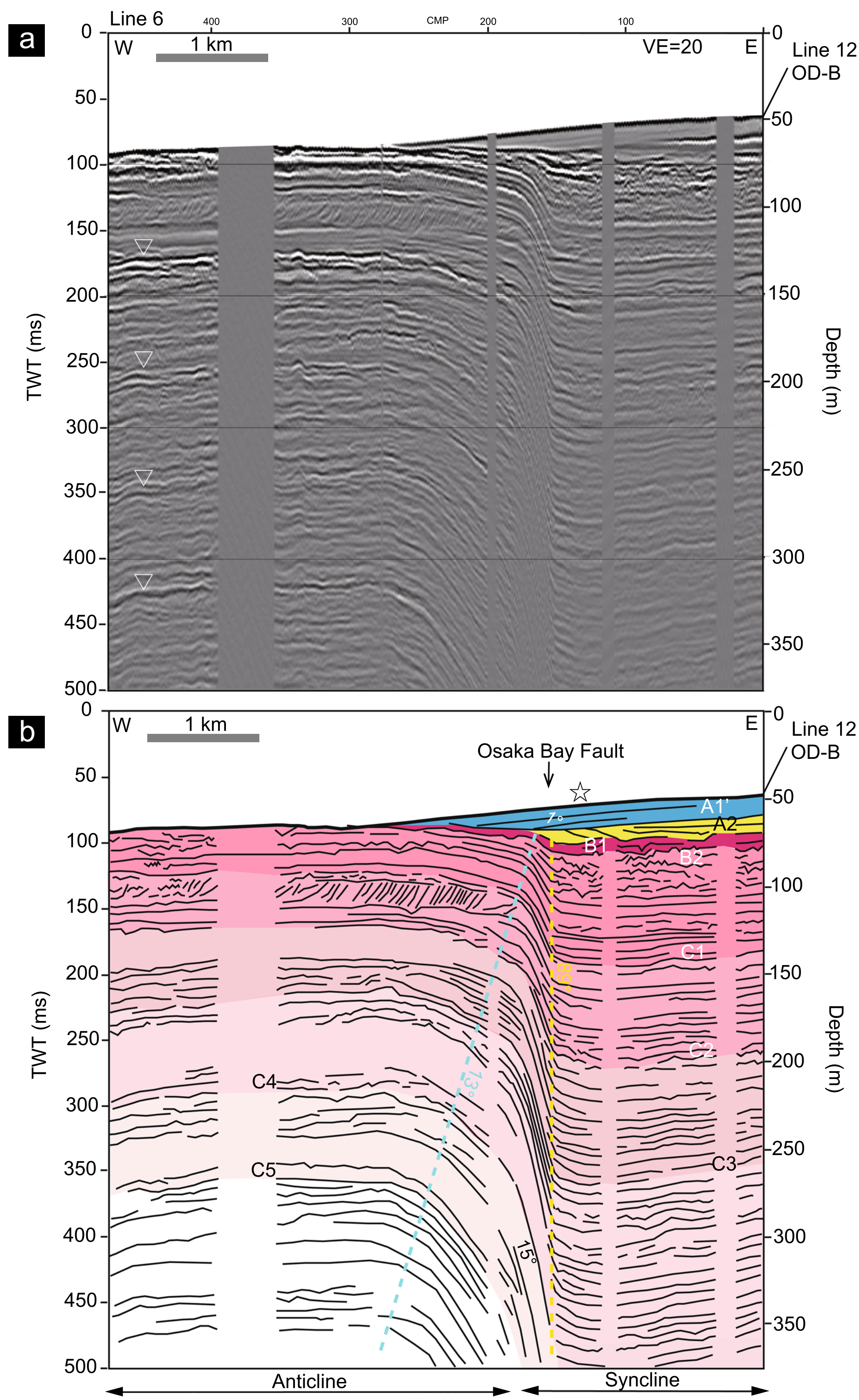

Fig. 13 (See legend on previous page.)

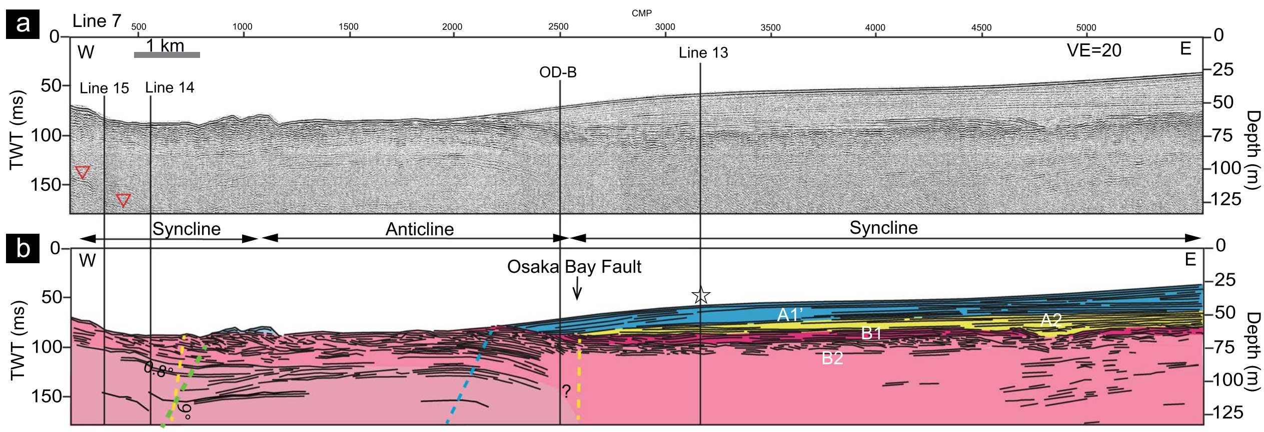

Fig. 14 Seismic profile Line 7 (Boomer). TWT: two-way travel time. Vertical line represents location of cross lines. (**a**) Uninterpreted image (post-stack, vertical exaggeration = 20). Red triangle: representative seafloor multiple. (**b**) Trace of seismic reflectors in (a) and interpreted image. Blue dotted line: estimated anticlinal axial surface. Yellow dotted line: estimated synclinal axial surface. Star shows location of sediment thickness measurement in Fig. 24. Note the onlap of Units A1' and A2 onto Unit B1, underlain by continuous tilting of strata by the hanging wall anticline of the Osaka Bay Fault. An additional synclinal fold structure is observed west of the hanging wall anticline (CMP #400–1200). The widths of the syncline and anticline reported in the main text are estimated from the width of the two points where the folded strata intersect with the inferred undeformed stratal dip (Additional file 1: Figs. S2, S3)

the Osaka Bay Fault (Figs. 9, 10). We measure 0.4°–3.4° east-dipping strata and shallowly-dipping strata separated by a synclinal axial surface within these units, associated with distinct thickening of sediments from the hanging wall to the footwall. The onlap of Units A1, A1' and A2 onto Unit B1 infer major sequence stratigraphic surfaces. At the deeper section of Unit B2, folded strata are continuously observed in the hanging wall and footwall.

4.2.2 Central survey area

At our central survey area, our NW–SE sections (Lines 6–10) cross at oblique to high-angle to the structure of the Osaka Bay Fault, and nearly perpendicular to the shelf east of our sections (Figs. 3b, 13, 14, 15, 16, 17). Our seismic sections show a monoclinal panel bounded by synclinal and anticlinal axial surfaces beneath the seafloor. We observe a distinct fold axis of the hanging wall anticline above the Osaka Bay Fault, separating a ~ 0.2 to 15° east-dipping panel which comprise the ~ 0.1–3.7-km-wide forelimb to the east, from shallowly-dipping reflectors to the west (Figs. 13, 15, 16). This anticlinal axial surface dips 13–25° to the west. Notably, the dip of the forelimb is gentler in the south (0.2–5.2°) (along Lines 8 and 9) (Figs. 15, 16), compared to the north (1–15°) (Line 6) (Figs. 13). Towards the eastern side on the footwall, our sections (Lines 7, 10) image the strata gradually tilting 0.2°–0.8° to the west, forming a broad syncline with a gentler dip than the hanging wall anticline (Figs. 14, 17). This synclinal fold axis dips ~ 89° to the west along Line 6, whereas it dips 85°–87° to the east along Lines 8 and 9, separating shallowly-dipping reflectors to the east from the forelimb to the west (Figs. 15, 16). Our sections also image the 0.4°–1.4° west-dipping backlimb of the hanging wall anticline above the Osaka Bay Fault (Figs. 15, 16). The seismic reflectors are continuously folded across these fold axes, thinning the hanging wall strata across the fold and with the dips of tilted strata in the forelimb and backlimb progressively steepening with depth (Figs. 13, 14, 15, 16, 17). The deeper sections west of the backlimb dip east, forming an additional synclinal fold structure buried by overlying sediments along Line 7 (Fig. 14). This structure may relate to the subsidiary fault between the Kariya and Osaka Bay Faults reported by previous studies (Yokokura et al. 1998; Iwabuchi et al. 2000) (Fig. 2a). This eastern synclinal fold axis dips ~ 8.6° to the west, and separates shallowly-dipping reflectors to the east from ~ 0.8° east-dipping panel to the west (Fig. 14). Overall, our sections show that the monocline above the Osaka Bay Fault at shallow depths consists of a coupled ~ 4.4 to 4.5 km wide anticline bounded by a broad ~ 11 km wide syncline to the east, and a narrow ~ 2.6 km wide syncline to the west (Figs. 14, 17; Additional file 1: Figs. S2, S3).

The uppermost ~ 31-m-thick sequences in the footwall are on-lapping the underlying tilted strata; these sequences are deposited only on the eastern side of our sections (Figs. 13, 14, 15, 16, 17). Here, Unit A1 is absent, and the observed sequences are characterized by thin, parallel reflectors similar to Units A1' and A2 at the northern survey area, and the bases of Units A1' and A2 are correlated with our N-S sections (Figs. 12, 13, 14). However, the top of Unit A1' is not correlated from north to south, and Unit A1' at the central

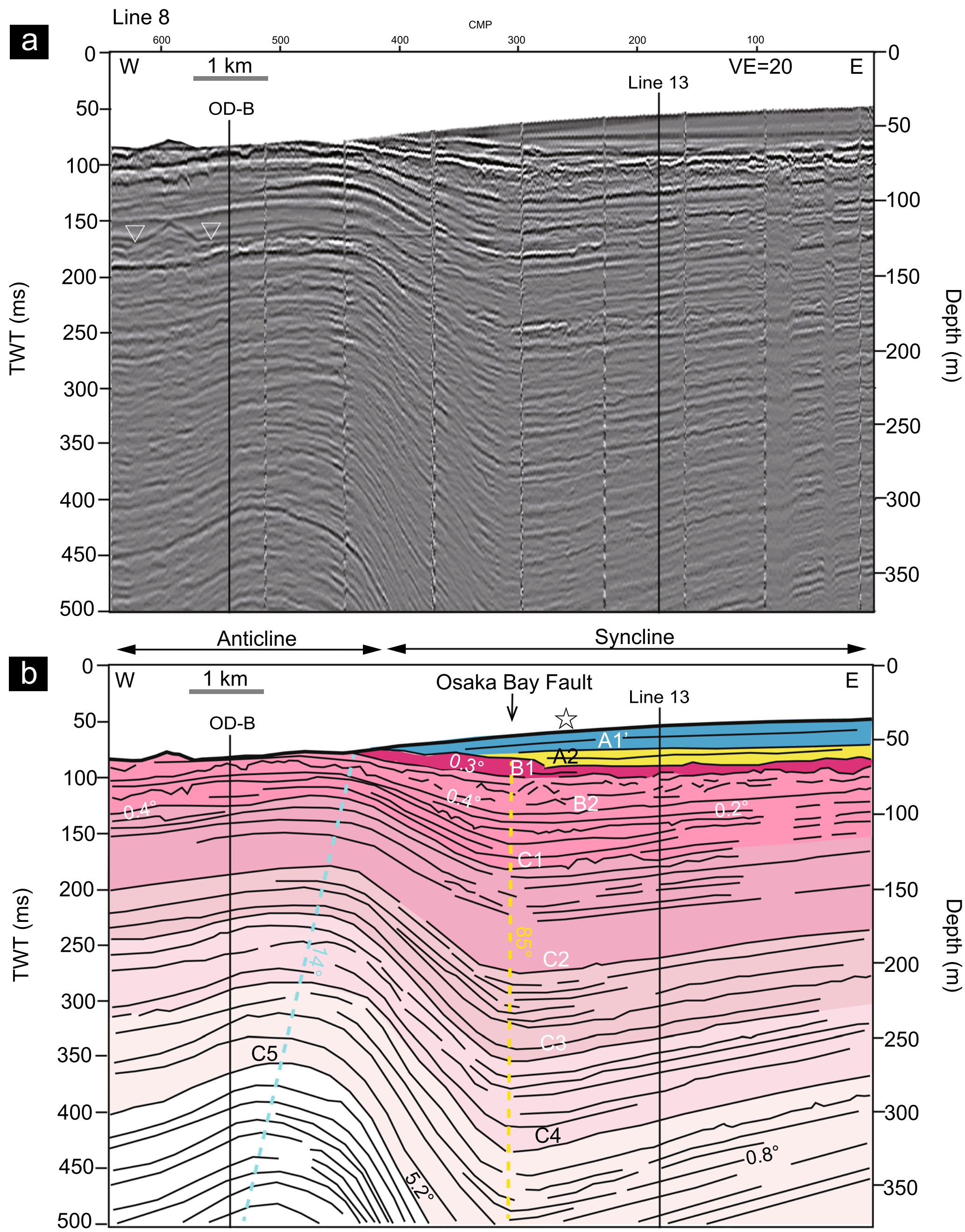

Fig. 15 Seismic profile Line 8 (Airgun). TWT: two-way travel time. Vertical line represents location of cross lines. (**a**) Uninterpreted image (post-stack, vertical exaggeration = 20). White triangle: representative seafloor multiple. (**b**) Trace of seismic reflectors in (a) and interpreted image. The seismic units at deeper sections (light to dark pink) are assigned at the base of representative seismic reflectors traceable with other sections. Blue dotted line: anticlinal axial surface. Yellow dotted line: synclinal axial surface. Dip measurements of representative layers are shown. Star shows location of sediment thickness measurement in Fig. 24. Note the onlap of Units A1' and A2 onto Unit B1, underlain by continuous tilting of strata by the hanging wall anticline of the Osaka Bay Fault

survey area is 16–22-m thick, deposited to the surface (Figs. 12, 13, 14, 15, 16, 17). Unit A1' is relatively undeformed, onlapping and truncated by the underlying 9–15-m-thick sequence of Unit A2, indicating some erosion (Figs. 13, 17). The strata of Unit A1' dip ~ 0.1° to the west, sub-parallel to the dip of the current seafloor (Figs. 13, 14, 15, 16, 17). In contrast, we measure 0.06–0.2° east-dipping strata and ~ 0.1° west-dipping strata separated by a synclinal axial surface within Unit A2 along Lines 6, 8, 9, and 10, which we attribute to the shallow deformation via the hanging wall anticline forelimb above the Osaka Bay Fault (Figs. 13, 15, 16, 17). We interpret the observed stratal termination and truncation of Unit A2 below Unit A1' to represent an erosional sequence stratigraphic surface. Near the eastern edge of our sections, an additional downlap surface may also be present at the shallow portion of Unit A1', although the imaging is not clear (Figs. 14, 17).

At the western side of our sections in the hanging wall, the 4–11-m-thick tilted sequence below Unit A2 is exposed at the seafloor, and is on-lapped by Units A1' and A2 (Figs. 13, 14, 15, 16, 17). This sequence is characterized by well-defined high-amplitude reflections, which we assign as Unit B1. We measure 0.2–1° east-dipping strata and ~ 0.14° west-dipping strata separated by a synclinal axial surface within Unit B1 on the hanging wall anticline forelimb (Figs. 13, 14, 15, 16, 17). The stratal termination and onlap of Units A1' and A2 above Unit B1 infer a major sequence boundary. Notably, the geometry of the boundary between Units A2 and B1 is wavy and irregular, indicating an erosional contact (Figs. 13, 14, 15, 16, 17). Here, thinning of strata in the hanging wall and thickening in the footwall within Unit B1 are obscured due to erosion in the footwall.

Our E–W sections and bathymetry data show a gradual westward increase in water depth, in a direction nearly perpendicular to the shelf to the east, with a deeper bathymetry in the hanging wall and shallower bathymetry in the footwall of the Osaka Bay Fault (Figs. 3b, 13, 14, 15, 16, 17). The shallower water depth in the eastern regions coincides with the deposition of Units A1' and A2 on the footwall side, which are absent or thinner in the western regions on the hanging wall. The observed variations in sediment thickness may partly be explained by enhanced erosion due to uplift by the fault in the hanging wall and larger sediment accommodation in the footwall due to subsidence. Furthermore, the clear difference in stratal dips observed between the folded strata (e.g. Units A2 and B1) and the shallow strata (Unit A1') sub-parallel to the current dip of the seafloor, suggest additional processes at shallow depths (Figs. 13, 17). Here, additional, non-tectonic surface processes such as tidal currents operating in the bay and sea-level fluctuations across the shelf, are also likely playing a major role in creating the variations in sediment thickness (Sect. 5.2).

Beneath Unit B1, sequence of wavy and discontinuous, irregular reflections is present, which we assign as Unit B2, underlain by well-defined continuous reflections at the deeper section (Figs. 13, 14, 15, 16, 17). Along Lines 6–8, Unit B1 is eroded at the seafloor, exposing Unit B2 on the hanging wall (Figs. 13, 14, 15). By contrast, south of these sections along Lines 9 and 10, Unit B1 is preserved at the seafloor, overlying Unit B2 (Figs. 16, 17). The contact between Units B1 and B2 is also observed in our N-S sections (Lines 15 and 16) at the hanging wall side, where the southern sub-horizontal sequence of Unit B1 is underlain by ~ 0.2° southward dipping sequence of Unit B2, associated with the overall southward thickening of strata (Figs. 18, Additional file 1: Fig. S4). At the deeper sections of Unit B2, the southward tilting of strata (~ 0.6°) becomes progressively steeper with depth, indicating that these structures are tectonically driven, showing an increase in uplift to the north (Figs. 18, Additional file 1: Fig. S4). The on-lap of Unit B1 onto Unit B2 observed from the N-S section may suggest a significant age gap between Units B1 and B2 (Fig. 18). The southward thickening of strata is coincident with the gradual southward shallowing in water depth shown by bathymetry; the northward dip of the seafloor is contrary to the southward dip of the underlying strata, indicating additional variations in surface processes (e.g., erosion by tidal currents) (Figs. 3b, 18). The deepest regions coincide where Unit B1 is eroded at the seafloor, exposing Unit B2, whereas the shallower region preserves Unit B1 at the seafloor (Figs. 3b, 18).

4.2.3 Southern survey area

Our E–W section (Line 11) at our southernmost survey area is located where the bathymetry shallows southward of the northern embayment, at an oblique angle to the inferred structure of the Osaka Bay Fault (Figs. 3b, 19). Units A1', A2, B1, and B2 have similar seismic characteristics as those in the central and northern survey areas, and are traceable along our N-S section (Lines 13 and 14) (Figs. 12, 18). Notably, the boundary between Units B1

(See figure on next page.)

Fig. 16 Seismic profile Line 9 (Airgun). TWT: two-way travel time. Vertical line represents location of cross lines. (**a**) Uninterpreted image (post-stack, vertical exaggeration = 20). White triangle: representative seafloor multiple. (**b**) Trace of seismic reflectors in (a) and interpreted image. The seismic units at deeper sections (light to dark pink) are assigned at the base of representative seismic reflectors traceable with other sections. Blue dotted line: anticlinal axial surface. Yellow dotted line: synclinal axial surface. Dip measurements of representative layers are shown. Star shows location of sediment thickness measurement in Fig. 24. Note the onlap of Units A1' and A2 onto Unit B1, underlain by continuous tilting of strata by the hanging wall anticline of the Osaka Bay Fault

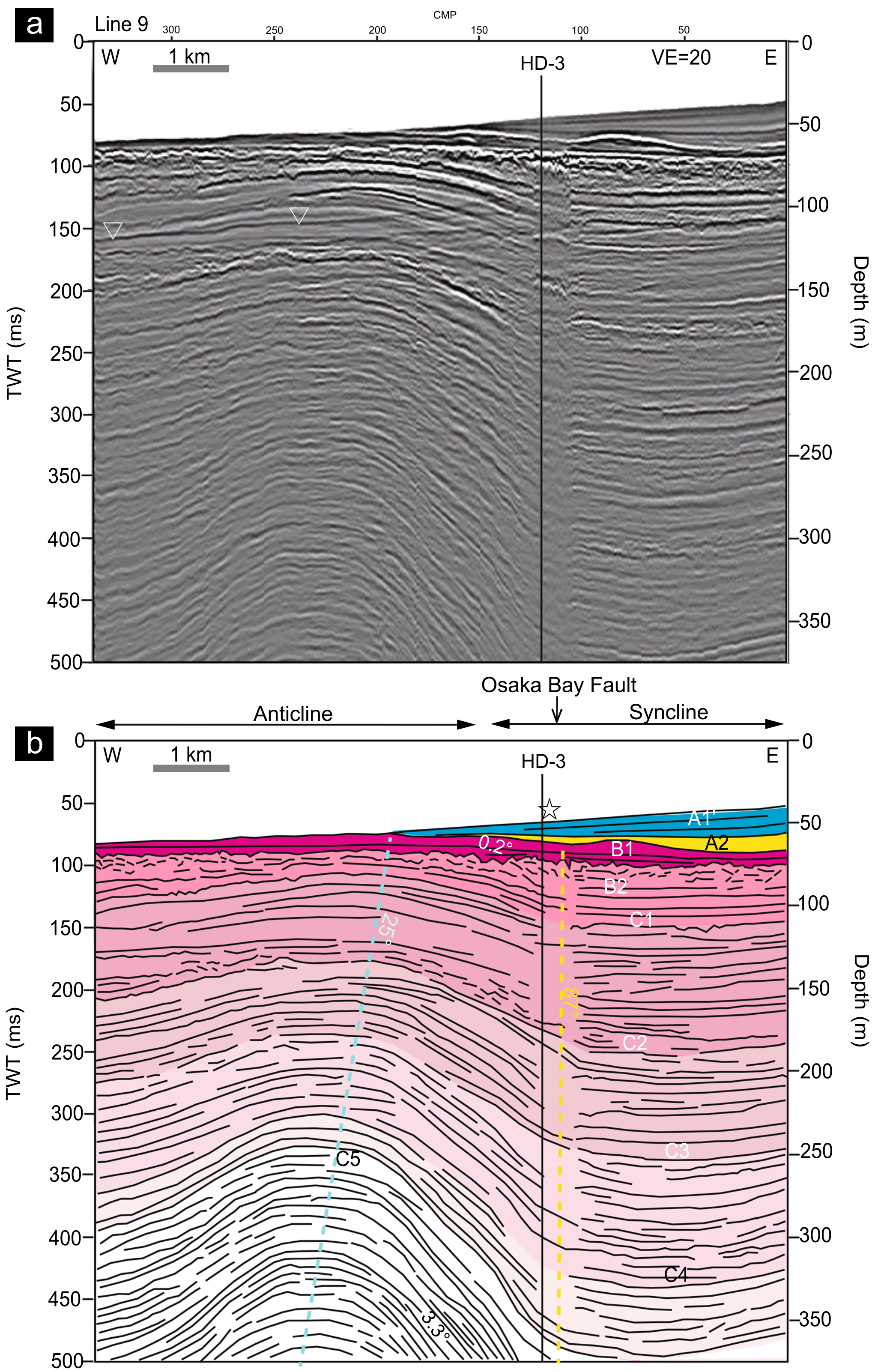

Fig. 16 (See legend on previous page.)

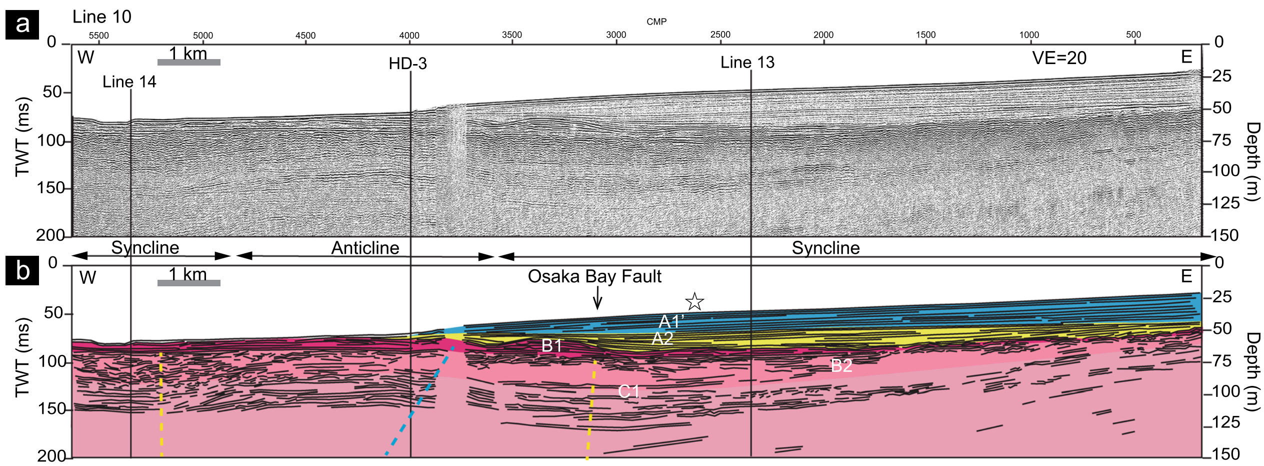

Fig. 17 Seismic profile Line 10 (Boomer). TWT: two-way travel time. Vertical line represents location of cross lines. (**a**) Uninterpreted image (post-stack, vertical exaggeration = 20). (**b**) Trace of seismic reflectors in (a) and interpreted image. The seismic units at deeper sections (light to dark pink) are assigned at the base of representative seismic reflectors traceable with other sections. Blue dotted line: estimated anticlinal axial surface. Yellow dotted line: estimated synclinal axial surface. Star shows location of sediment thickness measurement in Fig. 24. Note the onlap of Units A1' and A2 onto Unit B1, underlain by continuous tilting of strata by the hanging wall anticline of the Osaka Bay Fault. An additional synclinal fold structure is observed west of the hanging wall anticline (CMP #3500–3700). The widths of the syncline and anticline reported in the main text are estimated from the width of the two points where the folded strata intersect with the inferred undeformed stratal dip (Additional file 1: Figs. S2, S3)

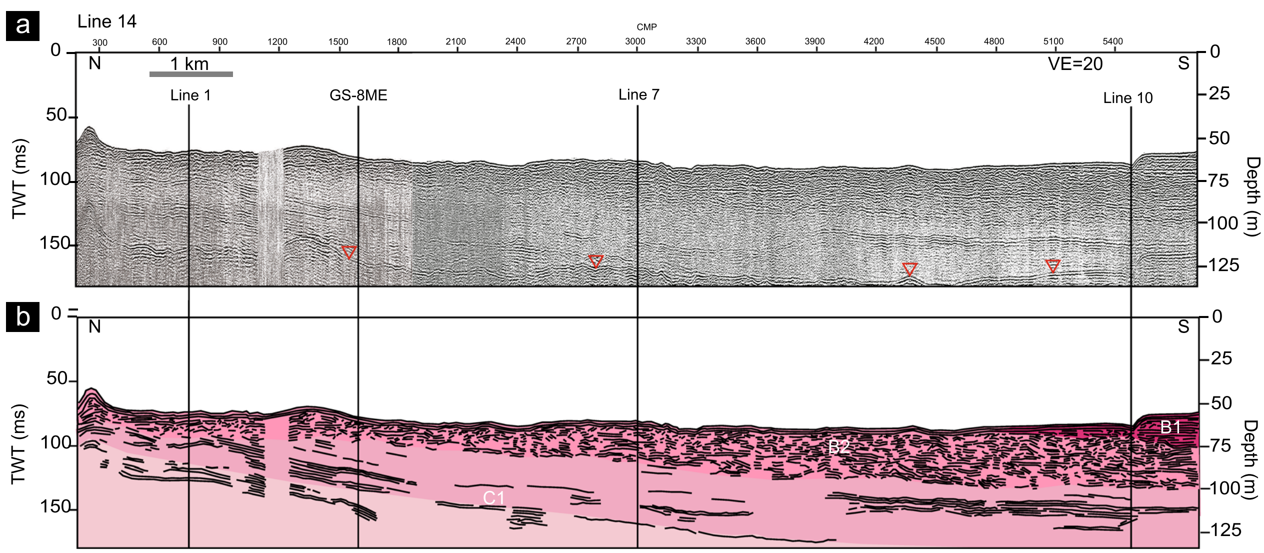

Fig. 18 Seismic profile Line 14 (Boomer). TWT: two-way travel time. Vertical line represents location of cross lines. (**a**) Uninterpreted image (post-stack, vertical exaggeration = 20). Red triangle: representative seafloor multiple. (**b**) Trace of seismic reflectors in (a) and interpreted image. The seismic units at deeper sections (light to dark pink) are assigned at the base of representative seismic reflectors traceable with other sections. Note that the strata dips and thickens southward, with an increase of tilting at greater depths, suggesting tectonic deformation

and A2 is wavy, indicating an erosional contact (Fig. 19). Here, sediments are overall thinner compared to the north, but Units A1' and A2 (13–23-m thick in total) are continuously deposited on top of Unit B1 (6–11-m thick). Unlike other sections to the north, Unit B1 is not exposed at the seafloor, and the tilting of strata is less distinct at shallow depths (Fig. 19). We interpret the tilting of strata in the deeper section beneath Unit B2 to represent the deformation by the hanging wall anticline.

4.2.4 Comparison of seismic facies with backscatter data

When combining seismic reflection and backscatter data, the seismic unit boundaries at the seafloor constrained from the seismic sections are coincident with the

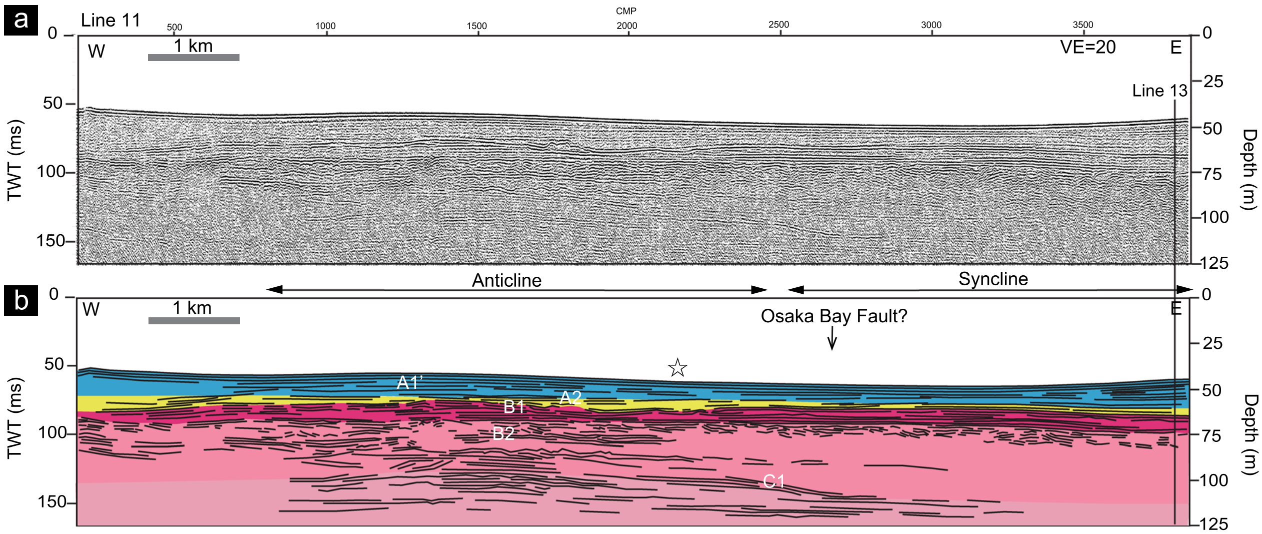

Fig. 19 Seismic profile Line 11 (Boomer). TWT: two-way travel time. Vertical line represents location of cross lines. (**a**) Uninterpreted image (post-stack, vertical exaggeration = 20). (**b**) Trace of seismic reflectors in (a) and interpreted image. Star shows location of sediment thickness measurement in Fig. 24

observed transitions in backscatter intensities (Sect. 4.1) (Fig. 4). Units A1 correspond to the heterogenous, moderate backscatter intensity facies 1, whereas Units A1' and B1 correspond to the homogeneous, weak-to-moderate backscatter intensity facies 2, and Unit B2 to the homogeneous moderate-to-high backscatter intensity facies 3 (Sect. 4.1, Fig. 4). These comparisons suggest that Units A1 and B2 consist of coarser-grained sediments such as sands and gravels, and Units A1' and B1 likely consist of finer-grained sediments such as silt and clay. The lithostratigraphy of seismic units is further discussed in Sect. 5.1.

4.2.5 Summary of observed deformation structures of the Osaka Bay Fault

Our seismic sections are all consistent with the presence of an asymmetric anticline above the Osaka Bay Fault imaged at shallow depths (50–400 m below the seafloor), characterized by a ~ 0.1 to 3.7-km-wide, steep forelimb that is dipping 0.2°–15° east and a gentler and broader backlimb that is dipping 0.2°–1.4° west, associated with an additional ~ 2.6-km-wide syncline at the western extent of the anticline (Figs. 6, 7, 8, 9, 10, 11, 12, 13, 14, 15, 16, 17, 18, 19, 20, 20, 21). Towards the eastern side of our sections, the tilted strata dips 0.2–0.8° gently west, forming a broad ~ 11-km-wide syncline in the footwall.

Our northern, central, and southern sections clearly show that the dip of the anticline forelimb is steeper in the northern area (0.4°–15°) with larger offsets across the fold, compared to that of the south (0.2°–5.2°) (Fig. 20). The southward tilting and thickening of strata observed in our N-S sections on the hanging wall to the west, also indicate larger amounts of uplift to the north (Fig. 18). The observed north–south variations in the width and geometry of the folds indicate along-strike variations in the amount of displacement of the underlying Osaka Bay Fault and its slip rate, and are further discussed in Sect. 5.2.

Our seismic data show no presence of fault plane reflections at our imaged depths, and confirm that the Osaka Bay Fault is blind. The deformation, however, reaches to and near surface by an asymmetric fold that grows progressively steeper with depth, showing clear evidence of limb rotation and fanning of limb dips (Fig. 20). The lengths of the limbs increase with depth, forming growth triangles between the anticlinal and synclinal fold axes, characterized by upward narrowing kink bands, where shear occurs within the triangular zone ("trishear") (e.g., Erslev 1991; Hardy and Ford 1997; Cardozo et al. 2011; Allmendinger 1998) (Fig. 20). The shear along the fault is not localized onto a narrow zone that is meters to tens of meters thick, but rather, shear is spread out across the entire forelimb in the trishear envelope, reaching to near the surface. An asymmetric fold commonly develops in the hanging wall of a thrust fault that is propagating towards the surface (e.g. Jamison 1987; McClay 1992; Almeida et al. 2018). We observe slip on the fold decreasing towards the surface, which is typical for a trishear fault-propagation fold that is continuously buried by sediments during its uplift history (e.g., Erslev 1991; Hardy and Ford 1997; Cardozo et al. 2011; Allmendinger 1998). At the bottom of the sedimentary basin (~ 2 km depths), previous studies image the Osaka Bay Fault offsetting the pre-growth strata of the granitic basement of the Ryoke

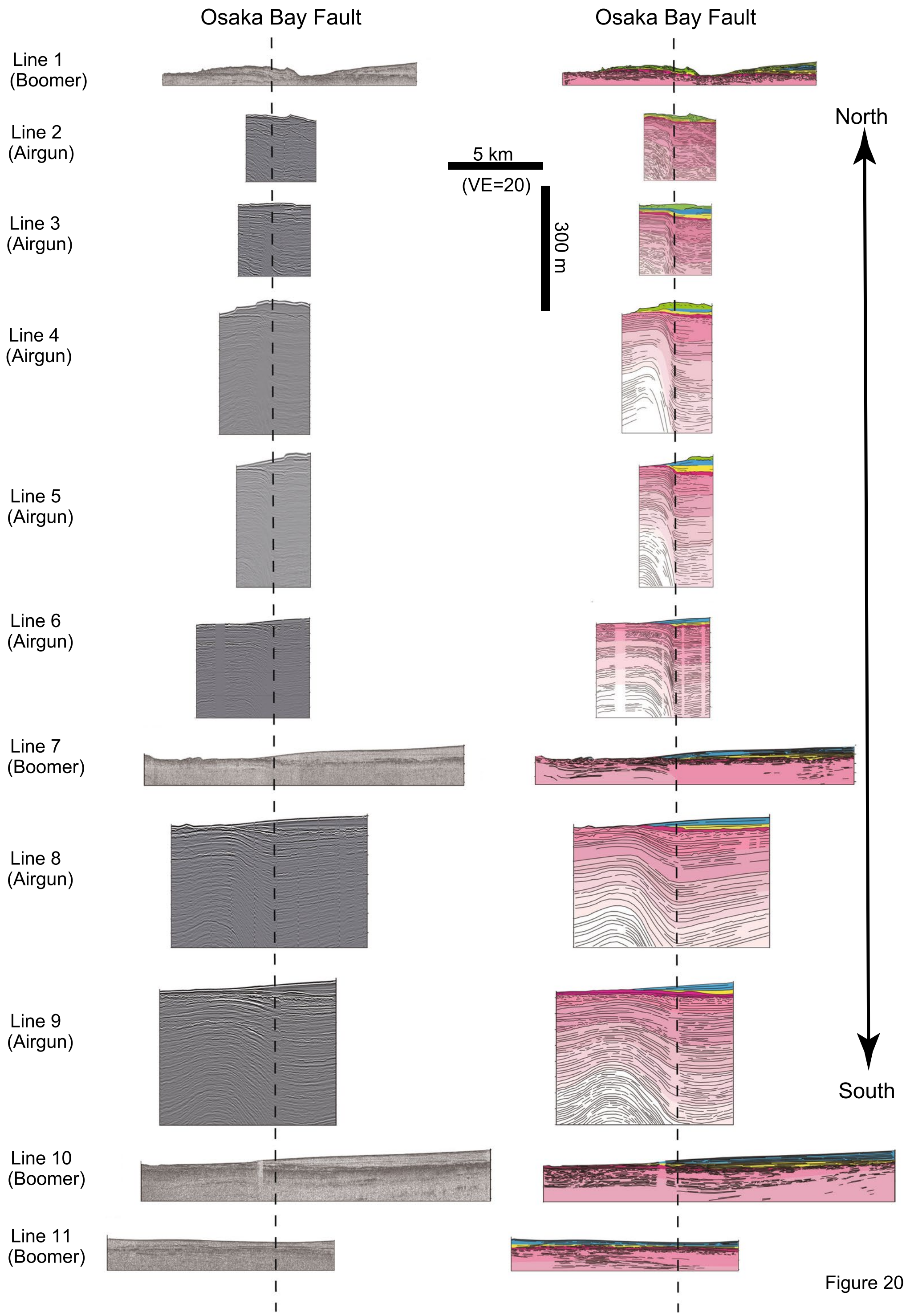

Fig. 20 Overview of E–W sections acquired in this study. Left: uninterpreted image. Right: interpreted image. Vertical exaggeration = 20. Note the northward increase in vertical displacement across the Osaka Bay Fault

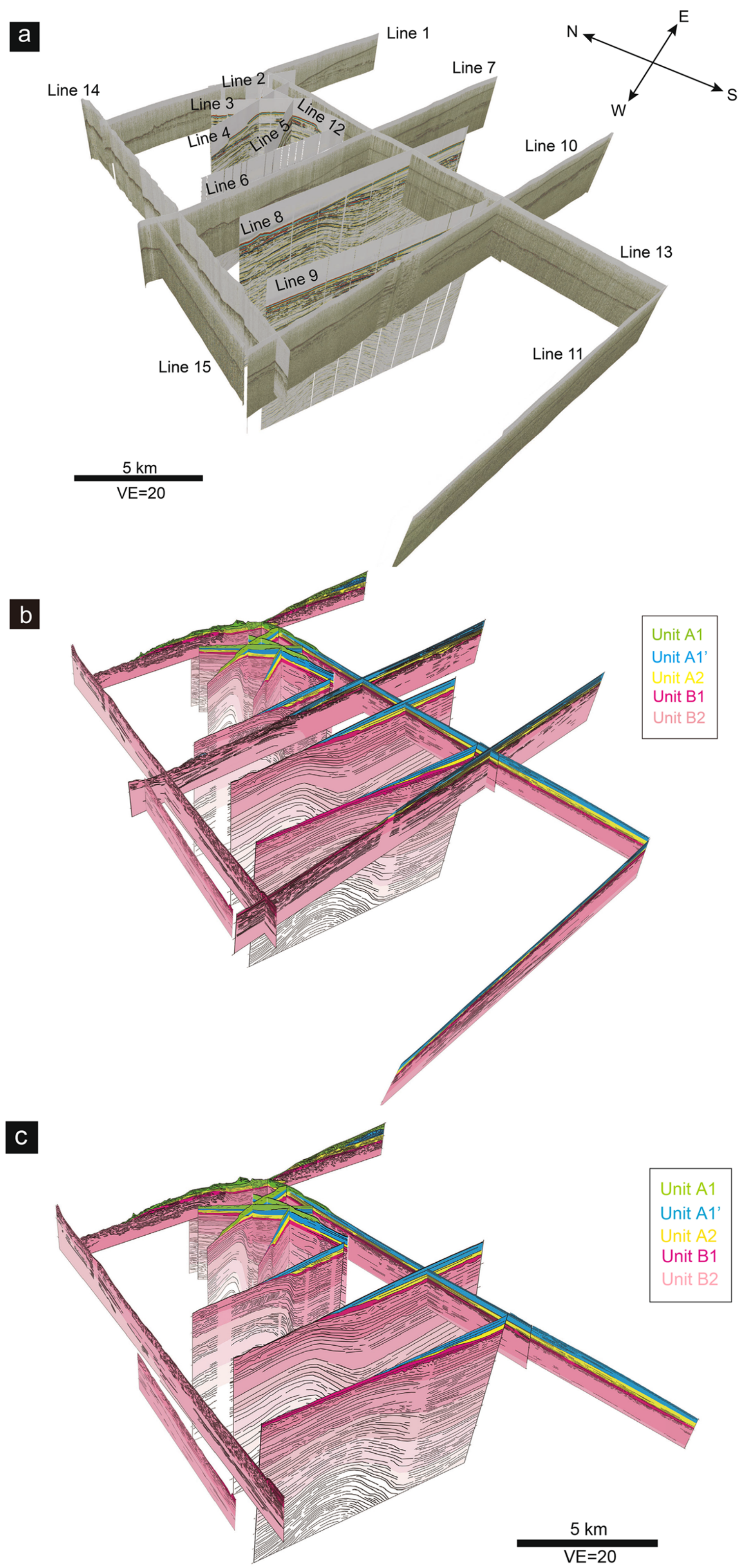

Fig. 21 Fence diagram of all seismic sections acquired in this study. Vertical exaggeration = 20. (**a**) Uninterpreted image. (**b**) Interpreted image. (**c**) Interpreted image excluding Lines 7, 10, and 11

Group (e.g., Sato et al. 1998; Yokokura et al. 1998), indicating the presence of a fault plane extending to deeper depths, with the fault tip estimated to exist at 1.5–4.5 km based on trishear modelling (Grothe et al. 2014). We interpret that the observed fold is a fault-propagation fold, and that the Osaka Bay Fault has accrued enough slip to generate this entire fold panel at its fault tip.

The seismic data from both our study and previous studies do not reveal clear stratigraphic cutoffs across the Osaka Bay Fault and measurable fault-dip angles. We measure fold axial surfaces that characterize the shear occurring within the growth triangle bounded by the anticlinal axial surface (growth axial surface) dipping ~ 12 to 25° to the west, and the synclinal axial surface dipping ~ 75 to 89° (to the west along Lines 4, 5, 6, and to the east along Lines 2, 3, 8, 9), along which shear is most concentrated throughout the stratigraphic column (Fig. 20; e.g., Hardy and Ford 1997; Cardozo et al. 2011). The more gently inclined anticlinal fold axis compared to the synclinal fold axis is consistent with the growth axial surface in the growth triangle above the blind thrust but at shallower levels (Grothe et al. 2014). It likely records the interplay between the migrating edge of the sheared trishear envelope and deposition of sediments deposited as the fold grows upward through the stratigraphic section (Grothe et al. 2014). The anticlinal fold axis is thus not necessarily a planar surface, as rates of sedimentation can vary its geometry; for example, faster sedimentation would tend to steepen the anticlinal axial surface and vice versa. It also marks the change in thickness of the growth strata in the trishear envelope, as predicted by fault related fold theory for trishear fault propagation folds (e.g., Allmendinger 1998; Grothe et al. 2014).

The synclinal axial surface marks the edge of the trishear envelope on the footwall side of the fault, but does not indicate the actual dip of the thrust per se (Grothe et al. 2014). The synclinal axial surface at shallow depths measured in this study ranges 75°–85° (84°–85° along Lines 1–3, and 75° along Lines 4 and 5) and 85°–89° in our northern (Figs. 6–10) and central (Figs. 13, 14, 15, 16, 17) survey areas, respectively, steeper than the synclinal axial surface measured in previous studies (~ 72°) at greater depths (e.g. Sato et al. 1998; Grothe et al. 2014). The steeper dips of the synclinal axial surface at shallow depths are associated with an upward propagating growth triangle with ongoing sedimentation (e.g., Hardy and Ford 1997; Cardozo et al. 2011). The presence of a backlimb on the fault-related fold of the Osaka Bay Fault may relate to the steepening of the trishear envelope (e.g., Seeber and Sorlien 2000). The fact that the backlimb steepens progressively with depth is also indicative of a curved thrust fault (e.g., Seeber and Sorlien 2000). The shallow part of the fault-structure documented by our study in previously unavailable detail, provides new insights on the geometry of subsurface deformation caused by the Osaka Bay Fault.

Our sections show that the strata thin across the folds and thicken in the footwall, indicating that these units represent syn-tectonic growth stratigraphy (i.e., deposition during deformation) (e.g., Hardy and Ford 1997; Cardozo et al. 2011; Grothe et al. 2014) (Figs. 6, 7, 8, 9, 10, 11, 12, 13, 14, 15, 16, 17, 18, 19, 20, 20, 21). The sediments in the growth strata have continuously buried the fold scarps formed by slip on the Osaka Bay Fault, recording the amount of relative uplift as the difference in stratigraphic thickness between the uplifted fold crest in the hanging wall and the subsided trough in the footwall. The ages of growth strata therefore define the timing of deformations. In Sect. 5.2, we measure the differences in stratigraphic thicknesses and combine age constraints from nearby borehole data to discuss the recent slip history of the Osaka Bay Fault.

The geometries of growth structures are controlled primarily by folding mechanism and the relative rates of sedimentation and tectonic uplift (e.g., Hardy and Ford 1997; Cardozo et al. 2011). From our seismic sections, we observe two contrasting features of growth strata; (1) progressive folding and thinning of recent strata across the fold, and (2) distinct on-lap of recent strata concentrated on the footwall above tilted strata (Figs. 6, 7, 8, 9, 10, 11, 12, 13, 14, 15, 16, 17, 18, 19, 20, 20, 21). These structural contrasts are either showing variations in rates of sedimentation and/or uplift within the bay. We investigate these processes and interpret the sequence stratigraphy in Sects. 6 and 7.

Our seismic sections and bathymetry data overall show no clear surface expression of the active fold scarps of the Osaka Bay Fault (Figs. 6, 7, 8, 9, 10, 11, 12, 13, 14, 15, 16, 17, 18, 19, 20, 20, 21). The slope of the seafloor is likely modified by various non-tectonic surface processes (erosional and depositional) such as by tidal currents. We observe along-strike variation of sediment thickness of recent sediments on the hanging wall and footwall, revealing horizons where the erosional surface of the fold is exposed at the seafloor, and horizons where the fold is buried by recent sediments (Figs. 20, 21). This trend is associated with the eastward and southward shallowing of water depth, and deeper water depths at the northwest region (Fig. 3b). The along-strike variation of sediment thickness is inconsistent with the northward increase in uplift on the hanging wall (Fig. 20, Sect. 5.2), which would predict a northward decrease in sediment thickness, clearly illustrating the imbalance between uplift and erosion.

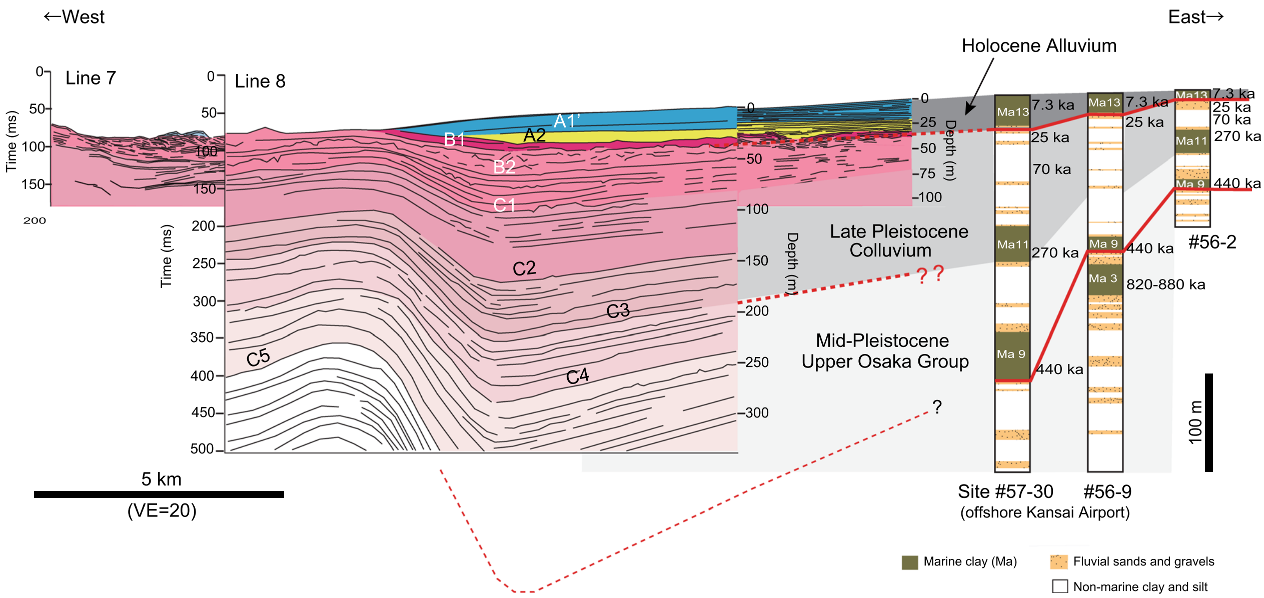

Fig. 22 Seismic Lines 7 and 8 combined with lithology previously reported at borehole sites #57-30, 56-9, and 56-2 near Kansai Airport, ~ 2.3 km east of Line 7. Boreholes are placed in their reported distance and depths. Lithology bar is modified after Nakaseko (1987). Ages (ka) are based on tephra and pollen assemblages (Nakaseko 1987). Ma: marine clay. The bases of Ma 13 and 11 correspond to the bases of the Holocene alluvium and Late Pleistocene colluvium, respectively. Units A1', A2, and B1 defined in this study are interpreted to represent the Holocene alluvium (Ma13), and Unit B2, C1, and C2 to comprise the Late Pleistocene colluvium. Note that the correlation of the base of C3 with Ma 11 is speculative, and may not necessarily coincide (Sect. 5.1.2). The red-dotted line is an extrapolation of the bedding geometry indicated from the seismic section

5 Discussion

5.1 Interpretation of stratigraphy and age

To investigate the lithostratigraphy and provide age constraints for the structures imaged by our seismic reflection data, we compare our seismic survey with published borehole data acquired from offshore Kobe city and Kansai Airport, and along the coastal plain of the Osaka Basin (Nakaseko 1987; Masuda 1992; Masuda et al. 2000; Masuda and Miyahara 2000; Nanayama et al. 2000, 2001; Kitada et al. 2001; Masuda and Itomoto 2015) (Figs. 2a, 22, 23). Although our survey lines do not directly cross over the boreholes, we are able to compare geological information and infer sequence stratigraphy (e.g., Van Wagoner et al. 1988; Catuneanu et al. 2009) with our seismic reflection and backscatter facies units and observed stratal geometries.

We start by extending our sections to the nearest boreholes (Sites 57–30, 56–23, 56–24, 56–25) offshore Kansai Airport ~ 2.3 km east of our survey Lines 7 and 8 (Figs. 2a, 22; Nakaseko 1987; Masuda 1992). Based on previous studies, the sedimentary sequence in the upper 30–35 m at these sites is primarily marine clay "Ma 13" of the Holocene alluvium (bearing the K-Ah tephra layer; ~ 7.3 ka) interpreted to be estuary and inner bay deposits, underlain by non-marine, sandy to gravely fluvial sequences of the Late Pleistocene colluvium (bearing the AT tephra layer; ~ 25 ka) (Fig. 22; Nakaseko 1987; Masuda 1992). Our E–W sections show that these sediments thicken seaward and thin towards the coast (Fig. 22). We correlate Units A1' and A2 observed from our sections with the Holocene marine clay, and Unit B2 with the fluvial sands and gravels of the Late Pleistocene colluvium (Fig. 22). We interpret Unit B1 to represent a sandy to clayey section transitioning from fluvial to marine facies across the Holocene–Late Pleistocene. Unit B1 thins to the east and is not well preserved in boreholes from offshore Kansai Airport, but is recovered and constrained by abundant microfossil ^{14}C ages and pollen assemblages from boreholes offshore Kobe (Sites OB-1 and OB-2) and coastal Osaka (Sites Suminoe-A and B) to the north (Figs. 2a, 23; Nanayama et al. 2000, 2001; Masuda et al. 2000; Kitada et al. 2001; Masuda and Miyahara 2000).

At Sites OB-1 and OB-2, ~ 6.8 km north of our survey Line 1 (Fig. 2a), the upper fluvial sequence at the base of marine clay, that we correlate with Unit B1, consists of normally-graded, interlayered silt and medium to coarse sand with pebbles, and has reported ^{14}C ages of 11.6–11.9 ka at Site OB-2 (Fig. 23; Nanayama et al. 2000). This sequence of Unit B1 is deposited up to ~ 10 m thick above the AT tephra layer (~ 25 ka), overlain by a 15–40 m thick coarser gravel sequence (Nanayama et al. 2000; Kitada et al. 2001), which we correlate to Unit B2 (Fig. 23). The AT tephra layer is also observed to cap the

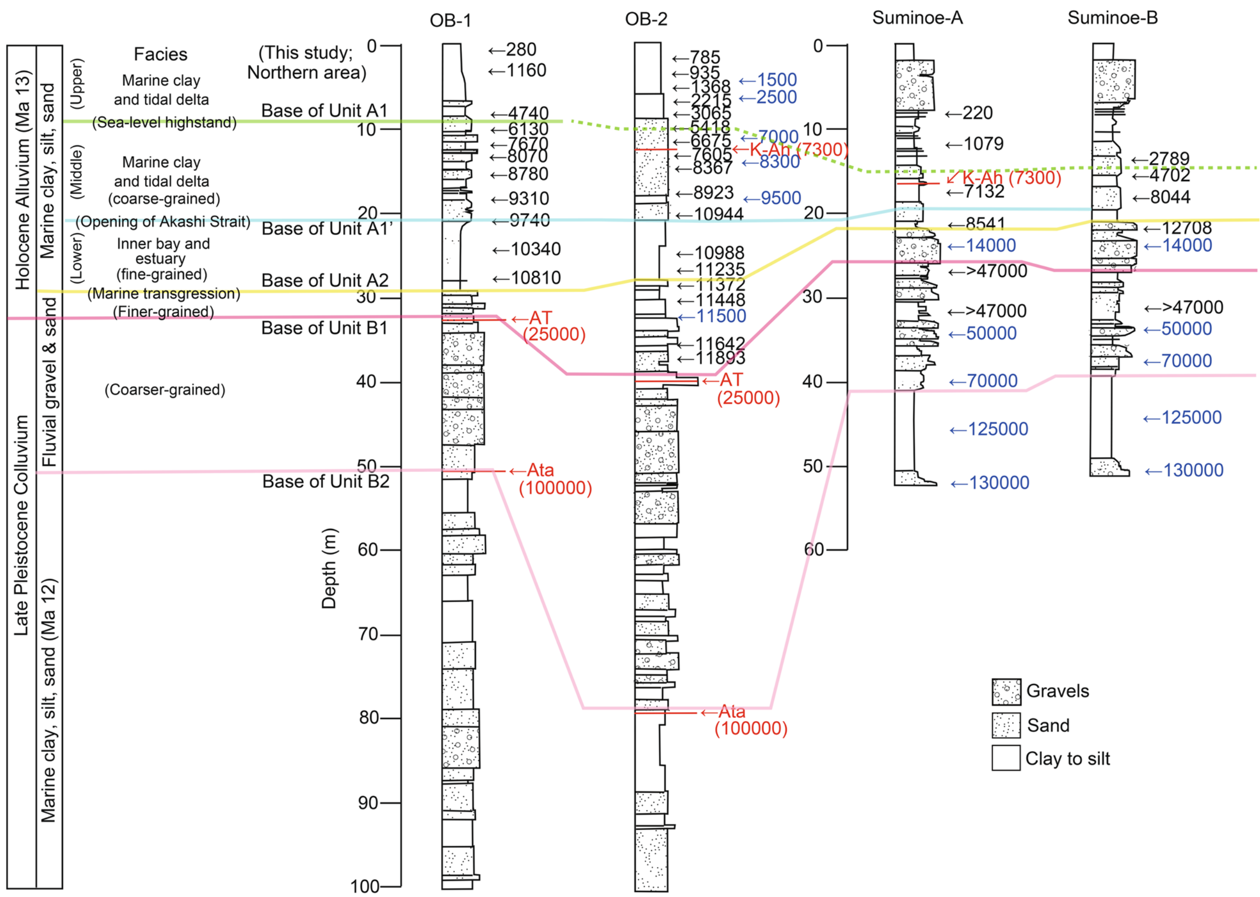

Fig. 23 Lithology bar at boreholes sites OB-1 and OB-2 (offshore Kobe) and sites Suminoe-A and B (Osaka Basin), modified after Masuda et al. (2000), Masuda and Miyahara (2000), Nanayama et al. (2000, 2001), and Kitada et al. (2001). Ages (yr) are based on these studies (red: tephra, black: radiocarbon dating, blue: pollen assemblage). The Holocene alluvium consist of a lower sequence of clay, silt, and sand interpreted to be marine clay deposited in an estuary and inner bay environment during marine transgression via the Kitan Strait, overlain by middle and upper sequences of coarser-grained, silt, sand, and clay in marine and tidal delta environment, following the opening of the Akashi Strait (~ 9.7 ka) (Masuda and Miyahara 2000; Nanayama et al. 2001). Green, blue, yellow, and pink lines mark the base of seismic units defined in this study. Bases of Units A1 and A1' in the northern area in this study are correlated with the bases of the middle and upper sequences (tidal delta facies), and the base of Unit A2 with the that of lower sequence (inner bay and estuary facies). Unit A1 comprises the contemporary Okinose sand bank, which have likely initiated during the sea-level highstand at ~ 5 ka (also see Fig. 24). Unit B1 is correlated to the finer-grained fluvial facies of the early Holocene alluvium, and Unit B2 to the coarser-grained fluvial facies of the Late Pleistocene colluvium. Note that in the central to southern area, Unit A1 is absent, and Unit A1' is deposited to the surface (~ 9.7 ka to present)

gravely sequence of Unit B2 at the boreholes offshore Kansai airport (Fig. 22; Nakaseko 1987; Masuda 1992). At Site Suminoe ~ 25 km northeast of our survey Line 1, the sandy and gravely sequence of Unit B1 (4–8 m thick) is dated 10–14 ka based on pollen assemblage at Suminoe-A, with a radiocarbon age of ~ 12.7 ka at Suminoe-B, and Unit B2 (7–12 m thick) of similar lithology is dated > 47 ka based on radiocarbon at Suminoe-A and B, separated by an unconformity at > 13 ka (Fig. 23; Nanayama et al. 2001). The youngest pollen assemblage (P2 zone, subgroup b) obtained from Unit B2 at Site Suminoe-A is 50–55 ka (Fig. 23; Nanayama et al. 2001). Here, the AT tephra layer is not well preserved, and were likely removed or disrupted by erosion at the base of Unit B1 or at the top of B2 (Fig. 23; Nanayama et al. 2001). Based on these data, we assign the age of Unit B1 to be ~ 11–14 ka, with a possibly older age (~ 25 ka or older) at the base (as inferred from the presence of AT tephra and the youngest pollen age (50–55 ka) at the top and upper section of Unit B2, respectively) (Fig. 23).

The stratal termination and onlap of Units A1' and A2 above Units B1 and B2 observed from our E–W sections are consistent with a major sequence boundary (Figs. 20, 21). The younger strata of the Holocene alluvium containing more distal facies of marine clay indicate transgression, whereas the underlying proximal facies of the coarser-grained colluvium indicate retrogradation (e.g., Van Wagoner et al. 1988; Masuda 1992; Catuneanu et al. 2009). We interpret the base of Unit B1 to represent a maximum regressive surface at the beginning of transgression (sea-level rise), when depositional trends switched from coastal progradation (regression) to retrogradation (transgression). Units B1 and B2 are interpreted to represent fluvial sediments in a lowstand systems tract across the Last Glacial Period, correlated to the incised lower terrace levels of the Tenman and the Uemachi Sub-Groups in the Osaka Basin, with Unit B1 incorporated to the early Holocene alluvium due to its relatively young age (Fig. 23; Masuda and Miyahara 2000; Nanayama et al. 2001). The boreholes indicate that the age of Unit B2 derived from AT tephra and pollen assemblage is significantly older (> 25–55 ka) than the overlying sediments, thus the base of Unit B1 is likely erosive with a possible hiatus, due to enhanced fluvial erosion during a sea level drop at MIS 2 (Fig. 23; Nanayama et al. 2001). At Sites OB-1, OB-2, Suminoe-A and B, the deepest section of the coarse gravel sequence of Unit B2 is marked by a sharp transition from finer-grained sediments (transitioning to marine clay Ma 12 at greater depth), floored by the Ata tephra (~ 100 ka) at OB-1 and OB-2, with a pollen assemblage suggesting ~ 70 ka (P3 zone, subgroup e) at Suminoe-A and B (Fig. 23; Nanayama et al. 2000, 2001; Kitada et al. 2001). The base of Unit B2 (~ 70 to 100 ka) is interpreted to represent the onset of forced regression at the beginning of sea-level drop at MIS 4 (Nanayama et al. 2001). In the current study, however, we cannot correlate the location of the base of Unit B2 from our seismic sections with the previously reported boreholes, due to the lack of traceable reflectors for the base of this horizon (Sect. 4.2).

Notably, the geometry of the boundary between Units B1 and A2 observed in our sections is wavy, suggesting fluvial erosion and/or wavy bedforms (possibly similar to the contemporary Okinose sand bank) of the sedimentary sequence (Figs. 13, 14, 15, 16, 17). We interpret this base of Unit A2 to represent an erosional surface that formed by means of waves during transgression (i.e., a transgressive ravinement surface; Catuneanu et al. 2009). The overlying sediments of Unit A2 are observed to drape and pond in the erosional spaces, rather than eroding the underlying sediments, consistent with the interpretation of a marine clay deposition in an estuary and inner bay environment (Figs. 13, 14, 15, 16, 17; Nanayama et al. 2000; Masuda and Miyahara 2000). The abrupt landward shift of marine systems (as a result of a landward shift of fluvial delta systems) suggests that the rise in sea level occurred rapidly and at rates higher than the rate of sedimentation (e.g., Catuneanu et al. 2009). Here, the marine clay of Units A1' and A2 have likely onlapped in the direction of coastal retreat/advancement of the sea, perpendicular to the shelf or parallel to the shoreline trajectory, as sediment accommodation space increased.

The ages of the Holocene alluvium are well-constrained at Sites OB-1, OB-2, and Suminoe (Figs. 23, 24; Masuda and Miyahara 2000; Nanayama et al. 2000, 2001). The Holocene alluvium recovered from Sites OB-1 and OB-2 consist of a lower sequence of clay, silt, and sand interpreted to be marine clay deposited in an estuary and inner bay environment during transgression, dated at the base to be ~ 11 ka by ^{14}C (Figs. 23, 24; Nanayama et al. 2000; Masuda et al. 2000). This lower sequence is overlain by middle and upper sequences of silt, sand, and clay, interpreted to represent tidal delta deposition driven by strong currents emerging from the Akashi Strait, in addition to marine clay deposition from floodplains of the Osaka Basin, dated by ^{14}C to be ~ 9.7 ka (radiocarbon, OB-1) at the base of the middle sequence, which is also supported by a pollen assemblage suggesting ~ 9.5 ka at OB-2, with a slightly older radiocarbon age of 10.9 ka below (Figs. 23, 24; Nanayama et al. 2000; Masuda et al. 2000). Here, the upper sequence of the Holocene alluvium is distinguished with the middle sequence by a decrease in sedimentation rate starting at ~ 8 ka, and ostracod assemblages suggestive of deepening of water in the upper section at ~ 5 to 5.3 ka, and is interpreted to represent highstand systems tract across a maximum flooding surface at ~ 5 ka, which is supported by

(See figure on next page.)

Fig. 24 **a** Depositional curves at representative sites along Lines 1–11 (location shown in Figs. 1–10, 13–17, 19) and at Site OB-1 offshore Kobe (Masuda et al. 2000), plotted with the relative sea-level curve derived from ostracod paleo-depth assemblage from a borehole at the Osaka Basin, Kitatsumori (Miyahara et al. 1999; Masuda et al. 2000; Masuda and Itomoto 2015). Elevation is measured from present sea-level. Note that the middle sequence of the Holocene alluvium (Unit A1') is distinguished with the lower sequence (Unit A2) by a decrease in sedimentation rate starting at ~ 8 ka and deepening of water at ~ 5 ka representing the sea-level highstand. The decrease in sedimentation rate is likely due to the further landward shift of marine and fluvial delta system near the sea-level highstand. During the sea-level highstand, the tidal currents have strengthened, and the Okinose sand bank (Unit A1) was likely initiated during this period (Masuda et al. 2000; Nanayama et al. 2001). Note the increase in sedimentation rate of Unit A1 compared to Unit A1' at Lines 1–5. (**b**) Comparison of stratigraphic records with Northern Hemisphere summer solar insolation (W/m^2) (red line; Berger and Loutre 1991), orbital precession cycle (amplitude/ no unit) (orange line; Berger and Loutre 1991) and Greenland ice core records (δ^{18}O /‰) (gray line; Wolff et al. 2010). MIS: marine isotope stage. YD: Younger Dryas. H1-H6: Heinrich events

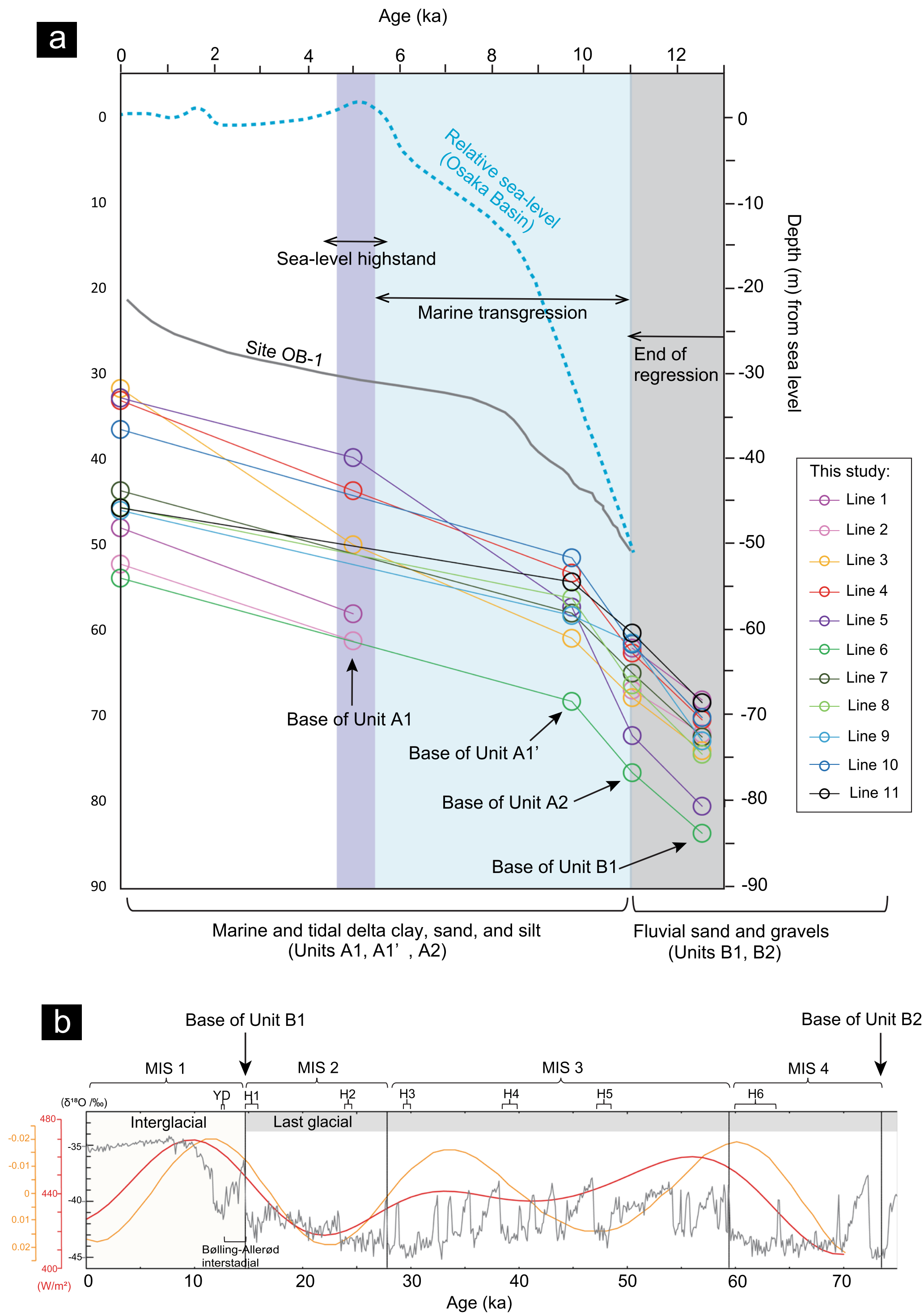

Fig. 24 (See legend on previous page.)

radiocarbon ages of 4.7–5.4 ka at the onset of tidal delta sequence identified at Sites OB-1 and OB-2 (Figs. 23, 24; Masuda and Miyahara 2000; Masuda et al. 2000; Nanayama et al. 2000, 2001). During the sea-level highstand, the tidal currents have likely strengthened, depositing coarser sediments; the Okinose sand bank was likely initiated during this period (Masuda et al. 2000; Nanayama et al. 2001). While the fluvial delta shifted further landward, decreasing the sedimentation rate of marine clay during the sea-level highstand, this period is followed by a gradual increase in sedimentation rate as the sea-level went down again (Fig. 24; Masuda et al. 2000; Nanayama et al. 2001). We correlate the lower sequence (inner bay and estuary facies) with Unit A2, and the middle sequence (marine clay and tidal delta facies) and upper sequences (marine clay and tidal delta facies; sea-level highstand) with Units A1' and A1 in our northern sections, respectively (Figs. 23, 24). The erosional surface at the base of Unit A1 observed in our section is interpreted to have formed by wave scouring and high-energy tidal currents, indicating a transgressive ravinement surface during the sea-level highstand (Lines 1, 2; Figs. 6, 7, 24). In the northern part of our survey area (Fig. 23), based on the information above, we assign the following units the following ages; base of Unit A2 ~ 11 ka, base of Unit A1' ~ 9.7 ka, and base of Unit A1 ~ 5 ka.

Our seismic sections show that Unit A1 (~ 5 ka to present) is present only in the northern area, and is replaced by Unit A1' to the surface (~ 9.7 ka to present) in the central area (Sect. 4.2.2, Figs. 13, 14, 15, 16, 17). Our sections in the central survey area show Unit A1' onlapping onto Units A2 and B1 (Figs. 13, 14, 15, 16, 17), consistent with marine transgression (retrogradation). The observed truncation of Unit A2 below Unit A1' may indicate erosion of Unit A2, suggesting that the base of Unit A1' is also an earlier transgressive ravinement surface produced by waves and tides during sea-level rise. At the shallower portion of Unit A1', we infer a possible additional downlap surface at the eastern side of our E–W sections (Figs. 14, 17), which may correlate with a switch to progradation of marine clay and further seaward shift of floodplains during recent marine regression at ~ 1 to 1.7 ka (Masuda et al. 2000). Similarly, the shallowest section of Unit A1' closer to the fault (to the west) may also be downlapping onto the underlying sediments. Although we interpret an overall onlapping relationship that is consistent with marine transgression, Unit A1' may additionally be prograding towards the east, due to the growth of the hanging wall anticline creating more sediment accommodation space eastward, forming a downlap surface onto Unit A2. The geometry of growth strata is further discussed in Sect. 5.1.1.

The Holocene alluvium in the northern regions offshore Kobe and coastal Osaka are likely to be coarser-grained compared to the clay-rich alluvium recovered offshore Kansai Airport, possibly due to the stronger effects of tidal currents around the Akashi Strait (Masuda et al. 2000; Masuda and Miyahara 2000; Nanayama et al. 2000, 2001; Kitada et al. 2001; Masuda and Itomoto 2015) (Fig. 23). We infer that Units A1' and A2 are a combination of both marine clay and tidal delta facies, but are likely to be finer-grained in our central and southern survey areas compared to the north, although these units could be seismically traced laterally across our survey area (Figs. 21, 23).

The timing of marine transgression (base of Unit A2) is dated ~ 11 to 11.4 ka from Sites OB-1 and OB-2, slightly older than the timings dated at the boreholes in coastal Osaka such as in Suminoe (~ 8.5 to 9.2 ka) (Masuda and Miyahara 2000; Nanayama et al. 2001) (Fig. 23). The timing of transgression is likely diachronous and becomes younger towards the basin margin. Similarly, sediment deposition arising from the opening of the Akashi Strait (Units A1 and A1') is also expected to be diachronous, likely becoming younger with increasing distance from the sediment source. However, we are unable to constrain the spatial variations of age and their full error range at the base of these units, as we do not have sufficient age data from offshore across the Osaka Bay. In this study, we therefore refer to the ages from OB-1 and OB-2 which are nearer to our survey lines, and use ~ 11 ka for the base of Unit A2, and ~ 9.7 ka for the base of Unit A1' in all our sections.

In summary (Table 1), we interpret Units A1, A1' and A2 to represent combined facies of marine clay and tidal delta sediments of the Holocene alluvium. Unit A1 comprises the contemporary Okinose sand bank and is coarser-grained, compared to the marine clay-rich Units A1' and A2. We correlate Unit B1 with the finer-grained fluvial facies of the early Holocene alluvium, and Units B2 to the coarser-grained fluvial facies of the Late Pleistocene colluvium. These interpretations are consistent with facies assignments based on backscatter intensity (Sect. 4.2.4), from which it can be inferred that coarser-grained facies comprise the seafloor of Units A1 and B2, whereas Units A1' and B1 comprise finer-grained facies (Fig. 4; Table 1). Internal seismic reflections also represent differences in lithology; the sequences of discontinuous and wavy reflectors that characterize Unit B2 in this study indicate the distribution of buried channels and deposition of coarser-grained, fluvial sediments forming wavy beds and scour surfaces (Figs. 6, 7, 8, 9, 10, 11, 12, 13, 14, 15, 16, 17, 18, 19). The seismically-transparent and chaotic facies of Unit A1 is consistent with coarse-grained tidal facies, whereas the thin, parallel seismic reflections of Units A1' and A2 likely represent interbeds of finer-grained marine clay (Figs. 6, 7, 8, 9, 10, 11, 12, 13, 14, 15, 16, 17, 18, 19).

Table 1 Summary of interpreted stratigraphy in this study

Survey area	Seismic unit	Characteristics of internal seismic reflections	Stratal geometries	Backscatter intensity facies	Inferred sediment facies	Intepreted sequence stratigraphic surfaces	Inferred age (ka) at the base of unit
North (Lines 1–5)	A1	Seismically transparent and occasionally chaotic reflectors	Tilting of strata by folding (Lines 1, 2, 3), onlap (Lines 4, 5), wavy and irregular contact (erosional) at the base (Lines 1, 2)	Heterogenous, moderate backscatter intensity facies 1	Marine clay, silt, sand, and tidal delta facies (Okinose sand bank)	Sea-level highstand, Maximum flooding surface (base of Unit A1), possible transgressive ravinement surface (base of Unit A1; Lines 1, 2)	~ 5 ka
	A1′	Continous, thin, parallel reflectors	Tilting of strata by folding (Lines 1, 2, 3), onlap (Lines 4, 5)	Homogeneous, weak-to-moderate backscatter intensity facies 2	Marine clay, silt, sand and tidal delta facies	Marine transgression	~ 9.7 ka
	A2	Continous, thin, parallel reflectors	Tilting of strata by folding (Lines 1, 2, 3), onlap (Lines 4, 5), wavy and irregular contact (erosional) at the base	N/A	Marine clay, silt, sand (estuary and inner bay deposits), transitioning to tidal delta facies	Marine transgression, transgressive ravinement surface (base of Unit A2)	~ 11 ka
	B1	Thick sequences of continuous, high-amplitude reflections	Tilting of strata by folding	Homogeneous, weak-to-moderate backscatter intensity facies 2	Fluvial sandy/gravely to clayey section transitioning to marine facies	Lowstand systems tract, Maximum regressive surface at the beginning of transgression (base of Unit B1), switch from coastal progradation (regression) to retrogradation (transgression)	~ 11 to 14 ka
	B2	Sequence of discontinous and wavy reflectors	Tilting of strata by folding	Homogeneous, moderate-to-high backscatter intensity facies 3	Fluvial sands and gravels	Lowstand systems tract	~ 70 to 100 ka
Central (Lines 6–10)	A1′	Continous, thin, parallel reflectors	Onlap	Homogeneous, weak-to-moderate backscatter intensity facies 2	Marine clay, silt, sand, and tidal delta facies	Marine transgression and sea-level highstand, possible transgressive ravinement surface (base of Unit A1′)	~ 9.7 ka
	A2	Continous, thin, parallel reflectors	Onlap and truncation, wavy and irregular contact (erosional) at the base	N/A	Marine clay, silt, sand (estuary and inner bay deposits), transitioning to tidal delta facies	Marine transgression, transgressive ravinement surface (base of Unit A2)	~ 11 ka
	B1	Thick sequences of continuous, high-amplitude reflections	Tilting of strata by folding	Homogeneous, weak-to-moderate backscatter intensity facies 2	Fluvial sandy/gravely to clayey section transitioning to marine facies	Lowstand systems tract, Maximum regressive surface at the beginning of transgression (base of Unit B1), switch from coastal progradation (regression) to retrogradation (transgression)	~ 11 to 14 ka

Table 1 (continued)

Survey area	Seismic unit	Characteristics of internal seismic reflections	Stratal geometries	Backscatter intensity facies	Inferred sediment facies	Intepreted sequence stratigraphic surfaces	Inferred age (ka) at the base of unit
	B2	Sequence of discontinous and wavy reflectors	Tilting of strata by folding	Homogeneous, moderate-to-high backscatter intensity facies 3	Fluvial sands and gravels	Lowstand systems tract	~70 to 100 ka
South (Line 11)	A1′	Continous, thin, parallel reflectors	Continous deposition	Homogeneous, weak-to-moderate backscatter intensity facies 2	Marine clay, silt, sand, and tidal delta facies	Marine transgression and sea-level highstand	~9.7 ka
	A2	Continous, thin, parallel reflectors	Continous deposition, wavy and irregular contact (erosional) at the base	N/A	Marine clay, silt, sand (estuary and inner bay deposits), transitioning to tidal delta facies	Marine transgression, transgressive ravinement surface (base of Unit A2)	~11 ka
	B1	Thick sequences of continuous, high-amplitude reflections	Continous deposition	Homogeneous, weak-to-moderate backscatter intensity facies 2	Fluvial sandy/gravely to clayey section transitioning to marine facies	Lowstand systems tract, Maximum regressive surface at the beginning of transgression (base of Unit B1), switch from coastal progradation (regression) to retrogradation (transgression)	~11 to 14 ka
	B2	Sequence of discontinous and wavy reflectors	Continous deposition	Homogeneous, moderate-to-high backscatter intensity facies 3	Fluvial sands and gravels	Lowstand systems tract	~70 to 100 ka

5.1.1 Variations in sedimentation rates and geometries of growth strata

Figure 24 shows the depositional curves of Units A1', A1, A2, and B1 using the assigned ages at representative locations above the footwall syncline along our northern, central and southern sections, plotted with the published depositional curve at Site OB-1 offshore Kobe (Masuda et al. 2000; Masuda and Miyahara 2000) and the relative sea-level curve of the Osaka Bay constrained from a borehole in Kitatsumori, coastal Osaka (Miyahara et al. 1999; Masuda et al. 2000; Masuda & Itomoto 2015) (Additional file 2: Table S1). Based on the inferred age and sediment thickness, we identify a sharp decrease in sedimentation rate of Unit A1' compared to Units A2 and B1 in all our sections (Fig. 24). Units A2 and B1 generally show higher sedimentation rates of 1.0–12 m/ka and 2.2–7.6 m/ka, respectively, whereas Unit A1' show lower sedimentation rates of 0.9–3.7 m/ka (Fig. 24). This is likely reflecting the decrease in sedimentation rate of marine clay due to the further landward shift of the fluvial delta during the sea-level highstand (Masuda et al. 2000; Nanayama et al. 2001) (Fig. 24).

The sediments are generally thicker in the northern region around the Okinose sand bank, characterized by higher sedimentation rates of 1.4–4.0 m/ka for Unit A1 and 2.1–3.7 m/ka for Unit A1' compared to the central and southern regions (Fig. 24). The progressive thinning of Units A1, A1', A2, and B1 across the fold observed in our northern survey areas indicate that the sediments were deposited while deformation was occurring (Figs. 6, 7, 8). This was likely achieved by the high sedimentation rate of coarser deposits that possibly exceeded the uplift rate, preserving the overall growth stratigraphy from surface erosion beneath the Okinose sand bank (Figs. 6, 7, 8).

The high sedimentation rate around the Okinose sand bank is also inferred from the high-amplitude negative polarity reflector that is partially distributed at the base of Unit A1. The high-amplitude negative polarity reflector may imply a localized horizon of abnormally high sediment porosity, suggesting that compaction and dewatering may not have kept pace with high rates of sedimentation. Rapid rates of sedimentation may produce elevated fluid pressure, possibly inducing submarine land-sliding at the base of the sand dune complex (e.g., Terrinha et al. 2019; Zhang and Askarinejad 2019). The steep flanks and multiple escarpments of the Okinose sand bank observed from our bathymetry data also imply that past gravitational collapse and syn-sedimentary normal faulting may have shaped the current morphology (Sect. 4.1, Figs. 3, 4, 5). The distribution of the negative polarity reflector along Lines 3, 5, and 12 is located across one of the steep flanks of the sand bank (Figs. 3, 8, 10, 11), and therefore may be related to past landslides that formed this topography. It is notable that this negative polarity reflector is only partially distributed and rather localized, which may indicate that this horizon could itself be a past landslide deposit. While we do not have direct evidence suggesting the occurrence of landslides (e.g., collapsed materials around the escarpments), multiple escarpments can be also be formed by other processes such as tidal erosion, rapid deposition of sand, and oversteepening of slope by sediment deposition at dune crest (e.g., Inouchi 1990; Yashima 1992; Ikehara and Kinoshita 1994).

In our central survey area, we observe distinct on-lap of Unit A1' onto Units A2 and B1, with no tilting of strata within Unit A1' (Figs. 13, 14, 15, 16, 17). This is likely due to the relatively low sedimentation rate of Unit A1' (~ 1.1 to 1.5 m/ka), possibly slower than or nearly equal to the uplift rate, suggesting that the marine clays were not continuously deposited during deformation (Fig. 24). The onlap may in fact be a result of several independent factors: marine transgression across the shelf, low sedimentation rate, and decrease in tectonic uplift to the south. The stratal dips of Unit A1' are sub-parallel to the current dip of the seafloor, thinning towards the west above the hanging wall (Figs. 13, 14, 15, 16, 17). The erosional contact between Units A1 and A2 suggest a major shift in depositional styles with possible age gaps. We therefore cannot use the upper section of Unit A1 as continuous record of growth strata to infer tectonic rates (Figs. 13, 14, 15, 16, 17). The underlying Units A2 and B1, however, show tilting of strata, preserving growth stratigraphy due to its higher sedimentation rate compared to Unit A1.

5.1.2 Implications for stratigraphy at deeper sections (Horizons C1–C5)

Past cycles of sequence stratigraphy are continuously recorded in the Pleistocene sediments in the Osaka Bay (e.g., Muslim et al. 2002; Inoue et al. 2003) (Fig. 22, Additional file 1: Fig. S5), providing a reference for inferring stratigraphy at greater depths. Marine clay layers that correlate with global eustatic sea-level highstands possess distinctive physical property contrasts with the surrounding non-marine strata that create high-amplitude reflections, and have been used as prominent stratigraphic markers by previous studies (Muslim et al. 2002; Inoue et al. 2003; Grothe et al. 2014). Notable of the marine clays are Ma 12 (~ 127 ka), Ma 11 (~ 242 ka), Ma 10 (~ 334 ka), Ma 9 (~ 427 ka), Ma 6 (~ 621 ka), Ma 3 (~ 865 ka), Ma 1 (~ 1070 ka), Ma 0 (~ 1120 ka), and Ma -1 (~ 1200 ka), that correlate with isotope stages MIS 5, 7, 9, 15, 21, 25, and 27, respectively (Additional file 1: Fig. S5). Ma 11 marks the base of the Late Pleistocene colluvium and the top of the Upper Osaka Group, whereas the bases of Ma 3 and Ma -1 mark the top and bottom of the Middle Osaka Group, respectively (e.g. Itoh et al. 2000, 2001). In Additional file 1: Figures S6–S20, we compare the bases of Horizons C1–C5 in our seismic profiles with the age-correlated reflectors of marine clays reported by Grothe et al. (2014) near the intersection points with our survey lines, along previously acquired deep seismic Lines GS-8ME (Yokokura et al. 1998), OD-B (Iwasaki et al. 1994), and HD-3 (Iwabuchi et al. 2000), correlated with the 1700-m deep borehole (Site GS-K1) at Higashinada, Kobe city (e.g., Itoh et al. 2001; Muslim et al. 2002; Inoue et al. 2003). Here, we refer to the published depth-converted profiles by Grothe et al. (2014), in which the two-way travel time section to depth conversion was made based on published stacking velocity functions by Yokokura et al. (1998). Due to the various uncertainties in correlation of seismic reflectors arising from velocity-model-dependent depth-conversions between this study and previous studies, however, we are unable to constrain reliable ages for the bases of Horizons C1–C5 in the current study Additional file 3: Table S2).

5.2 Estimation of fault displacement and slip rate of the Osaka Bay Fault: Implications for seismic hazards

5.2.1 Late Pleistocene–Holocene slip rate of the Osaka Bay fault

To document the strain accommodated by the Osaka Bay Fault, we measure the vertical offsets across the forelimb (i.e. the amount of relative uplift between the uplifted fold crest in the hanging wall and the subsided footwall trough) for the following stratigraphic horizons

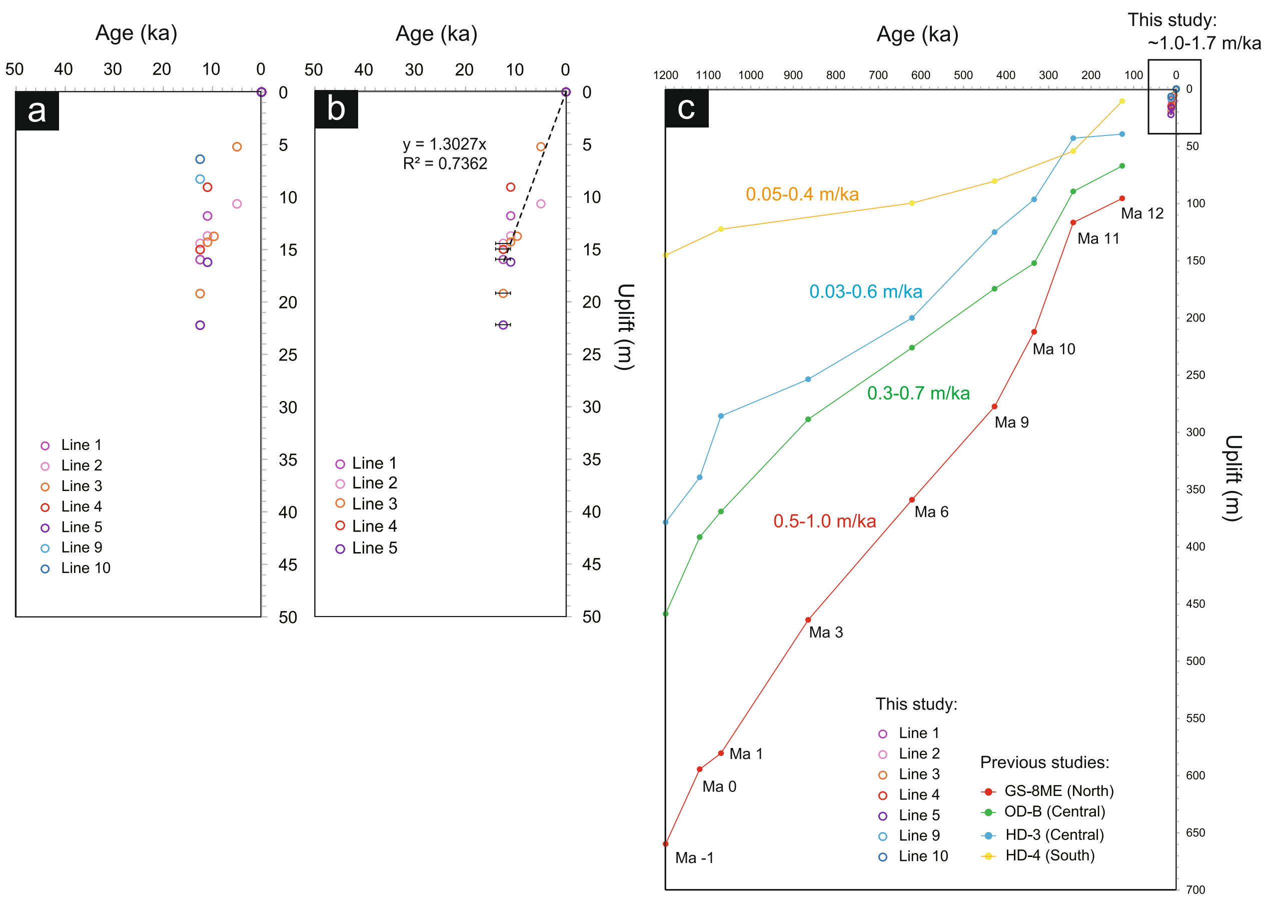

Fig. 25 Vertical uplift measured in this study plotted with inferred age and error bars. Vertical offsets across the forelimb (i.e. the amount of relative uplift between the uplifted fold crest in the hanging wall and the subsided footwall trough) were measured at the base of Units A1, A1', A2, and B1. The range of uplift rates estimated along each seismic line incorporating the full error of the ages (based on the minimum and maximum ages of each horizon) are shown in Additional file 1: Figs. S30–S33. (**a**) Uplift versus age measured from Lines 1–5, 9, and 10 in this study. (**b**) Uplift versus age measured from the northern sections Lines 1–5. The slope of the linear regression represents the estimated uplift rate using average ages. (**c**)Vertical uplift measured in this study and from previous deep seismic lines plotted with average age of marine clays and bases of Units A1, A1', A2, and B1. Uplift rate is estimated from the range of the slope of linear regression. Note the northward increase in uplift rate. Box on upper right shows data plotted from this study closed-up in **a**

(Sect. 5.1); the bases of Units A1 (~ 5 ka), A1' (~ 9.7 ka), A2 (~ 11 ka), and B1 (12.5 ± 1.5 ka), and the bases of Horizons C1, C2, C3, C4, and C5 (Additional file 1: Figs. S21–S29, Additional file 4: Table S3). For comparison, we also measure the vertical offsets of the marine clays Ma 12, Ma 11, Ma 10, and Ma 9 using the depth-converted images along the deep seismic Lines GS-8ME (Yokokura et al. 1998), OD-B (Iwasaki et al. 1994), and HD-3 (Iwabuchi et al. 2000) from previous studies (Grothe et al. 2014) (Additional file 1: Figs. S6–S19; Additional file 4: Table S3). For this analysis, we picked the highest position on the hanging wall fold crest and the most subsided position on the footwall syncline, and avoided undulating surfaces that are not planar (Additional file 1: Figs. S21–S29). We then plot the measured vertical offsets with known age to obtain uplift rates from the slope of the linear regression (Figs. 25, Additional file 1: Figs. S30–S33). To incorporate the full error of the ages, we estimate the range of uplift rates based on the minimum and maximum ages of each horizon (Additional file 1: Figs. S30–S33).

The most recent time period defined in this study is from the bases of Units A1 (~ 5 ka) and A1' (~ 9.7 ka) to the present. The total vertical uplift over the last ~ 5 ka ranges ~ 5 to 11 m, and ~ 6 to 14 m over the last ~ 9.7 ka in our northern survey area (Fig. 25a, b; Additional file 1: Figs. S30–S33). At the base of Unit A2, the vertical uplift ranges ~ 8 to 14 m and > 2–9 m over the last ~ 11 ka at the northern and central regions, respectively, and adds up to a total of ~ 9 to 19 m (northern) and > 6 m (central) over the last ~ 11–14 ka at the base of Unit B1 (Fig. 25a, b; Additional file 1: Figs. S30–S33). Units A2 and B1 at the central survey area are partly eroded at the seafloor, giving a minimum value for uplift (Figs. 13, 14, 15, 16, 17, 25a; Additional file 1: Figs. S31–S33). From the linear regression of the measured vertical offsets and age, the Late Pleistocene–Holocene uplift rate is estimated to range ~ 1.0 to 1.7 m/ka (Additional file 1: Figs. S31–S33) (average ~ 1.2 to 1.4 m/ka; Fig. 25b, Additional file 1: Fig. S30) and > 0.6 m/ka at the northern and central regions, respectively (Additional file 1: Figs. S31–S33). When using fault dip of ~ 70° estimated from greater depths by previous studies (Grothe et al. 2014), the uplift rates correspond to fault slip rates of ~ 1.1–1.8 m/ka and > 0.6 m/ka.

From previous studies along deep seismic Lines GS-8ME (Yokokura et al. 1998), OD-B (Iwasaki et al. 1994), and HD-3 and HD-4 (Iwabuchi et al. 2000), average uplift and fault slip rates of ~ 0.5 m/ka (with a range of ~ 0.5 to 1.0 m/ka), ~ 0.3 m/ka (with a range of ~ 0.2 to 0.7 m/ka), ~ 0.3 m/ka (with a range of ~ 0.03 to 0.7 m/ka), and ~ 0.1 m/ka (with a range of ~ 0.05 to 0.4 m/ka), are inferred in the northern, central, south-central, and southern regions along the Osaka Bay Fault, respectively, based on measured displacements at the bases of marine clay bed markers (Ma 12 to Ma − 1) during the Middle Pleistocene (< ~ 1.2 Ma), using the velocity functions by Yokokura et al. (1998) (Grothe et al. 2014) (Fig. 25c; Additional file 4: Table S3). This is generally consistent with the Pleistocene uplift rates estimated by previous studies; Yokokura et al. (1998) reported vertical uplift rate of 0.5–0.6 m/ka along the Osaka Bay Fault during the early–late Pleistocene, whereas Iwabuchi et al. (2000) reported vertical uplift rate of 0.5 m/ka over the last 200 ka, 0.6 m/ka over the last 600 ka, and 0.6–0.7 ka over the last 1200 ka.

It is noted that the measured depths and amount of uplift from the seismic profiles are velocity-model dependent. The depth conversion of the seismic profiles acquired in this study uses constant velocity at 1500 m/s (Section 4.2). If we use the downward increasing velocity functions by Yokokura et al. (1998) which predict that the velocity increase from ~ 1500 m/s up to ~ 1700 m/s at ~ 500 ms along Line GS-8ME close to the fault and close to our survey line, the total depths (up to ~ 500 ms) along our seismic profiles would deviate up to 7% increase at the trough of the footwall syncline, and up to 4% increase at the crest of the hanging wall anticline. If using this velocity function at the hanging wall and footwall (Yokokura et al. 1998), we estimate the deviation of uplift from that measured using constant velocity (1500 m/s) in the northern survey area at the bases of Units A1–C1 to be 0%, and ~ 1.3% increase at the base of Unit C2, indicating that the consequent errors for Late Pleistocene–Holocene uplift rates documented from Units A1–B1 in this study are minimal. In comparison, we also estimate the deviation of uplift in the central survey area to be ~1.6% increase at base of Unit C1, ~ 2.3% increase at the base of Unit C2, and ~1% increase at the base of Unit C3. As a result, the estimated uncertainties of measured uplift from our seismic profiles would range + 0.2–0.8 m at the base of Unit C1, + 0.9 to 1.3 m at the base of Unit C2, and + 0.8–1.1 m at the base of Unit C3.

The uplift rates estimated across the Late Pleistocene–Holocene in this study (~ 1.0 to 1.7 m/ka) (Fig. 25b; Additional file 1: Figs. S30–33) is larger than estimated across the Pleistocene (~ 0.5 to 0.7 m/ka; Yokokura et al. 1998; Iwabuchi et al. 2000), suggesting that the slip rate on the Osaka Bay Fault may have increased since the Late Pleistocene. We note, however, that the Pleistocene uplift rates are averaged over longer time periods than our Holocene uplift rates measured in higher resolution, and the assumption of an uplift rate remaining constant between the time intervals of marine clays (~ 100 ky) in the Pleistocene may not be applicable. The fault slips along the Osaka Bay Fault have likely been variable in space and time within the ranges stated above (Fig. 25c).

For a given fault slip, a steeper fault dip will produce larger vertical uplift. We infer steeper synclinal fold axis (~75 to 90°) in the recent strata from the dips of the eastern synclinal fold axis, compared to that measured from greater depths by previous studies (~72°) (Sect. 4.2). The presence of a backlimb also implies that the fault steepens upward (Seeber and Sorlien 2000). However, the overall range of these steep dips (~70° or near vertical) do not contribute largely to the increase in fault slip, showing that the slip rates may have likely increased in recent strata.

Larger fault slip rates may imply a higher probability of frequent earthquake recurrences, although fault slip can be accommodated by both coseismic, interseismic, and aseismic events (e.g., Scholz 2019). The lack of localized microseismicity and aseismic creep along the Osaka Bay Fault (e.g., Katao et al. 1997; Nakamukae et al. 2003; Matsushita and Imanishi 2015; Nishimura et al. 2020), however, indicate that fault slip is largely accommodated by large earthquakes and long-term inelastic deformation such as folding. Coseismic events, especially large magnitude earthquakes, produce large and rapid fault slips compared to aseismic deformation. During the 1995 M_w6.8 earthquake, for example, vertical offsets of up to ~1.2 m was inferred along the Nojima Fault (Awata et al. 1995; Nakata and Yomogida 1995; Nakata et al. 1996). The total vertical uplift of ~5–11 m over the last ~5 ka observed along the Osaka Bay Fault may therefore indicate the occurrence of multiple earthquake events.

Previous shallow seismic surveys using a single-channel sonoprobe conducted by Nanayama et al. (2000) along the northern extent of the Osaka Bay Fault, ~9 km north of our survey Line 1, reported vertical uplifts of ~5.5 to 8 m during the last ~7.3 to 8.6 ka, and ~2 to 3.5 m during the last ~0.9 to 1.2 ka, which is the most recent time period of fault activity that has been so far documented along the Osaka Bay Fault. Their results are comparable with our uplift estimates of ~5 to 11 m over the last ~5 ka, and ~6 to 14 m over the last ~9.7 ka in our northern survey area (Fig. 25a).

Although there is no direct paleoseismological record reported at the Osaka Bay Fault, previous on-land trench excavation studies at other faults have reported ruptures during the 1596 A.D. Keicho-Fushimi Earthquake (~M7.5), prior to the 1995 Kobe Earthquake, along multiple fault strands of the surrounding Arima-Takatsuki and Rokko-Awaji Island Fault zones (e.g., Nojima and Gosukebashi Faults), in addition to the Median Tectonic Line in Shikoku (Nakata et al. 1996; Lin et al. 1998; Sangawa 2001; Ikeda et al. 2019). According to trench studies at the Nojima Fault, the 1596 and 1995 events were preceded by events that occurred at ~2 and ~4 ka (Awata et al. 1996; Nakata et al.1996). At several trenches along the Arima-Takatsuki Fault zone, rupturing events that occurred at ~2.8 to 3 ka were also identified as predating the 1596 event (Sangawa 2001). Studies of the Gosukebashi Fault, for example, report that the 1596 event was predated by an event at ~416 A.D. (Yamato Earthquake), and an event occurring between ~6 ka and 1596 AD (Maruyama et al. 1997; Lin et al. 1998). Although the recurrence intervals of earthquakes along individual faults are likely variable, the 1995 and 1596 events have demonstrated that multiple fault segments in this region can potentially slip in a single or multiple events at around the same time period, leading to disastrous, large-magnitude earthquakes (Hirata et al. 1996; Kato et al. 2008; Ikeda et al. 2019). The Osaka Bay Fault may have ruptured in the form of fold scarps during these events (1596 AD, 416 AD, ~2 ka, ~4 ka), together with the surrounding faults in this region, producing the total vertical uplift of ~5–11 m over the last ~5 ka, as inferred from our study (Fig. 25a,b). It is important to note that, although blind, the fault displacement along the Osaka Bay Fault can potentially extend to the surface during earthquakes, as demonstrated from the shallow deformation across its entire forelimb (Sect. 4.2.5).

The possible increase in fault slip rates inferred in this study emphasize the importance of documenting recent deformation of strata and averaging slip rates over shorter time periods for probabilistic seismic hazard assessments. Our results suggest that slip rates and sedimentation rates averaged over longer time intervals may yield lower estimates of earthquake recurrence. Variable fault slips in space and time along the Osaka Bay Fault have also been documented by Grothe et al. (2014), inferring steadier fault slip rates at longer timescales of ~100 s of ky, which have also been noted for faults in other tectonic regions (e.g., Mouslopoulou et al. 2009; Bergen et al. 2017; Mueller 2017).

5.2.2 Northward increase in slip on the Osaka Bay Fault and implications for slip rates

Our study and previous seismic reflection studies document a northward increase in vertical uplift and slip rates along the Osaka Bay Fault (Figs. 20, 25; Additional file 1: Figs. S30–S33), indicating higher fault activity and/or structural maturity in the north (Yokokura et al. 1998; Iwabuchi et al. 2000; Grothe et al. 2014). This is supported by our observation that the dip of the anticline forelimb is steeper in the northern area (~0.4 to 15°) with larger offsets across the fold, compared to the dip of the forelimb in the central regions (~0.2 to 5.2°), indicating southward decrease of fault-related folding (Sect. 4.2). The southward tilting and thickening of strata observed in the hanging wall are also consistent with northward increase in uplift (Fig. 18). Despite the larger offsets and steeper forelimbs in the northern region, however, the dip of the eastern synclinal axial surface and inferred fault dip are steeper in the central regions (~ 85 to 89°) compared to the north (~ 75 to 85°) (Sect. 4.2), suggesting that the total fault slip indeed increases northward.

Grothe et al. (2014) inverted fault tip depths from the tips of the triangular zones inferred from the geometry of folded growth strata of the Osaka Bay Fault based on 2D asymmetric trishear modeling. Their models suggest greater initiating depths of the fault tip in the north (~ 3.5 to 5 km) and shallower depths in the south (~ 1.6 to 2.5 km) (Grothe et al. 2014). The fault tips initiate from older strata (~ 1.5 Ma) in the north than in the south, implying that the fault may have propagated laterally from north to south with time (Grothe et al. 2014). The greater depths of fault tips in the north may have been influenced by the depth of the basement and thickness of overall sediments that increase from south to north, as inferred by isopach models and gravity anomalies shown by previous studies (Komazawa et al. 1996; Yokokura et al. 1998; Iwabuchi et al. 2000). Sediment thickness in the basin is likely related to the effect of flexural loading by surrounding faults, although other far-field processes occurring deeper in the lithosphere may also play a role. The greater thickness of the depocenter at depths in the northern region is likely recording subsidence on the footwall of the Kariya Fault offshore northern Awaji Island, counteracted by uplift on the hanging wall of the Osaka Bay Fault (Fig. 2a). The southward tilting and thickening of recent strata observed in this study (Fig. 18), however, is contrary to the northward thickening at greater depths (> ~ 1000 m depths; > 1.2 Ma) (Iwabuchi et al. 2000), and suggests increased effects of uplift on the Osaka Bay Fault compared to the Kariya Fault in relatively recent strata (< 1.2 Ma).

Lateral propagation and growth of the fault may indicate that the fault lengths and areas of the Osaka Bay Fault have increased with time (Grothe et al. 2014). Generally, for a newly-initiating fault, an increase in fault length would correspond to greater displacement, leading to estimations for larger maximum potential earthquake magnitudes and seismic hazards (e.g., Bergen and Shaw 2010). Accelerated Holocene slip rates along active faults have also been reported for blind thrust fault systems in other regions such as beneath the Los Angeles basin (Bergen et al. 2017; Mueller 2017). The possible increase in slip rates during the Late Pleistocene–Holocene inferred in this study may be a result of enhanced lateral fault propagation since the Late Pleistocene, that led to an increase in average displacement per earthquake and occurrence of larger earthquakes.

The trishear modelling by Grothe et al. (2014), however, suggested that the Osaka Bay Fault is reactivated, based on the shallow depth of the fault tip early in its history, instead of a fault that initiated from the base of the seismogenic crust (e.g. Figure 1c). A reactivated fault may not necessarily involve lateral fault propagation in its recent history. Furthermore, changes in fault slip rate and propagation may not necessarily be directly correlated; fault propagation may depend on the strength of rock and faults (Hardy and Allmendinger 2011), whereas fault slip rates may depend on stressing rates and interaction among other neighboring faults.

Alternatively, the increase in slip rates may occur as a consequence of an overall increase in frequency of small-to-large earthquakes along the Osaka Bay Fault, which may not necessarily relate with increase in fault lengths. Other external forcing not related to tectonics may also affect fault activity (Mueller 2017), such as by unloading or loading by sea-level fluctuations and erosion (e.g., Calais et al. 2010; Luttrell and Sandwell 2010; Steer et al. 2014), or shorter timescale stress transients caused by earthquakes in the vicinity (e.g., Freed 2005; Ishitsuka et al. 2020). In the current study, we cannot rule out the cause of the inferred transient slip, although short-term forcing is less likely based on the time duration (> ~ 10 ka to present) of the inferred increase in slip rates in this study (Fig. 25).

5.2.3 Comparison of slip rates with regional faults

The Osaka Bay Fault is surrounded by the NE–SW trending Rokko-Awaji Island Fault zone (e.g. Nojima, Kariya, Kusumoto, and Higashiura Faults) to the west and north, the Uemachi Fault zone to the east, and the E–W trending Median Tectonic Line to the south (Fig. 2a). The average slip rate along the Nojima Fault that ruptured during the 1995 earthquake is 0.4–0.5 m/ka vertically and 0.9–1.0 m/ka right-laterally (Mizuno et al. 1990). The right-lateral average slip rate of the Kusumoto Fault is estimated to range 0.5–1.0 m/ka (Mizuno et al. 1990). The average slip rates of the E–W faults that extend to the Rokko Mountains are inferred to have larger lateral slip component, ranging ~ 2.0 m/ka right-laterally and 0.3–0.4 m/ka vertically (e.g. Itoh et al. 2000). For the Arima-Takatsuki Fault zone to the north, 0.06–0.2 m/ka vertical and 0.5–1.5 m/ka right-lateral slip rates have been reported (Sangawa 1978). The Uemachi and Ikoma Fault zones to the east have reported average vertical slip rates of ~ 0.4 m/ka and 0.5–1.0 m/ka, respectively (Research and Development Bureau/MEXT & DPRI 2013; The Headquarters for Earthquake Research Promotion/Earthquake Research Committee 2001). The overall similar slip rates in the region may suggest that the faults behave as a linked system. We note however that our slip rates are larger than most of the uplift rates reported by previous studies. By contrast, the long-term uplift rate estimated from the height of the mountain ranges; 2–3 km of vertical offset between the Osaka Basin and the Rokko Mountains (and Awaji Island) during the last 3 million years (e.g. Sato et al. 1998), yield a long-term uplift rate of 0.7–1.0 m/ka. This value is approximately the average between the Middle–Late Pleistocene slip rates inferred from previous studies (0.5–0.7 m/ky; see Yokokura et al. 1998; Iwabuchi et al. 2000) and the Late Pleistocene–Holocene slip rates (1.0–1.7 m/ka) inferred in this study (Fig. 25b; Additional file 1: Figs. S30–S33) at the Osaka Bay Fault, supporting that these rates are plausible.

The northern Osaka Bay Fault is known to splay into three strands (Wadamisaki, Rokko Island, and Maya Faults), and the average uplift rate of the Wadamisaki Fault is reported to range ~ 0.2–0.3 m/ka (Yokokura et al. 1998). The observed northward increase in slip along the Osaka Bay Fault may be translating to these splays. Nanayama et al. (2000) reported large Holocene uplift of ~ 6 m during the last ~ 6–7.3 ka on the Wadamisaki Fault, although they did not find that significant uplift occurred during the Holocene along the Rokko Island and Maya Faults.

By contrast, the average slip rates along the Median Tectonic Line to the south range ~ 0.8–1.0 m/ka vertically beneath the Kitan Strait (Nanayama 1999), with right-lateral slip rates of ~ 1.8–3.5 m/ka and ~ 6 m/ka onland to the east and west of the strait, respectively (Okada 1970; Okada and Sangawa 1978; Saito et al. 1997; Okada and Tsutsumi 1997). Near the Kitan Strait, E–W trending fault strands that may possibly be the seaward extension of the Uemachi Fault zone have been reported beneath the southern Osaka Bay, revealing vertical uplifts (Yokokura et al. 1998). These fault strands run parallel to the Median Tectonic Line, indicating a structural link with the faults beneath the Osaka Bay and the Median Tectonic Line. We do not have sufficient data for the southern region to fully address the structural link between the N-S trending Osaka Bay Fault with the E–W trending fault zones of the Median Tectonic Line and the Uemachi Fault zone. Structural complexities in the southern Osaka Bay are inferred from changes in the overall fault geometry and partitioning of multiple fault strands (Yokokura et al. 1998; Iwabuchi et al. 2000) and variable basement morphologies that are overall uplifted towards the Kitan Strait above the Cretaceous Izumi Group (Komazawa et al. 1996; Afnimar et al. 2002; Itoh et al. 2013a) (Fig. 2a, Sect. 2.2).

The southward decrease in slip of the Osaka Bay Fault along-strike observed in this study, and the lateral southward fault tip migration suggested by Grothe et al. (2014) may indicate that the southern segment of the Osaka Bay Fault has accommodated less slip after its reactivation compared to the northern segment. The recent increase in slip to the north may be related to its prior slip history; for example, the northern fault may be weaker in strength compared to the south, due to more slip accumulating in prior periods. Additionally, the northern segment of the Osaka Bay Fault may be more active than the south due to the interactions with other larger fault systems such as the Rokko-Awaji Island and Arima-Takatsuki Fault zones to the north. In the southern Osaka Bay, slip may be partitioning into other fault strands to the west (Iwabuchi et al. 2000), which may also relate to the southward decrease in slip of the Osaka Bay Fault. Alternatively, a change in stress state within the bay (Katao et al. 1997; Nakamukae et al. 2003; Matsushita and Imanishi 2015) may also contribute to the change in vertical component of slip.

If it is assumed that the total amount of slip adding all the faults in the system has been constant with time, the inferred increase in slip rate on the Osaka Bay Fault may indicate that the slip rate on other faults may have decreased. Alternatively, the total amount of slip in the system may have overall increased, with increased slip rates on other faults in addition to the Osaka Bay Fault. Based on the recent occurrence of the 1995 M_w6.8 Kobe (Southern Hyogo prefecture) Earthquake on the Rokko-Awaji Island Fault zone, it is possible that the fault activity of the whole system may have increased since the Late Pleistocene, leading to greater seismic risks in this region. It is crucial to study recent slip rates on other faults in order to fully evaluate the regional fault activities.

Fault slip rates in this region could reasonably be expected to have been transient during recent and earlier periods. Thus, while previous studies have inferred that the average slip rates have been fairly constant through time (e.g., Yokokura et al. 1998), other studies have demonstrated fluctuations in past slip rates (possibly from as low as ~ 0.1 mm/yr to as high as ~ 1.0 mm/yr) on the Uemachi, Osaka Bay, and the Rokko-Awaji Island Fault zones beneath the northern Osaka and Kobe Basins and in the Osaka Bay during the Middle Pleistocene (Itoh et al. 2000; Grothe et al. 2014). Grothe et al. (2014) reported variable fault slip in space and time, in which the Osaka Bay Fault propagated at greater rates in the north compared to the south, after its reactivation and onset of slip (~ 1.5 Ma), later building more slip around profile GS-8ME. Itoh et al. (2000) detected three main episodic changes occurring within the Osaka and Kobe Basins, where the subsidence rates show a sharp decline during the Ma 5/6 interval (~ 712–621 ka), followed by a second episode of differential rise and fall of subsidence rate occurred during Ma 7/8 (~578–528 ka), and a third episode of reduced subsidence on the western and eastern edge of the basin during Ma 8/9 (~528–427 ka) (Itoh et al. 2000). The first episode at Ma 5/6 corresponds to the Mantidani Unconformity (Huzita 1990), an upward-coarsening facies boundary at the base of the Upper Osaka Group found in the Awaji Island, Kobe and the Osaka Basin, implying a regional event (Inoue et al. 2003). Previous studies have attributed this episodic decline of subsidence in the northern Osaka Basin to be linked with the shift of the western part of the Median Tectonic Line at about ~700 ka (Itoh et al. 1998, 2000). The second and third episodic changes are inferred to link with the build-up of the Uemachi Basement High and the N-S warping of the sedimentary basin that caused accelerated north-westward tilting and subsidence in the south-eastern Osaka Basin during the Middle to Late Pleistocene (Itoh et al. 2000, 2001).

Fault slip rates are important because they are used in seismic hazard assessments, as a proxy for moment release along a fault over time, where they are merged with records of earthquake magnitude and recurrence intervals inferred from paleoseismic investigations and historical earthquakes (e.g., Matsuda 1975, Kanaori 2000; The Headquarters for Earthquake Research Promotion 2001; Mueller 2017). Our study investigates slip rates over the last several to tens of ky, owing to the continuous fold growth strata preserved in the sedimentary basin and high-resolution seismic imaging techniques coupled with drilling. These intermediate time-scales allow the identification of transient fault slip rates and bridge the observational time gaps between geologic cross sections that average longer time scales (~few mys) and short-term observations based on paleoseismology (~few hundred yrs to several kys), geodesy and seismology (~few seconds to few yrs). Transient fault slip rates indicate changes in potential earthquake magnitudes, frequencies, slip distributions, and/or interactions with surrounding faults with time, and this time-variant nature challenges characteristic earthquake cycle models that typically assume repeating rupture size and displacement on individual fault segments (e.g., Grant 1996; Bergen et al. 2017; Nakatani 2020). In this study, we highlight the importance of using observations of slip rates averaged over intermediate (Late Pleistocene-Holocene) time scales, and incorporating these aspects to improve earthquake models for potential seismic hazard assessments.

5.3 Implications for regional tectonics and comparisons with geodetic slip rates

5.3.1 The onset of active faulting related to forearc sliver

The differential right-lateral and vertical slip motions of regional faults resulted in the formation of the Osaka, Kobe, and Nara Basins, bounded by the Rokko, Ikoma, and Suzuka Mountains within the Kinki Triangle (Huzita 1962). The vertical slip component is accommodated largely by fold-and-thrust faulting, with folding being dominant in the sedimentary section (Ishiyama 2003; Sato et al. 2009), as observed in this study. The bases of the sedimentary basins are dated ~3 Ma, which is coincident with the timing of reactivation of regional faults such as the Median Tectonic Line (Maruyama & Lin 2004; Famin et al. 2014). However, on the basis of regional unconformities and marine clay distributions within the Osaka Group, previous studies have inferred that the subsidence of basins and uplift of ranges occurred rapidly after ~1 Ma, indicating that the activity of major faults in the region accelerated < ~1 Ma (Huzita 1990; Itoh et al. 2000; Kato et al. 2008). A broad distribution of marine clay Ma 1, 2 and 3 (~1070 ka, 960 ka, and ~865 ka, respectively) of the Middle Osaka Group is identified within the Kyoto and Nara Basins that extend from the Osaka Basin across the Rokko and Ikoma Mountains, and the preservation of these strata across these elevated ranges indicates that uplift was not significant during deposition of Ma 1–4, and that significant uplift occurred later (e.g. Huzita 1990). During and possibly prior to this period (~3–1 Ma), the basement rocks of the Ryoke Group were likely deformed via a detachment fold without localized uplift (Huzita 1990; Poblet and McClay 1996). Whereas, the marine clays of the Upper Osaka Group (Ma 6 ~) (< 621 ka) are not deposited on the mountains and are only preserved in the basins, with the strata clearly offset by dominant faulting and fault-related folding that have likely accelerated after ~1 Ma (e.g., Huzita 1990). The current arrangement of the basins and mountain ranges are therefore likely a topographic expression of the faulted blocks in the basement rocks that have propagated to the sedimentary section (Huzita 1990; Itoh et al. 2000).

The onset of the current tectonic framework in SW Japan is governed by the oblique subduction of the Philippine Sea Plate along the Nankai, Ryukyu and Philippine Trenches, which is estimated to have initiated around ~6 Ma, as inferred from ocean drilling results in the Nankai subduction zone (Moore et al. 2015; Kimura et al. 2014, 2018), geologic surveys on the Median Tectonic Line (Maruyama and Lin 2004; Famin et al. 2014), and plate reconstruction models (Wu et al. 2016). The slip sense of the Median Tectonic Line changed from dominantly reverse faulting to right-lateral strike-slip faulting at around ~3 Ma (Maruyama and Lin 2004; Famin et al. 2014), suggesting that the oblique subduction strengthened during this period. The contemporary left-stepping dextral Median Tectonic Line is likely a result of translation of the forearc sliver, in addition to reactivation of other major E–W trending dextral faults to the north (e.g., Arima-Takatsuki Fault zone) (e.g., Kanaori 1990; Tsukuda 1992). The NE–SW to N-S trending faults north of the Median Tectonic Line, such as the Nojima, Osaka Bay, Uemachi, and Ikoma Faults, have likely initiated as en echelon right-lateral- and reverse faults and folds associated with the forearc sliver (e.g., Tsukuda 1992), evolving from a detachment fold system to a fault-propagation fold system as the structures matured and as more sediments accumulated.

The onset of contemporary inland active faulting and the growth of the accretionary prism at the Nankai subduction zone were likely punctuated events occurring in several time steps; ~ 6 Ma, ~ 3 Ma, ~ 2 Ma, and ~ 1 Ma, most likely related to the kinematics of the plate subduction (e.g., Moore et al. 2001, 2015; Kimura et al. 2018). Seismic reflection studies coupled with drillings along the Nankai Trough have shown a major unconformity at ~ 6 Ma that implied resurgence of Philippine Sea Plate subduction after a long period of cessation since ~ 12 Ma (Kimura et al. 2018). Drilling results have also indicated rapid formation of the frontal prism (imbricated thrust zone) in the Nankai Trough after ~ 2 Ma (e.g., Moore et al. 2001), and rapid < ~ 2 Ma uplift on the megasplay fault and landward tilting in the Kumano Basin (e.g., Moore et al. 2015), in addition to strike-slip faulting inferred along the Kumano Basin Edge Fault zone (e.g., Martin et al. 2010). The punctuated growths of the offshore accretionary prisms and forearc basins are inferred to be coincident with the period when the slip sense of the Median Tectonic Line changed to right-lateral strike-slip faulting (e.g., Maruyama and Lin 2004; Famin et al. 2014), suggesting a large-scale tectonic reorganization that involved vast areas of the upper plate. The volcanic activities around the Beppu-Shimabara grabens and the Higo volcanic zone are also reported to have onset at ~ 5–6 Ma and ~ 2 Ma (e.g., Kamata and Kodama 1994). The opening of the Okinawa Trough is also coincident with these periods (e.g., Sibuet et al. 1987). Plio-Pleistocene sedimentary basins were formed in many parts of the region, likely related to tectonic events (e.g., Nakajima 2018).

The recent tectonic phase may also relate to the initiation of convergence of the Amurian Plate with the Okhotsk Plate along the eastern margin of the Japan Sea (Kimura et al. 2018; Nishimura et al. 2018). Previous studies have inferred similarities in geodetic strains and tectonic block movements east of Awaji Island with the blocks in the Kanto region that is known as part of the Okhotsk Plate, implying the presence of a N-S trending tectonic boundary that may explain the regional E–W compression (Nishimura et al. 2018).

5.3.2 Comparisons with geodetic strain rates

The contemporary crustal deformation in southwest Japan has been monitored by dense GNSS (Global Navigation Satellite System) networks represented by GEONET (GNSS Earth Observation Network System) onland stations and GPS-A (Global Positioning System-Acoustic) seafloor stations (e.g. Sagiya 2004; Yokota et al. 2016; Nishimura et al. 2018) (Fig. 1b). The inland velocity fields in most regions show west-northwestward movement almost parallel to the motion of the subducting Philippine Sea Plate along the Nankai Trough, suggesting strong interplate coupling at the subduction zone (Nishimura et al. 2018) (Fig. 1b). The existence of numerous active faults and high seismicity on the island arc and continental crust of Japan are consistent with significant slip partitioning and diffuse deformation in the upper plate (Fig. 1a). While the strain rate distribution in the inland regions are not homogeneous, several zones of strain concentration are recognized from GNSS data (Loveless and Meade 2010; Nishimura et al. 2018). One of the most active boundaries with geodetic slip rates of ≥ 9 mm/yr is the Median Tectonic Line, accommodating part of the margin-parallel component of the current oblique convergence by right-lateral shear motion (Loveless and Meade 2010; Nishimura et al. 2018) (Fig. 1b). Another significant high-strain rate zone is the Niigata–Kobe Tectonic Zone, a ~ 50–200 km wide NE–SW trending zone north of the Median Tectonic Line which has large geodetic slip rates of > 15 mm/yr (e.g., Sagiya et al. 2000; Loveless and Meade 2010; Nishimura et al. 2018) (Fig. 1b). The active faults around the Osaka Bay and the Kinki Triangle constitutes the southern portion of the Niigata–Kobe Tectonic Zone (Fig. 1ab).

Loveless and Meade (2010) and Nishimura et al. (2018) defined a tectonic block around the Kinki Triangle bounded by the Rokko-Awaji Island Fault zone, the Arima-Takatsuki Fault zone, and the Median Tectonic Line in their models, and inferred large internal strain rates of − 52.4 to − 82.8 nanostrain/yr within the block surrounding Osaka. The geodetic strain rate (surface deformation) within the Kinki Triangle expressed as a sum of rigid block rotations and interseismic elastic deformation due to locked faults on the block boundaries (Nishimura et al. 2018) is estimated to be ~ 15 mm/yr (T. Nishimura, personal communication, December 2023). The compressional strain within the block dominates in a direction of relative plate convergence, and is nearly perpendicular to the NE–SW trending Osaka Bay Fault and other faults such as the Uemachi and Ikoma Faults, which may indicate relatively dominant dip-slip thrusting for these faults, whereas right-lateral slip is relatively dominant along E–W trending faults of the Rokko-Awaji

Island and Arima-Takatsuki Fault zones (Loveless and Meade 2010; Nishimura et al. 2018). Across the central–northern Osaka Bay (within a box extending ~ 140 km oriented perpendicular to the strike of the Osaka Bay Fault with its center aligned parallel to the fault), GNSS velocity data by Nishimura et al. (2018) suggest relative geodetic strain and shortening rates of ~ 10 to 11 mm/yr (T. Nishimura, personal communication, December 2023). The Late Pleistocene–Holocene slip rate (~ 1.1 to 1.8 mm/yr) on the Osaka Bay Fault estimated in our study (Sect. 5.2.1) may account for ~ 10 to 18% of the regional geodetic strain accumulation across the central–northern Osaka Bay (~ 10 to 11 mm/yr), and ~ 7.3 to 12% of the regional geodetic strain accumulation within the Kinki Triangle (~ 15 mm/yr). The remaining strain accumulation may be accommodated by other faults, which may indicate the possibility for more previously-unknown hidden faults in the region, and/or larger slip rates on other faults. By contrast, the interblock right-lateral motions along the Rokko-Awaji Island and Arima-Takatsuki Fault zones are inferred to range ~ 3 to 9 mm/yr, and ~ 3 to 6 mm/yr along the Median Tectonic Line (Nishimura et al. 2018), which is likely relatively more compatible with geologic slip rates of known faults. Geodetic strain rates generally include a sum of the slip rates and slip senses of individual faults existing in the system (e.g., Bourne et al. 1998). However, discrepancies between geodetic and geologic slip rates may arise from various processes such as by elastic deformation due to interplate coupling on the plate boundary included in geodetic strains, long-term (geologic) transient slip rates that are not accounted for in geodetic rates, and/or when there is significant amount of deep, inelastic deformation that is not expressed in geomorphological features and hence excluded in geologic slip rates (e.g., Hashimoto 1990; Meade and Hager 2005; Ohzono et al. 2011; Johnson 2013). We demonstrate that a detailed study of Holocene slip rates of regional faults is necessary to assess the seismic hazards and the internal strain budgets within the Kinki Triangle and the Niigata–Kobe Tectonic Zone.

6 Conclusion

To investigate the shallow structure and recent deformation history of active faults in the Osaka Bay, we acquired high-resolution seismic profiles and multi-beam bathymetry data across the central segment of the Osaka Bay Fault. Our main results are:

(1) The Osaka Bay Fault is characterized by an asymmetric anticline at shallow depths, composed of a ~ 0.1–3.7-km-wide, steeper forelimb that dips east and a gentler and broader backlimb that dips west, associated with an additional ~ 2.6-km-wide syncline at the western extent of the anticline. Towards the eastern side of our sections, the tilted strata dip gently west, forming a broad ~ 11-km-wide syncline in the footwall. Our seismic data confirm that the Osaka Bay Fault is blind, and that the deformation reaches near surface by a fault-propagation fold. The forelimb and backlimb of the fault-propagated anticline progressively steepens with depth, and the overall monocline widens at shallower depths.

(2) The synclinal axial surface at shallow depths measured in this study ranges from 75 to 89°. This dip observed at shallower depths is steeper than measured in previous studies (~ 72°) from deep seismic lines. The steeper dips of the synclinal axial surface at shallow depths are associated with an upward propagating growth triangle with ongoing sedimentation. The presence of a backlimb on the fault-related fold may also relate to the steepening of the trishear envelope. The shallow structure of the fault documented by our study in previously unavailable detail provide insights on the subsurface deformation by the Osaka Bay Fault.

(3) Our northern, central, and southern sections clearly show that the dip of the anticline forelimb is steeper in the northern area (~ 0.4 to 15°) with larger offsets across the fold, compared to that of the south (~ 0.2 to 5.2°). The sediment thickness on the hanging wall, however, is variable (north > > central < south), suggesting that erosion does not balance uplift. We attribute this variation to varied mobilization of sediment by tidal currents active in the bay during the Holocene. Major sequence boundaries such as onlap of recent sediments onto tilted strata and basal erosional surfaces during marine transgression and sea level highstands are inferred to affect the geometry of growth strata.

(4) In the northern Osaka Bay, the most recent deformation by the Osaka Bay Fault reaches to near the seafloor by active folding, with large vertical offsets of ~ 8–14 m over the last ~ 11 ka, and ~ 5–11 m over the last ~ 5 ka. By combining with previously reported borehole age data, the average uplift rate on the Osaka Bay Fault during the Late Pleistocene to Holocene in this study is estimated to be ~ 1.0 to 1.7 m/ka, larger than the uplift rates previously documented (~ 0.5 to 0.7 m/ka) from deeper sections spanning the Pleistocene (Yokokura et al. 1998; Iwabuchi et al. 2000).

(5) The inferred slip on the Osaka Bay Fault during the Late Pleistocene–Holocene may account for ~ 7.3 to 12% of the regional geodetic strain accumulation within the Kinki Triangle. Further studies to evalu-

ate the Holocene slip rates of regional faults are necessary for the assessment of seismic hazards and the internal strain budgets within the Kinki Triangle and the Niigata–Kobe Tectonic Zone.

Abbreviations

"Ma 1"–"Ma13"	Marine clay beds 1–13
"TWT"	Two-way travel time

Supplementary Information

The online version contains supplementary material available at https://doi.org/10.1186/s40645-024-00607-0.

Additional file 1. Figures S1 to S33.

Additional file 2. Table S1. Measured depths of seismic horizons shown in Figure 24 (main text).

Additional file 3. Table S2. Measured depths of seismic horizons and marine clays.

Additional file 4. Table S3. Measured uplift and inferred age along seismic horizons.

Acknowledgements
We are grateful to Editor Ken Ikehara for handling our manuscript, and to Karl Mueller and an anonymous reviewer for their constructive and insightful reviews that have helped improve this contribution. We express our gratitude to Yoshiji Yano, Masaki Fuchi, and crew members of the T/S Fukaemaru for the operation of the ship during our surveys. We are grateful to Morihito Ishu for the operation of the R/V Onokoro, and Masata Suzuki and Satomi Takagi for their assistance on the ship. We are thankful to Shinya Uwai and staff members from the Research Center for Inland Seas, Kobe University (KURCIS) for their hospitality during our stay at the Marine Site (Joint Usage/Education Center of MEXT). We are grateful to Takahiko Inoue, Ayanori Misawa, Tomoyuki Sato, Fumitoshi Murakami, Kohsaku Arai, and Rei Nakashima for useful discussions. We are thankful to Takuya Nishimura for the valuable discussions and insights on geodetic strain rates around the Osaka Bay. We express our gratitude to Tomoichi Enomoto, Shin Terado, Mitsutec Corp., Hiruzen Institute for Geology and Chronology Co., Ltd., Masayoshi Kondo, Nakagawa Textile Co., Ltd., and Seisgadget Ltd., for their contribution in the academic crowdfunding to investigate the active faults in the Osaka Bay (Academist Project #111). We thank all the students and staffs that have participated in the seismic surveys during the marine geophysics field class held during the period of 2017–2021 onboard the T/S Fukaemaru at Kobe University.

Author contributions
MH, HO, YS, JA, TM, NS, SS, HI, MS, KS, KK and KN contributed in data acquisition. HI, HO, JA and YS conducted seismic data processing. MS carried out processing of bathymetry and backscatter data. MH analyzed the data and constructed the manuscript. YT and HS acquired funding. MH, HO, YS, JA, NS, YY, SAB, HS and YT contributed in investigation, data interpretation, and conceptualization. All authors participated in reviewing the manuscript and approving the final version.

Funding
This research was supported by the Kobe-Ocean Bottom Exploration Center, Geological Survey of Japan, and academic crowdfunding to investigate the active faults in the Osaka Bay (Academist Project #111). MH received travel support to present at the International Joint Workshop on Slow-to-Fast Earthquakes 2023 supported by JSPS KAKENHI Grant Number JP21H05200 in Grant-in-Aid for Transformative Research Areas (A) "Science of Slow-to-Fast Earthquakes".

Availability of data and materials
All data used in this study will be uploaded to a FAIR-aligned data repository upon publication.

Declarations

Competing interests
The authors declare that they have no competing interest.

Author details
[1]Kobe Ocean-Bottom Exploration Center, Kobe University, 5-1-1 Fukaeminamimachi, Higashinada, Kobe 658-0022, Japan. [2]Geological Survey of Japan, National Institute of Advanced Industrial Science and Technology, 1-1-1 Higashi, Tsukuba, Ibaraki 305-8567, Japan. [3]Department of Planetology, Graduate School of Science, Kobe University, 1-1 Rokkodai, Nada, Kobe 657-8501, Japan. [4]School of Geosciences, University of Aberdeen, King's College, Aberdeen AB24 3FX, UK. [5]Nippon Marine Enterprises, Ltd., 14-1 Ogawacho, Yokosuka, Kanagawa 238-0004, Japan. [6]Seisgadget Ltd, 3-31-11, Ohmori-Kita, Ohta-Ku, Tokyo 143-0016, Japan. [7]School of Marine Resources and Environment, Tokyo University of Marine Science and Technology, 4-5-7 Konan, Minato-Ku, Tokyo 108-8477, Japan. [8]Present Address: Faculty of Global and Science Studies, Yamaguchi University, 1677-1 Yoshida, Yamaguchi 753-8541, Japan.

Received: 10 April 2023 Accepted: 2 February 2024
Published online: 14 February 2024

References

Afnimar KK, Nakagawa K (2002) Joint inversion of refraction and gravity data for the three-dimensional topography of a sediment-basement interface. Geophys J Int 151(1):243–254. https://doi.org/10.1046/j.1365-246X.2002.01772.x

Allmendinger RW (1998) Inverse and forward numerical modeling of trishear fault-propagation folds. Tectonics 17(4):640–656. https://doi.org/10.1029/98TC01907

Almeida RV, Hubbard J, Liberty L, Foster A, Sapkota SN (2018) Seismic imaging of the Main Frontal Thrust in Nepal reveals a shallow décollement and blind thrusting. Earth Planet Sci Lett 494:216–225. https://doi.org/10.1016/j.epsl.2018.04.045

Awata Y, Mizuno K, Sugiyama Y, Shimokawa K, Imura & Kimura K, (1995) Surface faults associated with the Hyogoken nanbu earthquake of 1995. Chishitsu News 486(16–20):1995 (**(In Japanese)**)

Awata Y, Mizuno K, Sugiyama Y, Imura R, Shimokawa K, Okumura K, Tsukuda E, Kimura K (1996) Surface fault ruptures on the northwest coast of Awaji Island associated with the Hyogo-ken Nanbu Earthquake of 1995. Jpn J Seismol Soc Jpn (zisin) 49(1):113–124. https://doi.org/10.4294/zisin1948.49.1_113

Baba T, Cummins PR (2005) Contiguous rupture areas of two Nankai Trough earthquakes revealed by high-resolution tsunami waveform inversion. Geophys Res Lett 32(8):L08305. https://doi.org/10.1029/2004GL022320

Bergen KJ, Shaw JH (2010) Displacement profiles and displacement-length scaling relationships of thrust faults constrained by seismic-reflection data. Geol Soc Am Bull 122:1209–1219. https://doi.org/10.1130/B26373.1

Bergen KJ, Shaw JH, Leon LA, Dolan JF, Pratt TL, Ponti DJ, Morrow E, Barrera W, Rhodes EJ, Murari MK, Owen LA (2017) Accelerating slip rates on the Puente Hills blind thrust fault system beneath metropolitan Los Angeles, California, USA. Geology 45(3):227–230. https://doi.org/10.1130/G38520.1

Berger A, Loutre MF (1991) Insolation values for the climate of the last 10 million years. Quat Sci Rev 10(4):297–317. https://doi.org/10.1016/0277-3791(91)90033-q

Biswas DK, Hyodo M, Taniguchi Y, Kaneko M, Katoh S, Sato H, Kinugasa Y, Mizuno K (1999) Magnetostratigraphy of Plio-Pleistocene sediments in a 1700-m core from Osaka Bay, southwestern Japan and short geomagnetic events in the middle Matuyama and early Brunhes chrons. Palaeogeogr Palaeoclimatol Palaeoecol 148(4):233–248. https://doi.org/10.1016/S0031-0182(98)00185-0

Bourne SJ, England PC, Persons B (1998) The motion of crustal blocks driven by flow of the lower lithosphere and implications for slip rates of continental strike-slip faults. Nature 391:665–659. https://doi.org/10.1038/35556
Calais E, Freed AM, Van Arsdale R, Stein S (2010) Triggering of new madrid seismicity by late-pleistocene erosion. Nature 466:608–611. https://doi.org/10.1038/nature09258
Cardozo N, Jackson CAL, Whipp PS (2011) Determining the uniqueness of best-fit trishear models. J Struct Geol 33(6):1063–1078. https://doi.org/10.1016/j.jsg.2011.04.001
Catuneanu O, Abreu V, Bhattacharya JP, Blum MD, Dalrymple RW, Eriksson PG, Fielding CR, Fisher WL, Galloway WE, Gibling MR, Giles KA, Holbrook JM, Jordan R, St C, Kendall CG, Macurda B, Martinsen OJ, Miall AD, Neal JE, Nummedal D, Pomar L, Posamentier HW, Pratt BR, Sarg JF, Shanley KW, Steel RJ, Strasser A, Tucker ME, Winker C (2009) Towards the standardization of sequence stratigraphy. Earth Sci Rev 92(1–2):1–33. https://doi.org/10.1016/j.earscirev.2008.10.003
Collier JS, Brown CJ (2005) Correlation of sidescan backscatter with grain size distribution of surficial seabed sediments. Mar Geol 214(4):431–449. https://doi.org/10.1016/j.margeo.2004.11.011
Committee for Catalog of Quaternary Volcanoes in Japan (1999) Catalog of Quaternary volcanoes in Japan, ver.1.0, Volcanological Society of Japan
Erslev EA (1991) Trishear fault-propagation folding. Geology 19(6):617–620. https://doi.org/10.1130/0091-7613(1991)019%3c0617:TFPF%3e2.3.CO;2
Famin V, Raimbourg H, Garcia S, Bellahsen N, Hamada Y, Boullier A, Fabbri O, Michon L, Uchide T, Ricci T, Hirono T, Kawabata K (2014) Stress rotations and the long-term weakness of the Median Tectonic Line and the Rokko-Awaji Segment. Tectonics 33(10):1900–1919. https://doi.org/10.1002/2014TC003600
Ferrini VL, Flood RD (2006) The effects of fine-scale surface roughness and grain size on 300 kHz multibeam backscatter intensity in sandy marine sedimentary environments. Mar Geol 228(1–4):153–172. https://doi.org/10.1016/j.margeo.2005.11.010
Freed A (2005) Earthquake triggering by static, dynamic and postseismic stress transfer. Annu Rev Earth Planet 33:335–367. https://doi.org/10.1146/annurev.earth.33.092203.122505
Fujiwara T, Higo T, Takasugi Y (1989) Osakawan no koryu to choryu•uzu. Proc Coast Eng 36:209–213. https://doi.org/10.2208/proce1989.36.209
Furumura T, Koketsu K (1998) Specific distribution of ground motion during the 1995 Kobe earthquake and its generation mechanism. Geophys Res Lett 25(6):785–788. https://doi.org/10.1029/98GL50418
Geological Survey of Japan, AIST (2022) Seamless digital geological map of Japan V2 1: 200,000. https://gbank.gsj.jp/seamless. Accessed 24 Jul 2022
Grant LB (1996) Uncharacteristic earthquakes on the San Andreas fault. Science 272:826–827. https://doi.org/10.1126/science.272.5263.826
Goff JA, Olson HC, Duncan CS (2000) Correlation of side-scan backscatter intensity with grain-size distribution of shelf sediments. New Jersey Margin Geo-Mar Lett 20(1):43–49. https://doi.org/10.1007/s003670000032
Grothe PR, Cardozo N, Mueller K, Ishiyama T (2014) Propagation history of the Osaka-wan blind thrust, Japan, from trishear modeling. J Struct Geol 58:79–94. https://doi.org/10.1016/j.jsg.2013.10.014
Hallier S, Chaljub E, Bouchon M, Sekiguchi H (2008) Revisiting the basin-edge effect at Kobe during the 1995 Hyogo-ken Nanbu Earthquake. Pure Appl Geophys 165:1751–1760. https://doi.org/10.1007/s00024-008-0404-y
Hallo M, Opršal I, Asano K, Gallovič F (2019) Seismotectonics of the 2018 northern Osaka M6.1 earthquake and its aftershocks: joint movements on strike-slip and reverse faults in inland Japan. Earth Planets Space 71:34. https://doi.org/10.1186/s40623-019-1016-8
Hamahashi M, Hubbard JA, Almeida RV, Haines SH, Owen LA, Mishra S, Sapkota SN (2022) Fluvial sedimentary response to late quaternary climate and tectonics at the himalayan frontal Thrust Central Nepal. Geochem Geophys Geosyst. https://doi.org/10.1029/2022GC010366
Hardy S, Ford M (1997) Numerical modeling of trishear fault propagation folding. Tectonics 16(5):841–854. https://doi.org/10.1029/97TC01171
Hardy S, Allmendinger RW (2011) Trishear: A review of kinematics, mechanics, and applications, in K. McClay, J. Shaw, and J. Suppe, eds., Thrust fault-related folding: AAPG Memoir 94, 95–119. https://doi.org/10.1306/13251334M943429
Hashimoto M (1990) Horizontal strain rates in the Japanese islands during interseismic period deduced from geodetic surveys (Part 1): Honshu, Shikoku and Kyushu. Zishin 43:13–26 (**in Japanese with English abstract**)
Hayakawa M, Mori K, Kamata S, Fujita K (1964) Sonic method survey at Osaka Bay. Bull Geol Surv Japan 15: 1–26. https://dl.ndl.go.jp/info:ndljp/pid/9616146 (**In Japanese with English abstract**)
Hirata N, Ohmi S, Sakai S, Katsumata K, Matsumoto S, Takanami T, Yamamoto A, Iidaka T, Urabe T, Sekine M, Ooida T, Yamazaki F, Katao H, Umeda Y, Nakamura M, Seto N, Matsuhima T, Shimizu H, Japanese University Group of the Urgent Joint Observation for the 1995 Hyogo-ken Nanbu Earthquake (1996) Urgent Joint Observation of Aftershocks of the 1995 Hyogo-ken Nanbu Earthquake. J Phys Earth 44 (4): 317–328. https://doi.org/10.4294/jpe1952.44.317
Hirata N, Kimura R (2018) The Earthquake in Osaka-Fu Hokubu on 18 June 2018 and its ensuing disaster. J Disaster Res 13(4):813–816. https://doi.org/10.20965/jdr.2018.p0813
Honda R, Yomogida K (2003) Effect of complex fault geometry and slip style on near-fault strong motions and static displacement. Earth Planets Space 55(9):515–530. https://doi.org/10.1186/BF03351785
Huzita K (1962) Tectonic development of the Median Zone (Setouti) of southwest Japan, since the Miocene: With special reference to the characteristic structure of central Kinki area. J Geosci Osaka City Univ 6:103–144
Huzita K, Maeda Y (1969) Latest Quaternary deposits in Osaka Bay. Quat Res 8(3):89–100. https://doi.org/10.4116/jaqua.8.89
Huzita K, Maeda Y (1984) Geology of the Suma district. Quadrangle Series, scale 1:50,000, Geol. Surv. Japan, 101 p. https://www.gsj.jp/data/50KGM/PDF/GSJ_MAP_G050_11061_1984_D.pdf (**in Japanese with English abstract**)
Huzita K (1990) Manchidani Unconformity and Rokko movements -Middle Pleistocene fault-block movement and sea-level rise in Kinki. Japan Quat Res 29(4):337–349. https://doi.org/10.4116/jaqua.29.337
Hyodo M, Morinaga H, Nishimura H, Inokuchi H, Yasukawa K (1985) Paleomagnetism of a core from Osaka Bay. J Geomagn Geoelectr 37(7):729–737. https://doi.org/10.5636/jgg.37.729
Ide S, Takeo M, Yoshida Y (1996) Source process of the 1995 Kobe earthquake: determination of spatio-temporal slip distribution by Bayesian modeling. Bull Seismol Soc Am 86(3):547–566. https://doi.org/10.1785/BSSA0860030547
Ikebe N, Iwatsu J, Takenaka J (1970) Quaternary geology of Osaka with special reference to land subsidence. J Geosci Osaka City Univ 13:39–98
Ikeda Y, Togo M, Sawa H (1995) Maximum slip vector on the Nojima Fault associated with the Hyogoken Nanbu, Western Japan, Earthquake of January 17, 1995. J Seismol Soc Japan (zisin) 48(4):531–537. https://doi.org/10.4294/zisin1948.48.4_531
Ikeda M, Toda S, Onishi K, Nishizaka N, Suzuki S (2019) The 1596 Keicho earthquake, a 5-day, 300-km-long sequential rupture event in the Median Tectonic Line fault zone, southwestern Japan. J Geophys Res: Solid Earth 124:8376–8403. https://doi.org/10.1029/2018JB017264
Ikehara K, Kinoshita Y (1994) Distribution and origin of subaqueous dunes on the shelf of Japan. Mar Geol 120(1–2):75–87. https://doi.org/10.1016/0025-3227(94)90078-7
Imanishi K, Ohtani M, Uchide T (2020) Driving stress and seismotectonic implications of the 2013 Mw5.8 Awaji Island earthquake, southwestern Japan, based on earthquake focal mechanisms before and after the mainshock. Earth Planets Space 72:158. https://doi.org/10.1186/s40623-020-01292-1
Inoue N, Kitada N, Itoh Y, Takemura K, Nakagawa K (2003) Integrated study of high resolution geophysical and geological information of Osaka Bay, southwest Japan. J Asian Earth Sci 22:1–11. https://doi.org/10.1016/S1367-9120(03)00038-5
Irikura K, Iwata T, Sekiguchi H, Pitarka A (1996) Lesson from the 1995 Hyogo-ken Nanbu Earthquake: Why were such destructive motions generated to buildings? J Nat Disaster Sci 17(2):99–127
Irizuki T, Masuda F, Miyahara B, Hirotsu A, Ueda S, Yoshikawa S (2001) Vertical changes of Holocene ostracods in bore hole cores from off Kobe, related to the opening of straits and relative sea-level change in western Japan. Quat Res 40(2):105–120
Ishitsuka K, Tsuji T, Lin W, Kagabu M, Shimada J (2020) Seasonal and transient surface displacements in the Kumamoto area, Japan, associated

with the 2016 Kumamoto earthquake: implications for seismic-induced groundwater level change. Earth Planets Space 72:144. https://doi.org/10.1186/s40623-020-01275-2
Ishiyama T (2003) Geometry and kinematics of the Uemachi and Ikoma fault zones beneath Metropolitan Osaka, central Japan. Ann. Rep. Active Fault Paleoearthquake Res 3:145–155
Ishiyama T, Mueller K, Sato H, Togo M (2007) Coseismic fault-related fold model, growth structure, and the historic multisegment blind thrust earthquake on the basement-involved Yoro thrust, central Japan. J Geophys Res 112:B03S07. https://doi.org/10.1029/2006JB004377
Itihara M (1960) Some problems of the Quaternary sedimentaries, Osaka and Akashi areas. Earth Sci (chikyu Kagaku) 49:15–25. https://doi.org/10.15080/agcjchikyukagaku.1960.49_15
Itihara M (Eds.) (1993) *The Osaka Group*. Osaka, Japan: Sogensha. (**In Japanese**)
Ito M, Kameo K, Satoguchi Y, Masuda F, Hiroki Y, Takano O, Nakajima T, Suzuki N (2016) Neogene-Quaternary sedimentary successions. The Geology of Japan. Geological Society of London, London, pp 309–337
Itoh Y, Takemura K, Kamata H (1998) History of basin formation and tectonic evolution at the termination of a large transcurrent fault system: deformation mode of central Kyushu. Japan Tectonophysics 284(1–2):135–150. https://doi.org/10.1016/S0040-1951(97)00167-4
Itoh Y, Takemura K, Ishiyama T, Tanaka Y, Iwaki H (2000) Basin formation at a contractional bend of a large transcurrent fault: Plio-Pleistocene subsidence of the Kobe and northern Osaka Basins. Japan Tectonophysics 321(3):327–341. https://doi.org/10.1016/S0040-1951(00)00072-X
Itoh Y, Takemura K, Kawabata D, Tanaka Y, Nakaseko K (2001) Quaternary tectonic warping and strata formation in the southern Osaka Basin inferred from reflection seismic interpretation and borehole sequences. J Asian Earth Sci 20(1):45–58. https://doi.org/10.1016/S1367-9120(01)00019-0
Itoh Y, Kusumoto S, Takemura K (2013a) Characteristic basin formation at terminations of a large transcurrent fault—basin configuration based on gravity and geomagnetic data. In: Mechanism of sedimentary basin formation—multidisciplinary approach on active plate margins. InTech, Croatia 255–272. https://doi.org/10.5772/56702
Itoh Y, Takemura K, Kusumoto S (2013b) Neotectonic inter-arc basins within southwest Japan -Conspicuous basin-forming process related to differential motions of crustal blocks. In: Mechanism of sedimentary basin formation—multidisciplinary approach on active plate margins. InTech, Croatia 191–206. https://doi.org/10.5772/56588
Itoh Y, Takemura K (2019a) Basic knowledge -Stratigraphy of the Osaka Group. In: Three-Dimensional Architecture and Paleoenvironments of Osaka Bay. Adv Geol Sci 25–40. https://doi.org/10.1007/978-981-13-0577-1_2
Itoh Y, Takemura K (2019b) Reflection Seismic Data. In: Three-Dimensional Architecture and Paleoenvironments of Osaka Bay. Adv Geol Sci 41–102. https://doi.org/10.1007/978-981-13-0577-1_3
Itoh Y, Takemura K (2019c) Discussion -Origin and evolution of the Osaka Basin. In: Three-Dimensional Architecture and Paleoenvironments of Osaka Bay. Adv Geol Sci 103–119. https://doi.org/10.1007/978-981-13-0577-1_4
Inouchi Y (1982) Distribution of bottom sediments in the Seto Inland Sea-The influence of tidal currents on the distribution of bottom sediments. Journal Geol Soc Japan 88(8):665–681. https://doi.org/10.5575/geosoc.88.665(InJapanesewithEnglishabstract)
Inouchi Y (1990) Reconsideration of the subdivision of "Alluvium" in enclosed coastal seas -The example of Osaka bay-. Quat Res 29(5):405–416. https://doi.org/10.4116/jaqua.29.405
Iwabuchi Y, Kasuga S, Kokuta S, Okino K, Shimura E, Nagata S (1995) Active faults in the western Osaka Bay and adjacent area. J Japan Soc Mar Surv Tech 7(2):11–19. https://doi.org/10.11306/jsmst.7.2_11(inJapanesewithEnglishabstract)
Iwabuchi Y, Nishikawa H, Noda N, Yukimatsu T, Taga M, Miyano M, Sakai K, Fukazawa M (2000) Basement and active structures revealed by the seismic reflection survey in Osaka Bay. Rep Hydrograph Res 36: 1–23. https://dl.ndl.go.jp/pid/10115421/1/1 (in Japanese with English abstract)
Iwasaki Y, Kagawa T, Sawada S, Matsuyama S, Ohshima K, Ikawa T, Onishi M (1994) Basement structure by airgun reflection survey in Osaka Bay, southwest Japan. Jishin 46(4):395–403. https://doi.org/10.4294/zisin1948.46.4_395(inJapanesewithEnglishabstract)
Jamison WR (1987) Geometric analysis of fold development in overthrust terranes. J Struct Geol 9(2):207–219. https://doi.org/10.1016/0191-8141(87)90026-5
Japan Meteorological Agency (1995) The 1995 Hyogoken nanbu earthquake and its aftershocks. Rep Coord Comm Earthq Predict 54:584–592 ((**In Japanese)**)
Johnson KM (2013) Slip rates and off-fault deformation in southern California inferred from GPS data and models. J Geophys Res 118: 5643–5664, https:// doi .org /10.1002 /jgrb .50365
Kamata H, Kodama K (1994) Tectonics of an arc-arc junction: an example from Kyushu Island at the junction of the southwest Japan arc and Ryukyu arc. Tectonophysics 233(1–2):69–81. https://doi.org/10.1016/0040-1951(94)90220-8
Kanaori Y (1990) Late Mesozoic-Cenozoic strike-slip and block rotation in the inner belt of southwest Japan. Tectonophysics 177(4):381–399. https://doi.org/10.1016/0040-1951(90)90397-Q
Kanaori Y (2000) Seismic risk assessment of an active fault system: the example of the Tsurugawan-Isewan tectonic line. Eng Geol 56(1–2):109–123. https://doi.org/10.1016/S0013-7952(99)00137-4
Katao H, Maeda N, Hiramatsu Y, Iio Y, Nakao S (1997) Detailed mapping of focal mechanisms in/around the 1995 Hyogo-ken Nanbu Earthquake rupture zone. J Phys Earth 45(2):105–119. https://doi.org/10.4294/jpe1952.45.105
Kato S, Okada A, Sangawa A (2008) Active faults in the Rokko Mountains, Awaji Island and Osaka Bay area, and Quaternary development of the Osaka and Harimanada sedimentary basins, western Japan. Quat Res 47(4):233–246. https://doi.org/10.4116/jaqua.47.233(inJapanesewithEnglishabstract)
Kato A, Ueda T (2019) Source fault model of the 2018 M_w5.6 northern Osaka earthquake, Japan, inferred from the aftershock sequence. Earth Planets Space 71:11. https://doi.org/10.1186/s40623-019-0995-9
Kawata Y, Suzuki S, Koshimura S (2005) Osakawan rinkaitoshiiki-no tsunami-zeijakusei-to bosaitaisakukouka-no hyoka (title in Japanese). Proc Coastal Engineering, JSCE 52:1276–1280. https://doi.org/10.2208/proce1989.52.1276(inJapanese)
Kikuchi M, Kanamori H (1996) Rupture process of the Kobe, Japan, earthquake of Jan. 17 (1995) determined from teleseismic body waves. J Phys Earth 44(5):429–436. https://doi.org/10.4294/jpe1952.44.429
Kimura J, Stern RJ, Yoshida T (2005) Reinitiation of subduction and magmatic responses in SW Japan during Neogene time. Geol Soc Am Bull 117(7–8):969–986. https://doi.org/10.1130/B25565.1
Kimura G, Hashimoto Y, Kitamura Y, Yamaguchi A, Koge H (2014) Middle Miocene swift migration of the TTT triple junction and rapid crustal growth in southwest Japan: A review. Tectonics 33(7):1219–1238. https://doi.org/10.1002/2014TC003531
Kimura G, Koge H, Tsuji T (2018) Punctuated growth of an accretionary prism and the onset of a seismogenic megathrust in the Nankai Trough. Prog Earth Planet Sci 5:78. https://doi.org/10.1186/s40645-018-0234-1
Kitada N, Takemura K, Ito Y, Saito R, Miyakawa C, Mitamura M, Nanayama F, Iwabuchi Y (2001) Stratigraphic correlation between the OB-1 and OB-2 cores and its application to the activity evaluation of the Osaka-wan fault. Annu Rep Active Fault Paleoearthq Res 1:153–166
Kitada N, Mimura M (2016) Subsurface flexure of Uemachi Fault and its characteristics in Osaka plain. Jpn Geotech Soc Special Pub 2(19):715–718. https://doi.org/10.3208/jgssp.JPN-108
Kobayashi R, Koketsu K (2005) Source process of the 1923 Kanto earthquake inferred from historical geodetic, teleseismic, and strong motion data. Earth Planets Space 57:261–270. https://doi.org/10.1186/BF03352562
Kojima H (2020) Short and long term morphological changes and migration of sand waves in a semi-enclosed sea: a case study of Okinose area of Osaka Bay. MS Dissertation, Kobe University
Koketsu K, Miyake H (2008) A seismological overview of long-period ground motion. J Seismol 12:133–143. https://doi.org/10.1007/s10950-007-9080-0
Komazawa M, Shibuya S, Kumai M, Murakami M (1996) Sea bottom gravity survey of Osaka Bay and its study. Proc 94th SEGJ Conf 430–433. https://www.osti.gov/etdeweb/biblio/395567 (**In Japanese with English abstract**)
Kusumoto S, Fukuda Y, Takemura K, Takemoto S (2001) Forming mechanism of the sedimentary basin at the termination of the right-lateral

left-stepping faults and tectonics around Osaka Bay. J Geol Soc Japan 110(1):32–43. https://doi.org/10.5026/jgeography.110.32
Kusumoto S, Itoh Y, Takano O, Tamaki M (2013) Numerical modeling of sedimentary basin formation at the termination of lateral faults in a tectonic region where fault propagation has occurred. In: Mechanism of sedimentary basin formation: multidisciplinary approach on active plate margins. InTech. https://doi.org/10.5772/56558
Lamarche G, Lurton X, Verdier A, Augustin J (2011) Quantitative characterization of seafloor substrate and bedforms using advanced processing of multibeam backscatter -Application to Cook Strait, New Zealand. Cont Shelf Res 31:S93–S109. https://doi.org/10.1016/j.csr.2010.06.001
Lin A, Murayama T, Miyata T (1998) Paleoseismic events and the1596 Keicho-Fushimi large earthquake produced by a slip on the Gosukebashi fault at the eastern Rokko Mountains, Japan. Island Arc 7:621–636. https://doi.org/10.1046/j.1440-1738.1998.00214.x
Loveless JP, Meade BJ (2010) Geodetic imaging of plate motions, slip rates, and partitioning of deformation in Japan. J Geophys Res 115:B2. https://doi.org/10.1029/2008JB006248
Luttrell K, Sandwell D (2010) Ocean loading effects on stress at near shore plate boundary fault systems. J Geophys Res 115:B08411.
Martin KM, Gulick SPS, Bangs NLB, Moore GF, Ashi J, Park J-O, Taira Kuramoto S (2010) Possible strain partitioning structure between the Kumano fore-arc basin and the slope of the Nankai Trough accretionary prism. Geochem Geophys Geosyst. https://doi.org/10.1029/2009GC002668
Maruyama T, Lin A, Miyata T (1997) Deformational topography and late Quaternary activity of the Gosukebashi fault zone in the eastern Rokko Mountains, Japan. Active Fault Res 16:59–72. https://doi.org/10.11462/afr1985.1997.16_59(InJapanesewithEnglishabstract)
Maruyama T, Lin A (2004) Slip sense inversion on active strike-slip faults in southwest Japan and its implications for Cenozoic tectonic evolution. Tectonophysics 383(1–2):45–70. https://doi.org/10.1016/j.tecto.2004.02.007
Masuda F (1992) Depositional sequences of the Holocene and Upper Pleistocene in Osaka Bay. Japan J Sedimentol Soc Japan 37(37):71–77. https://doi.org/10.14860/jssj1972.37.71
Masuda F, Miyahara B (2000) Depositional facies and processes of the Holocene marine clay in the Osaka Bay area. Japan Quat Res 39(4):349–355. https://doi.org/10.4116/jaqua.39.349
Masuda F, Miyahara B, Hirotsu J, Irizuki T, Iwabuchi Y, Yoshikawa S (2000) Temporal variation of Holocene Osaka Bay conditions estimated from a core in off-Kobe. J Geol Soc Japan 106:482–488. https://doi.org/10.5575/geosoc.106.482
Masuda F, Itomoto N (2015) Temporal and spatial variations of accommodation and sediment accumulation during transgressive to highstand stages as reconstructed from a latest Pleistocene to Holocene sequence in the intra-arc Osaka Basin, Japan. Open J Geol 5:28–37. https://doi.org/10.4236/ojg.2015.51003
Matsuda T (1975) Magnitude and recurrence interval of earthquakes from a fault. Zisin 28:169–283
Matsushita R, Imanishi K (2015) Stress fields in and around metropolitan Osaka, Japan, deduced from microearthquake focal mechanisms. Tectonophysics 642:46–57. https://doi.org/10.1016/j.tecto.2014.12.011
McClay KR (1992) Glossary of thrust tectonics terms. Thrust tectonics 419–433
Meade BJ, Hager BH (2005) Block models of crustal motion in southern California constrained by GPS measurements. J Geophys Res 110:B03403. https://doi.org/10.1029/2004JB003209
Mitamura M, Yoshikawa Y, Ishii Y, Kaito S, Nagahashi Y (1998) Lithology on the OD drilling cores in the Osaka plain. Bull Osaka Mus Nat History 52:1–20
Mitamura M, Takemura K, Kitada N, Saito R (2000) Subsurface geology reviewed with drilling data in the kobe-hanshin region. Central Jpn Quat Res 39(4):319–330. https://doi.org/10.4116/jaqua.39.319
Miyahara B, Masuda F, Irizuki T, Fujiwara O, Yoshikawa S (1999) Holocene sea level curve and paleoenvironments reconstructed from a core in Osaka, Japan. Proceeding of Prof. K.O. Emery Commemorative International Workshop on Land-Sea link in Asia Sci and Tech Agency, Japan and Geol Surv Japan 415–420.
Miyazaki S, Heki K (2001) Crustal velocity field of southwest Japan: subduction and arc-arc collision. J Geophys Res 106(B3):4305–4326. https://doi.org/10.1029/2000JB900312
Mizuno K, Hattori H, Sangawa A, Takahashi Y (1990) Geology of Akashi district. Quadrangle series, I :50.000, Okayama (12) 83:90. (**in Japanese with English abstract**)
Mizuno K (2018) Study of tectonic development related to Plio-Pleistocene sedimentary basins with reference to the role of widespread tephras. Quat Res 57(3):85–95. https://doi.org/10.4116/jaqua.57.85
Moore GF, Taira A, Klaus A, Becker L, Boeckel B, Cragg BA, Dean A, Fergusson CL, Henry P, Hirano S, Hisamitsu T, Hunze S, Kastner M, Maltman AJ, Morgan JK, Murakami Y, Saffer DM (2001) New insights into deformation and fluid flow processes in the Nankai Trough accretionary prism: results of Ocean Drilling Program Leg 190. Geochem Geophys Geosyst. https://doi.org/10.1029/2001GC000166
Moore GF, Boston BB, Strasser M, Underwood MB, Ratliff RA (2015) Evolution of tectono-sedimentary systems in the Kumano Basin, Nankai Trough forearc. Mar Petrol Geol 67:604–616. https://doi.org/10.1016/j.marpetgeo.2015.05.032
Mouslopoulou V, Walsh JJ, Nicol A (2009) Fault displacement rates on a range of timescales. Earth Planet Sci Lett 278(3–4):186–197. https://doi.org/10.1016/j.epsl.2008.11.031
Mueller K (2017) Variation in slip rates on active faults: Natural growth or stress transients? Geology 45(3):287–288. https://doi.org/10.1130/focus032017.1
Muslim D, Kobayashi G, Uchiyama M, Mitamura M, Yoshikawa S (2002) The characteristics of seismic stratigraphic division of the Quaternary sediments in Kobe, southwest Japan. Earth Sci 56(6):321–332. https://doi.org/10.15080/agcjchikyukagaku.56.6_321
Nakajima T (2018) Tectonics of sedimentary basins in and around Japan since the opening of the Sea of Japan. J Geol Soc Japan 124(9):693–722. https://doi.org/10.5575/geosoc.2018.0049
Nakajima J, Hasegawa A (2007) Subduction of the Philippine Sea plate beneath southwestern Japan: Slab geometry and its relationship to arc magmatism. J Geophys Res 112:B08306. https://doi.org/10.1029/2006JB004770
Nakamukae M, Katao H, Nemoto H, Nakagawa Y (2003) Focal mechanisms of microearthquakes in Osaka Basin. Zisin J Seismol Soc Japan (zishin) 56(3):303–309. https://doi.org/10.4294/zisin1948.56.3_303(inJapanese)
Nakamura S (1999) On a relation between tsunami source and seismic fault. La mer 37:81–83
Nakata T, Yomogida K (1995) Surface fault characteristics of the 1995 Hyogo-ken-nambu earthquake. J Nat Disaster Sci 16(3):1–9
Nakata T, Odaka J, Goto H, Asahi K, Chida N, Suzuki Y, Watanabe M, Nakamura T (1996) A trench study on the surface fault rupture in Awaji Island associated with the 1995 Hyogoken-nambu earthquake. Active Fault Res 14:23–27. https://doi.org/10.11462/afr1985.1996.14_23
Nakaseko K (1987) Using of the geological methods to the submarine strata -As an example of the Kansai International Airport in Osaka Bay-. J Japan Soc Eng Geol 28(4):201–211. https://doi.org/10.5110/jjseg.28.201
Nakatani M (2020) Evaluation of phenomena preceding earthquakes and earthquake predictability. J Disast Res Special Issue Earthq Volcano Hazards Observ Res Progr 15(2):112–143. https://doi.org/10.20965/jdr.2020.p0112
Nanayama F (1999) Paleoseismological study of the Tomogashima-suido fault, Median Tectonic Line active faultsystem, during the Holocene, at the eastern side of the Kitan Straits, central Japan. Geol Surv Japan Inter Rep EQ/99/3 1999, Interim Report on Active Fault and Paleoearthquake Researches 235–252
Nanayama F, Sugiyama Y, Kitada N, Takemura K, Iwabuchi Y (2000) Holocene activity of the Osaka-wan fault and Wada-misaki fault off Kobe, Osaka Bay, central Japan. Inter Rep Active Fault Paleoearthq Res 1999:179–193
Nanayama F, Doi Y, Kitada N, Takemura K (2001) Stratigraphic, sequence stratigraphic and sedimentary environment analyses on the late Pleistocene-Holocene sediments of the eastern side of Osaka Bay, central Japan since 130 ka. J Geol Soc Jpn 107(2):179–197. https://doi.org/10.5575/geosoc.107.179
National Institute of Advanced Industrial Science and Technology (2012) Active Fault Database of Japan. February 28, 2012 version. Research Information Database DB095, National Institute of Advanced Industrial Science and Technology. https://gbank.gsj.jp/activefault/index_e_gmap.html
Nishimura T, Yokota Y, Tadokoro K, Ochi T (2018) Strain partitioning and interpolate coupling along the northern margin of the Philippine Sea plate,

estimated from Global Navigation satellite system and global positioning system-acoustic data. Geosphere 14(2):535–551. https://doi.org/10.1130/GES01529.1
Nishimura T, Hashimoto M, Fujiwara S (2020) Crustal deformation before and after the 2018 M6.1 Northern Osaka Earthquake. Disaster Prevention Research Institute Annuals 63(B): 61–68.
Nishiwaki H, Okudaira T, Ishii K, Mitamura M (2021) Dip angles of active faults from the surface to the seismogenic zone inferred from a 2D numerical analysis of visco-elasto-plastic models: a case study for the Osaka Plain. Earth Planets Space 73:86. https://doi.org/10.1186/s40623-021-01390-8
Ohzono M, Sagiya T, Hirahara K, Hashimoto M, Takeuchi A, Hoso Y, Wada Y, Onoue K, Ohya F, Doke R (2011) Strain accumulation process around the Atotsugawa fault system in the Niigata–Kobe Tectonic Zone, central Japan. Geophys J Int 184:977–990. https://doi.org/10.1111/j.1365-246X.2010.04876.x
Okada A (1970) Fault topography and rate of faulting along the Median Tectonic Line in the drainage basin of the river Yoshino, northeastern Shikoku. Japan Geogr Rev Jpn 43(1):1–21. https://doi.org/10.4157/grj.43.1
Okada A, Sangawa A (1978) Fault morphology and Quaternary faulting along the Median Tectonic Line in the southern part of the Izumi Range. Geogr Rev Jpn 51(5):385–405. https://doi.org/10.4157/grj.51.385
Okada A, Tsutsumi H (1997) Holocene activity of the chichio fault, the median tectonic line active fault system, southwest japan, based on trenching studies. J Geogr 106(5):644–659. https://doi.org/10.5026/jgeography.106.5_644
McClay JK (1996) Geometry and kinematics of single-layer detachment folds 1. AAPG Bull 80(7):1085–1109. https://doi.org/10.1306/64ED8CA0-1724-11D7-8645000102C1865D
Research and Development Bureau/Ministry of Education, Culture, Sports, Science and Technology, Japan (MEXT), Disaster Prevention Research Institute/Kyoto University (DPRI) (2013) Comprehensive Study on the Uemachi Fault Zone. 2010–2012 Project report. https://www.jishin.go.jp/database/project_report/uemachi_juten/uemachi_juten-h24/ (**Japanese**)
Sagiya T, Miyazaki S, Tada T (2000) Continuous GPS array and present-day crustal deformation of Japan. Pure Appl Geophys 157:2303–2322. https://doi.org/10.1007/PL00022507
Sagiya T (2004) A decade of GEONET: 1994–2003 -The continuous GPS observation in Japan and its impact on earthquake studies-. Earth Planets Space. https://doi.org/10.1186/BF03353077
Saito M, Tsukuda E, Okada A, Furusawa A (1997) AT tephra found in the fluvial lower terrace deposits at the northern wakayama city, and the slip rate of the negoro fault, median tectonic line active fault system. Central Jpn Quat Res 36(4):277–280. https://doi.org/10.4116/jaqua.36.277
Saito Y, Ikehara K, Tamura T (2016) Coastal geology and oceanography. In: The Geology of Japan, Geological Society, London, Geology Series. Ed: Moreno T, Wallis S, Kojima T, Gibbons W. https://doi.org/10.1144/GOJ.15
Sangawa A (1978) Fault topography and Quaternary faulting along the middle and eastern parts of the Arima-Takatsuki Tectonic Line, Kinki district, central Japan. Geogr Rev Jpn 51(10):760–775. https://doi.org/10.4157/grj.51.760
Sangawa A (2001) Recent results of paleoseismological study based on earthquake traces excavated at archaeological sites (in Japanese with English abstract). Ann Rep Active Fault Paleoearthq Res Geol Surv Jpn/AIST 1:1–26
Sato H, Hirata H, Ito T, Tsumura N, Ikawa T (1998) Seismic reflection profiling across the seismogenic fault of the 1995 Kobe earthquake, southwestern Japan. Tectonophysics 286:19–30. https://doi.org/10.1016/S0040-1951(97)00252-7
Sato H, Ito K, Abe S, Kato N, Iwasaki T, Hirata N, Ikawa T, Kawanaka T (2009) Deep seismic reflection profiling across active reverse faults in the Kinki Triangle, central Japan. Tectonophysics 472:86–94. https://doi.org/10.1016/j.tecto.2008.06.014
Sato H, Ban F, Katoh S, Hyodo M (2017) Sea-level variations during Marine Isotope Stage 7 and coastal tectonics in the eastern Seto Inland Sea area, western Japan. Quat Int 456:102–116. https://doi.org/10.1016/j.quaint.2017.03.042
Scholz C (2019) The Mechanics of Earthquakes and Faulting. In The Mechanics of Earthquakes and Faulting (p. I). Cambridge: Cambridge University Press. https://doi.org/10.1017/9781316681473
Seeber L, Sorlien CC (2000) Listric thrusts in the western Transverse Ranges. California GSA Bulletin 112(7):1067–1079. https://doi.org/10.1130/0016-7606(2000)112%3c1067:LTITWT%3e2.0.CO;2
Seno T, Stein S, Gripp AE (1993) A model for the motion of the Philippine Sea Plate consistent with NUVEL-1 and geological data. J Geophys Res 98(B10):17941–17948. https://doi.org/10.1029/93JB00782
Sibuet JC, Letouzey J, Barbier F, Charvet J, Foucher JP, Hilde TWC, Kimura M, Chiao L-Y, Marsset B, Muller C, Stéphan J-F (1987) Back arc extension in the Okinawa Trough. J Geophys Res: Solid Earth 92(B13):14041–14063. https://doi.org/10.1029/JB092iB13p14041
Steer P, Simoes M, Cattin R, Shyu B (2014) Erosion influences the seismicity of active thrust faults. Nat Commun 5:1–7. https://doi.org/10.1038/ncomms6564
Suzuki Y, Arimoto J, Otsuka H, Hamahashi M (2021) Preliminary results of the multichannel seismic reflection survey in Osaka Bay, Japan. Geol Surv Jpn Interim Rep 82:1–6
Tanaka A (2004) Geothermal gradient and heat flow data in and around Japan (II): Crustal thermal structure and its relationship to seismogenic layer. Earth Planets Space 56(12):1195–1199. https://doi.org/10.1186/BF03353340
Tatsumi Y (2006) High-Mg andesites in the Setouchi volcanic belt, southwestern Japan: analogy to archean magmatism and continental crust formation? Ann Rev Earth Planet Sci 34:467–499. https://doi.org/10.1146/annurev.earth.34.031405.125014
Terrinha P, Duarte H, Brito P, Noiva J, Ribeiro C, Omira R, Baptista MA, Miranda M, Magalhães V, RoqueTagusdelta cruise team C (2019) The Tagus River delta landslide, off Lisbon, Portugal. Implic Marine Geo-Hazards Mar Geol 416:105983. https://doi.org/10.1016/j.margeo.2019.105983
The Headquarters for Earthquake Research Promotion (2001) Methods for Evaluating Long-term Probability of Earthquake Occurrence. https://www.jishin.go.jp/reports/research_report/choukihyoka_01b/ (**In Japanese**)
The Headquarters for Earthquake Research Promotion/ Earthquake Research Committee (2001) Long-term evaluation for the Ikoma Fault. Long-term evaluations of active faults No. 511. https://www.jishin.go.jp/main/chousa/katsudansou_pdf/77_ikoma.pdf (**In Japanese**)
The Headquarters for Earthquake Research Promotion/ Earthquake Research Committee (2014) Long-term evaluation for the Osaka Bay Fault. Long-term evaluations of active faults No. 515. https://www.jishin.go.jp/main/chousa/katsudansou_pdf/98_osaka-wan.pdf (**In Japanese**)
Tsukuda E (1992) Active tectonics of southwest Japan arc controlled by the westward translation of the forearc sliver. Mem Geol Soc Jpn 40:235–250
Uchida N, Bürgmann R (2021) A decade of lessons learned from the 2011 Tohoku-Oki Earthquake. Rev Geophys. https://doi.org/10.1029/2020RG000713
Usami M (2002) Distribution of the Osaka-wan fault estimated from the existing multi-channel seismic profiles. Active Fault Res 22:111–114. https://doi.org/10.11462/afr1985.2002.22_111
Van Wagoner JC, Posamentier HW, Mitchum RM, Vail PR, Sarg JF, Loutit TS, Hardenbol J (1988) An overview of sequence stratigraphy and key definitions. In: Wilgus CK, Hastings BS, Kendall CG.St.C, Posamentier HW, Ross CA, Van Wagoner JC (Eds.), Sea Level Changes – An Integrated Approach. Special Publication vol. 42. Society of Economic Paleontologists and Mineralogists (SEPM) 39–45
Wolff EW, Chappellaz J, Blunier T, Rasmussen SO, Svensson A (2010) Millennial-scale variability during the last glacial: the ice core record. Quat Sci Rev 29(21–22):2828–2838. https://doi.org/10.1016/j.quascirev.2009.10.013
Wu J, Suppe J, Lu R, Kanda R (2016) Philippine Sea and East Asian plate tectonics since 52 Ma constrained by new subducted slab reconstruction methods. J Geophys Res 121(6):4670–4741. https://doi.org/10.1002/2016JB012923
Yashima K (1992) Study and analysis on caldrons in the Seto Inland Sea, using the basic map of the sea "Coastal Series." Rep Hydrogr Res 28:139–230
Yasuhara M, Irizuki T, Yoshikawa S, Nanayama F, Mitamura M (2004) Holocene ostracode paleobiogeography in Osaka Bay, southwestern Japan. Mar Micropaleontol 53(1–2):11–36. https://doi.org/10.1016/j.marmicro.2004.02.002
Yasuhara M (2008) Holocene ostracod palaeobiogeography of the Seto Inland Sea, Japan: impact of opening of the strait. J Micropalaeontol 27:111–116. https://doi.org/10.1144/jm.27.2.111

Yokokura T, Kano N, Yamaguchi K, Miyazaki T, Ikawa T, Ohta Y, Kawanaka T, Abe S (1998) Seismic profiling of deep geological structure in the Osaka Bay area. Bull Geol Surv Jpn 49(11):571–590
Yokota H, Ikawa T, Sano M, Takemura K (1997) Seismic reflection profiles across the northern part of Osaka Bay and Rokko mountain foothill. In: Museum of Nature and Human Activities, Hyogo (ed) The great Hanshin-Awaji earthquake disaster and Rokko movements—Report on the research of active tectonics around the damaged area by the 1995 Hyogoken-Nanbu earthquake. Kobe Civil Engineering Office, Kobe pp 57–89 (**In Japanese**)
Yokota Y, Ishikawa T, Watanabe S, Tashiro T, Asada A (2016) Seafloor geodetic constraints on interpolate coupling of the Nankai Trough megathrust zone. Nature 534:374–377. https://doi.org/10.1038/nature17632
Yoshikawa S, Nakagawa K, Kawabe T, Furutani M, Daishi M (1987) Reconsideration of the OD-2 and OD-1 core samples in Osaka City, central Japan. J Geol Soc Jpn 93(9):653–665. https://doi.org/10.5575/geosoc.93.653
Yu J, Henrys SA, Brown C, Marsh I, Duffy G (2015) A combined boundary integral and Lambert's Law method for modelling multibeam backscatter data from the seafloor. Cont Shelf Res 104:60–69. https://doi.org/10.1016/j.csr.2015.04.020
Zang SX, Chen QY, Ning JY, Shen ZK, Liu YG (2002) Motion of the Philippine Sea plate consistent with the NUVEL-1 model. Geophys J Int 150(3):809–819. https://doi.org/10.1046/j.1365-246X.2002.01744.x
Zhang W, Askarinejad A (2019) Centrifuge modelling of submarine landslides due to static liquefaction. Landslides 16:1921–1938. https://doi.org/10.1007/s10346-019-01200-z

Publisher's Note